UNIVERSITÀ DEGLI STUDI DI PALERMO

Dottorato di Ricerca in Fisica
Dipartimento di Fisica e Chimica
Settore Scientifico Disciplinare FIS/07

THE PHYSICAL ORIGIN OF PROTEIN DYNAMICAL TRANSITION: A LIQUID-LIQUID TRANSITION IN HYDRATION WATER?

IL DOTTORE
Margarita Fominà

IL COORDINATORE
Prof. Antonio Cupane

IL TUTOR
Prof. Antonio Cupane

CICLO XXIV
ANNO CONSEGUIMENTO TITOLO 2015

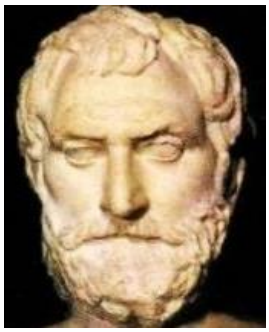

“L'acqua è la sostanza da cui traggono origine tutte le cose; la sua scorrevolezza spiega anche i mutamenti delle cose stesse. Questa concezione deriva dalla constatazione che animali e piante si nutrono di umidità, che gli alimenti sono ricchi di succhi e che gli esseri viventi si disseccano dopo la morte.”

(Talete di Mileto)

Abstract

In this thesis I study, by means of neutron scattering, calorimetry, and dielectric spectroscopy, the physical origin of protein dynamical transition (PDT) which is usually observed at ~230 K in protein hydrated powders and is deemed necessary for protein function. Measurements reported in this thesis have been performed on hydrated powders of Myoglobin. The combined use of different experimental techniques gives a coherent description of the PDT and reveals a connection with a liquid-liquid crossover occurring in the protein hydration water at about the same temperature. In order to deepen our understanding of this connection and to obtain a direct experimental evidence of the existence of a liquid-liquid transition (LLT) in supercooled water at low temperatures, we investigated a second system, i.e. deeply cooled water confined within the pores of a 3-dimensional disordered SiO_2 xerogel. In this system the hydrophilic surface of the matrix pores mimics the protein surface, while water confined within the pores mimics the protein hydration water. Using the same experimental techniques, we obtained evidence for the presence of a LLT, occurring at about 230 K, between a low density liquid (LDL) predominant at lower temperatures and a high density liquid predominant at higher temperatures. In conclusion, we suggest that the LLT in protein hydration shell is the physical origin of the biologically relevant protein dynamical transition.

Contents

Introduction

Proteins are characterized by a large structural heterogeneity. They assume an overall 3-dimensional arrangement corresponding to the biologically active conformation; however, owing to the high flexibility and to the non-covalent interactions stabilizing their structure, they can explore, by thermal motions, a large number of conformational substates [**1**]. As a consequence, protein dynamics ranges over a large time-space domain, from local harmonic vibrations (femtoseconds), to collective vibrations (picoseconds), to molecular groups rotations (picoseconds) and local molecular rearrangements (pico/nanoseconds), up to relative movements of larger groups of the protein (micro-milliseconds).

The exploration by proteins of conformational substates is dynamically reflected in the activation of anharmonic atomic fluctuations; this anharmonic activation is deemed essential for protein functioning. The main onset of this kind of motions in hydrated proteins is the well-known "protein dynamical transition" (PDT), a steep increase in the amplitude of atomic motions revealed at about 220-240 K by different techniques like, e.g., elastic neutron scattering (ENS) [**2**]. The physical origin of this transition is still unclear, and different models have been proposed to explain it [**3–11**]. There is however a general consensus about the essential role played by solvent (although not necessarily water [**12**]) in this phenomenon. In fact, for dry protein powders, no PDT is observed. It is therefore well accepted that protein dynamics is intimately coupled to the properties of the surrounding medium which, in the biological environment, is mainly water.

Studies on the hydration dependence of protein dynamics are therefore important, both from the point of view of Biophysics/Soft Matter (hydrated proteins may help understanding the behavior of complex systems like e.g. glasses) and from a more biological point of view since hydration/dehydration may be relevant in the regulation of protein function and in cryopreservation. This notwithstanding, systematic studies on the hydration dependence of protein dynamics are lacking. Among the few works present in the literature, it is relevant to mention those by Khodadadi et al., 2008 [**13**] (on hydrated lysozyme powders) and by Jansson et al., 2011 [**14**] (on myoglobin hydrated powders, in which however water/glycerol mixtures were used as "solvent").

In the first part of my thesis I will present a systematic study of the hydration dependence of D_2O-hydrated myoglobin (Mb) powders, in the hydration range $0 \div 0.5$ gr D_2O/gr protein. In view of the wide time scale involved in protein dynamics, the measurements by ENS (time scale hundreds of picoseconds) and broadband dielectric spectroscopy (BDS, time scales ranging from hundreds of nanoseconds to seconds or more) were performed. Besides the different timescales, it

should also be kept in mind that the two techniques probe different types of motions. In fact, ENS on D_2O-hydrated protein powders monitors essentially motions of the nonexchangeable hydrogen atoms, evenly distributed over the entire protein, that include e.g. methyl groups rotations and librational/translational-like motions of the amino acid side chains. On the other hand BDS, although covering a broad frequency range, measures motions of all the dipoles in the sample, so that assignment of the observed relaxations to specific groups (e.g. amino acid side chains and/or hydration water) is often very difficult. In this work also Differential Scanning Calorimetry (DSC) is used, in order to obtain a thermodynamic description of the systems studied.

The combined use of the above mentioned experimental techniques sensitive to hydration water and protein has led to the idea that the PDT can be connected with a transition in the hydration water since the activation of anharmonic atomic motions detected by ENS lies in the same temperature range (220-240 K) of the endothermic peak onset revealed by thermodynamic investigation (DSC) and a fragile-to-strong crossover of one of the dielectric processes obtained by BDS. Indeed, one of the models proposes a connection of PDT with the transition between two distinct forms of supercooled liquid water (like protein hydration water), a low density liquid (LDL), and a high density liquid (HDL). In this scenario, originally proposed by Chen and coworkers [**7, 15-17**], interfacial water on protein surface undergoes a transition at 220-230 K (Liquid-Liquid Transition, LLT), connected with a change in its dynamical properties revealed as a crossover from an Arrhenius to a super-Arrhenius temperature dependence of the relaxation times. The LLT hypothesis for supercooled water has been supported also by computational studies [**18–20**], but recently questioned by Limmer and Chandler [**21, 22**]. A model based on the cooperativity of a 2-dimensional hydrogen network has been also proposed, where two dynamic crossovers are expected to occur at 180 and 250 K (at ambient pressure), the latter consistent with the presence of a low-temperature water critical point [**23**]. However, other experimental works investigating the temperature dependence of water relaxation times have seriously questioned the existence of the LLT in the protein hydration water [**24–26**].

If the LLT actually occurs, the coupling between hydration water and protein molecular groups would cause, in turn, the activation of anharmonic protein motions, revealed by neutron scattering as an enhancement of protein mean square fluctuations and identified as the PDT. Further support to this picture of the PDT has been given by a recent neutron scattering work on homomeric polypeptides [**8, 9**], where the dependence of PDT onset temperature and fluctuations amplitude on energy resolution has been used to investigate the energetic details of this phenomenon.

The second part of the thesis will be devoted to the search of direct experimental evidence for the existence of a LLT in deeply cooled confined water. Unfortunately, the hydration water of protein powders is not easily accessible by Incoherent Neutron Scattering or by Broadband dielectric spectroscopy since, as already discussed, the signal coming from hydration water cannot be straightforwardly separated from that coming from the protein hydrogens/dipoles. To circumvent this difficulty, we used a model system in which water is confined within a nanoporous silica xerogel, thus allowing to enter deeply into the supercooled region. Indeed, it has been shown [**27–29**] that water confined in such matrices remains liquid at temperatures much lower than the homogeneous nucleation temperature (about 235 K at atmospheric pressure), in contrast to bulk water, and thus can be used to explore the properties of liquid water in the so-called "no man's land." Moreover, the hydration level of this kind of matrices can be easily tuned, thus allowing estimating the contribution from matrix and the effect of water interaction with matrix inner surfaces. By the sol-gel method the prepared solid silica matrix has 3D-disordered structure with a broad pore size distribution (Figure 1). This system, unlike ordered MCM-41-S, mimics the protein surface and water inside of its pores is similar to the hydration water. Also the proposed model system is cheap and easy to prepare; moreover, the silica matrix scarcely contributes to incoherent neutron scattering and to dielectric relaxations. In this second part, besides Elastic Incoherent Neutron Scattering, BDS, and calorimetry, we have used also inelastic neutron scattering to investigate the temperature dependence of the collective vibrational dynamics (the so-called boson peak) of confined water. Finally, a new approach to study the water anomalies, and in particular the pressure anomaly (i.e. the anomalous increase of the translational diffusion coefficient with increasing pressure) via Elastic neutron Scattering gives further experimental support to the real existence of a LLT in deeply cooled confined water.

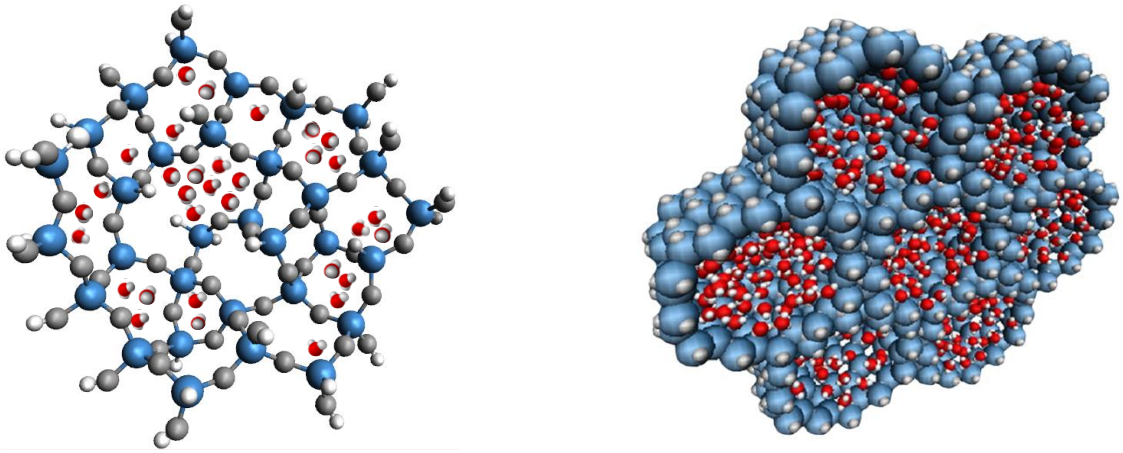

Figure 1. *Left panel*: a sketch of hydrated disordered SiO_2 matrix with broad pore size distribution. *Right panel*: 3D schematic representation of a D_2O hydrated MCM-41-S nanoporous silica crystallite (pore diameter 15 Å ± 2 Å) is taken from [**30**].

In conclusion, aim of this thesis is to contribute to the clarification of an highly debated scientific issue like the physical origin of the PDT and, by means of studies on deeply cooled confined water, to provide experimental evidence for the real existence of a LLT which we suggest to be the underlying physical phenomenon that induces the activation of biologically relevant anharmonic atomic motions in proteins.

Chapter 1

Experimental techniques

1.1. Broadband dielectric spectroscopy

Broadband dielectric spectroscopy (BDS) is a powerful method for investigations of molecular dynamics of various materials. It enables to monitor molecular mobility reflected in the relaxation processes over a wide frequency range up to 9 decades, at different temperatures. BDS finds application in many fields of science and technology. It is successfully employed in studies on (i) the molecular dynamics of liquids, biological systems, disordered crystals, (ii) charge transport in ionic liquids, semiconductors, (iii) structural material properties like phase compositions, (iv) non-linear electrical and optical effects. BDS is also a very useful tool to monitor chemical reactions and phase transitions, e.g. vitrification or crystallization.

1.1.1. Theoretical background (Electric polarization and dielectric relaxation)

A perfect dielectric is a material with zero electrical conductivity whose internal structure comprises only bound electric charges. When dielectric is placed in an electric field, practically no current flows through it because there are no free charges that may drift through a material. Instead, dielectric can be polarized by an electric field.

When an electric field is applied across the faces of a parallel plate capacitor containing a dielectric, the atomic and molecular charges in the dielectric are displaced from their equilibrium positions and the material is said to be polarized. There are two major polarization mechanisms in polymeric materials that are studied by dielectric spectroscopy: 1) polarization due to charge displacement (induced dipoles), and 2) polarization due to orientation of permanent dipoles. Migration of charges gives rise to conductivity.

Displacement (electronic or ionic) polarization is polarization caused by relative displacements between positive and negative charges in the field presence. In the classical approach to the dielectric model, a material is made up of atoms. Each atom consists of a cloud of negative charge (electrons) bound to and surrounding a positive point charge at its center. In the presence of an electric field the charge cloud is distorted and directed in the opposite direction of the field. In this case the local dipole moment p between opposite charges is induced and points in the same

direction as the electric field. This creates an internal electric field that reduces the overall (total) field within the dielectric using the superposition principle; of course, when the electric field is removed the atom returns to its original state.

In general a polarization $\vec{P}$ can be related to dipole moments $\vec{p}_i$ of the particles or molecules within a volume V by

$$\vec{P} = \frac{1}{V}\sum_{i=1}^{N} \vec{p}_i \tag{1}$$

with

$$\vec{p}_i = q_i \vec{d}_i \tag{2}$$

where charges q_i are separated by a distance $\vec{d}_i$ and N denotes the whole number of charges/dipoles in the system. The polarization can be interpreted as a measure of how strong and how aligned the dipoles are in a region of the material.

Polar molecules have a permanent dipole moment μ which is randomly oriented but can be oriented to the applied field. In this case the orientational (dipolar) polarization takes place. For example, a water molecule retains polarization in the absence of a field; its permanent dipole moment exists at 104.45° angle between the asymmetric bonds of oxygen and hydrogen atoms. When an external electric field is applied, the distance between charges within each permanent dipole, which is related to chemical bonding, remains constant in orientational polarization; however, the direction of polarization itself rotates. The assembly of all dipoles in a material forms a macroscopic polarization:

$$\vec{P} = \frac{1}{V}\sum_{i=1}^{N} \mu_i + \vec{P}_\infty = \frac{N}{V}\langle \mu \rangle + \vec{P}_\infty \tag{3}$$

where $\langle \mu \rangle$ is the mean permanent dipole moment.

For linear dielectrics the susceptibility χ is defined as the constant of proportionality relating the electric field $\vec{E}$ to the polarization $\vec{P}$ such that:

$$\vec{P} = \chi \varepsilon_0 \vec{E} \tag{4}$$

where ε_0 is the electric permittivity of free space, constant value. The susceptibility χ of a linear dielectric material is a measure of how easily it polarizes in response to the electric field.

Let's consider two originally uncharged parallel metal plates (capacitor) with nothing in between. If electric charge is transferred between these conducting surfaces, one becomes positively charged and the other negatively charged by the same amount, and an electric field exists between the plates. An electric displacement field $\vec{D}_0$ which is associated with the presence of separated free electric charges will be:

$$\vec{D}_0 = \varepsilon_0 \vec{E} \tag{5}$$

If a dielectric medium is inserted between these charged plates (inside capacitor), the dielectric polarization reduces the value of the electric field that was present before the insertion of dielectric. The actual value of the electric displacement field $\vec{D}$ therefore has also a component $\vec{P}$ that depends on the bound polarization charges. The relationship among the three vectors $\vec{D}$, $\vec{P}$ and $\vec{E}$ in SI system is:

$$\vec{D} = \vec{D}_0 + \vec{P} = \varepsilon_0 \vec{E} + \chi \varepsilon_0 \vec{E} = (1 + \chi)\varepsilon_0 \vec{E} = \varepsilon_r \varepsilon_0 \vec{E} = \varepsilon \vec{E} \tag{6}$$

where

$$1 + \chi = \varepsilon_r = \frac{\varepsilon}{\varepsilon_0} \tag{7}$$

is a relative permittivity of the material, i.e. the factor by which the electric field between the charges is decreased or increased relative to free space. As clear seen the susceptibility χ determines the permittivity of material ε which relates to the material's ability to transmit (or "permit") an electric field.

If a dielectric in equilibrium state is disturbed by the time-dependent external electrical field $E(t)$, the response of the system will be the polarization $P(t)$. Electronic polarization takes place on a time scale of 10^{-12} s because of the low mass of the electron, therefore it is not relevant in our time scales. Concerning the permanent dipoles, the distance between charges within each permanent dipole, which is related to chemical bonding, remains substantially constant; however, the average orientation of dipoles changes. The rotational fluctuations of molecular dipoles occur on a timescale that depends on the surrounding local viscosity of the molecules. As a consequence, the dipole rotation is not instantaneous and the response of the orientational polarization to a change of the electric field is always retarded. This process is called dielectric relaxation. Each relaxation process is characterized by a relaxation time τ, i.e. the characteristic time needed to reach a new equilibrium. The simplest theoretical description of relaxation as function of time t is an exponential law $exp(-t/\tau)$. In addition to the relaxation phenomenon of molecular dipoles there

may be a drift motion of mobile charge carriers (electrons, ions or charged defects) which causes conductive contribution to the dielectric response.

Note that, in general, there are two additional aspects of induced polarization that one should recognize and account for in the interpretation of experimental results. The first is electrode polarization, which results from the accumulation of ions at the sample-electrode interface. The second aspect is the polarization due to the buildup of charges at the interface between components in heterogeneous systems (suspensions or colloids, biological materials, phase separated polymers). This polarization is known as interfacial, space charge, or Maxwell-Wagner polarization. Both cases are related with a separation of charges. The charges are often separated over a considerable distance (relative to the atomic and molecular sizes), and the contribution to dielectric response can therefore be orders of magnitude larger than that caused by molecular fluctuations.

A simple approach to calculate the time dependence of dielectric behavior was proposed a long time ago by Peter Debye. The Debye model assumes that a dipolar relaxation is characterized by a single characteristic time τ and that the time derivative of the polarization is proportional to the difference between the actual value and the equilibrium static (ω → 0) value:

$$\frac{dP}{dt} = -\frac{1}{\tau}\left[P(t) - P_{\mathrm{eq}}\right] \tag{8}$$

where

$$P_{\mathrm{eq}} = \chi_{\mathrm{s}} E = \chi_{\mathrm{s}} E_0 e^{i\omega t} \tag{9}$$

and χ_{s} is the static (ω → 0) susceptibility. By integrating one easily obtains:

$$P(t) = \frac{\chi_{\mathrm{s}} E_0 e^{i\omega t}}{1 + i\omega\tau} = \chi(\omega) E \tag{10}$$

where

$$\chi(\omega) = \frac{\chi_{\mathrm{s}}}{1 + i\omega\tau} = \frac{\chi(1 - i\omega\tau)}{1 + \omega^2\tau^2} \tag{11}$$

The frequency dependent susceptibility is now a complex quantity:

$$\chi(\omega) = \chi'(\omega) - i\chi''(\omega) \tag{12}$$

where

$$\chi' = \frac{\chi_s}{1 + \omega^2\tau^2} \tag{13}$$

and

$$\chi'' = \frac{\chi_s\omega\tau}{1 + \omega^2\tau^2} \tag{14}$$

This simple analysis refers to a single relaxation; in this case χ' goes from χ_s (in the limit $\omega \to 0$) to 0 (in the limit $\omega \to \infty$). In a more general case possible susceptibility contributions still present at the highest frequency investigated are taken into account by a term χ_∞ and the presence of several relaxations is considered. In this case

$$\chi'(\omega) = \chi_\infty + \sum_{i=1}^{N} \frac{\Delta\chi_i}{1 + \omega^2\tau_i^2} \tag{15}$$

and

$$\chi''(\omega) = \sum_{i=1}^{N} \frac{\Delta\chi_i\omega\tau_i}{1 + \omega^2\tau_i^2} \tag{16}$$

where $\Delta\chi_i$ and τ_i are the amplitude and characteristic time of the i^{th} relaxation. Theoretical plots of ε' and ε'' vs ω on a logarithmic scale are reported in Figure 2 (left panel) for a single relaxation.

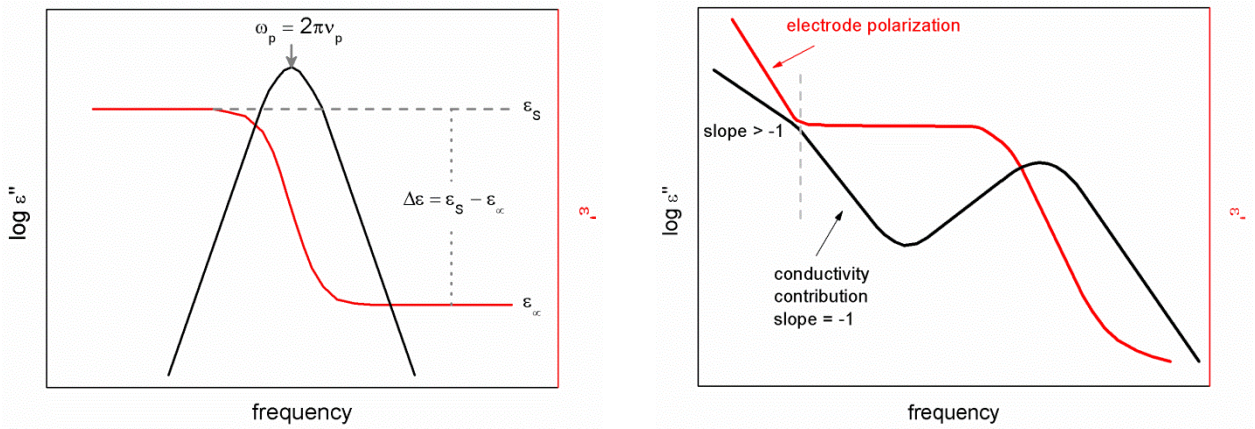

Figure 2. Theoretical real ε' (red line) and imaginary ε'' (black line) part of the complex dielectric function for a relaxation process (*left panel*) and with conductivity and electrode polarization contributions (*right panel*).

In case of the presence in a material of mobile charge carries, the BDS data will show electrical conductivity phenomena as a linear increase of the imaginary part of the dielectric function with decreasing frequency:

$$\varepsilon''(\omega) = \frac{\sigma_0}{\varepsilon_0 \omega} \tag{17}$$

where σ_0 is the (electronic) d.c.-conductivity. For pure electronic conduction no contribution arises to ε'. At difference, for polarization effects (at inner boundaries or external electrodes) the real part of $\varepsilon^*(\omega)$ increases with decreasing frequency. The amplitude of these effects can vary extremely for different materials and in some cases can completely suppress other features in the spectra. A schematic example of the influence of conduction and electrode polarization to the complex dielectric function at low frequency is shown in Figure 2 (right panel).

1.1.2. BDS data analysis

In most cases the width of measured loss peaks is much broader than predicted by Debye equation and in addition their shapes are asymmetric with a high frequency tail. This is called non-Debye (or non-ideal) relaxation behavior. From the physical point of view, this arises from the fact that in the Debye model all dipoles are considered equivalent for a given process and local heterogeneity is neglected: this brings about exponential relaxations in the time domain and the Debye formulas (Eqs. 13 and 14) in the frequency domain. A more realistic approach should consider, for a given process, a distribution of relaxation times thus bringing about non-exponential relaxations (e.g. stretched exponentials, see the Kohlrausch-Williams-Watts (KWW) expressions, or power laws) and more complicated frequency dependence. In the literature several empirical model functions – mostly generalizations of the Debye function – have been developed and tested which are able to describe broadened and/or asymmetric loss peaks. A more general model function was introduced by Havriliak and Negami (HN-function) [**31**]:

$$\varepsilon^*_{\mathrm{HN}}(\omega) = \varepsilon_\infty + \frac{\Delta\varepsilon}{(1 + (i\omega\tau_{\mathrm{HN}})^\beta)^\gamma} \tag{18}$$

For the fractional shape parameters β and γ which describe the symmetric and asymmetric broadening of the complex dielectric function $0 < \beta, \gamma \leq 1$ holds. Thus this equation represents a model function with a set of four parameters in the f-domain which is able to give a complete description of the relaxation process. Figure 3 gives a comparison between the Debye function and the HN-function for selected shape parameters.

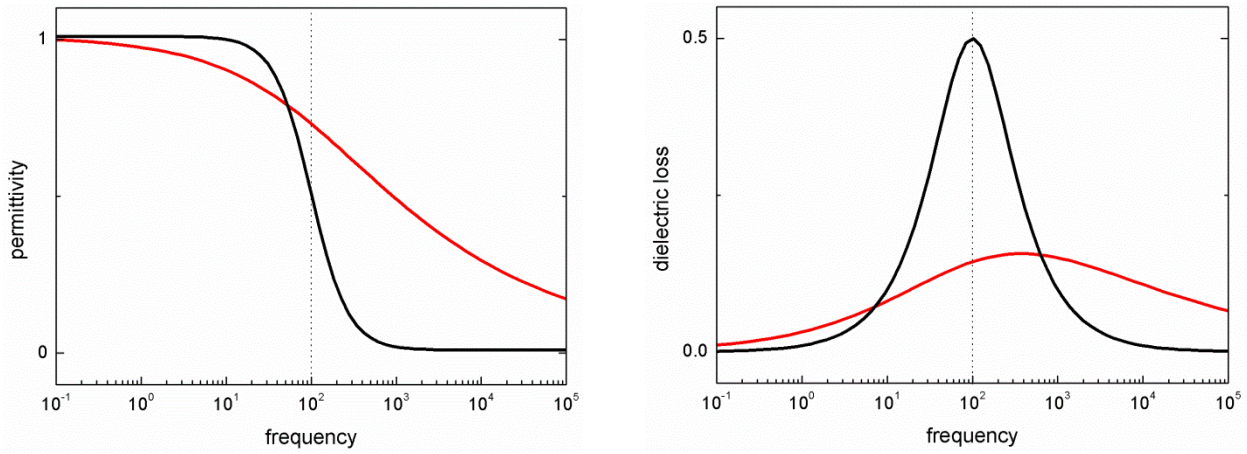

Figure 3. Real (*left panel*) and imaginary (*right panel*) parts of the complex dielectric function vs field frequency for the Debye (black curve) and the Havriliak-Negami (red curve, $\beta = \gamma = 0.5$) relaxation processes.

For glass-forming materials the molecular dynamics spans a wide time scale and in order to analyse its temperature dependence in detail it is useful to use so-called Arrhenius plot, i.e. logarithm of relaxation time with respect to 1/T (Figure 4, right panel).

Two different behaviors are usually observed:

a) the temperature dependence of the relaxation time follows the simple Arrhenius law:

$$\tau(T) = \tau_0 \cdot exp\left(\frac{-E_A}{k_B T}\right) \tag{19}$$

where E_A is the temperature independent activation energy, k_B is the Boltzmann constant and τ_0 is the relaxation time in the high temperature limit ($T \gg E_A/k_B$). This type of relaxation is non-cooperative and an example, in a simplified picture of glassy dynamics, is given by the low temperature "rattling" motion of a molecule fluctuating in the cage formed by its neighbors.

b) the temperature dependence of the relaxation time follows a super-Arrhenius cooperative behavior that can be approximated by the Vogel-Fulcher-Tammann (VFT)-equation:

$$\tau(T) = \tau_0 \cdot exp\left[\frac{-DT_0}{T - T_0}\right] \tag{20}$$

where T_0 is the temperature at which $\tau(T)$ diverges and is denoted as the Vogel temperature or the "ideal" glass transition temperature. This type of relaxation is clearly cooperative and a typical example in the simplified picture of glassy dynamics is given by the reorientation of the molecules forming the cage that are clearly dependent from each other. A schematic picture of the two types of relaxation processes is given in Figure 4. Glass-forming materials are called "fragile" if their $\tau(T)$

dependence obeys the VFT equation and "strong" if $\tau(T)$ follows the Arrhenius law. In some cases a transition from a high temperature fragile behavior to a low temperature strong behavior is observed. In this case the expression "fragile to strong crossover" (FSC) is often used.

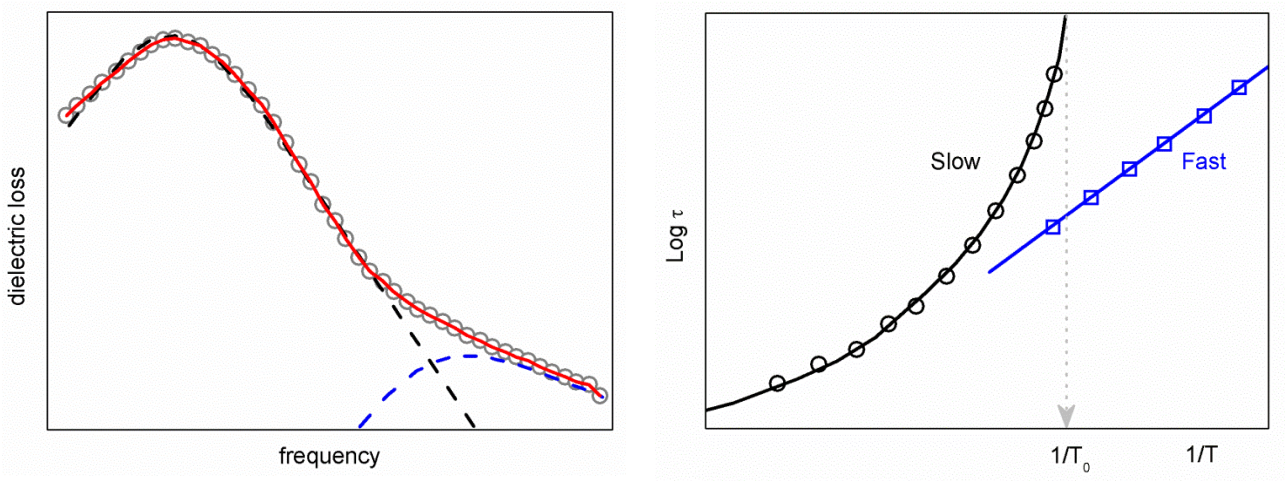

Figure 4. *Left panel*: schematic dielectric loss with fit curves to the relaxation processes. *Right panel*: schematic Arrhenius plot for corresponding processes.

1.1.3. Experimental setup

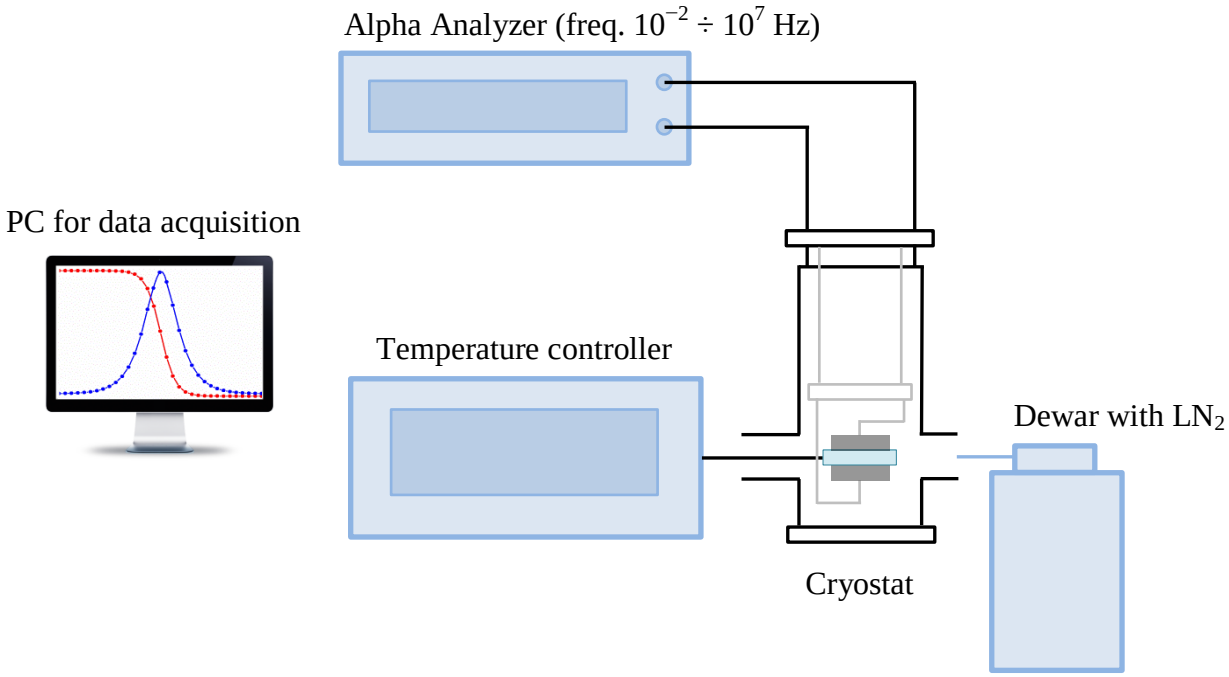

Figure 5. Simplified scheme of the experimental setup for broadband dielectric spectroscopy.

The dielectric measurements were performed with the Broadband Dielectric Spectrometer produced by Novocontrol technologies Company (Germany). The basic parts of the spectrometer are frequency analyzer, temperature controller, sample cell, cryostat, dewar with LN_2 and computer. The simplified scheme of the experimental setup is depicted in Figure 5.

The Alpha-A High Performance Frequency Analyzer measures the complex dielectric, conductivity and impedance function of materials in dependence of alternating electric field frequency with high precision. The broad frequency range of our BDS is from 10^{-2} Hz to 10^{7} Hz. The Alpha analyzer contains a frequency response analyzer (FRA) with a sine wave generator and ac voltage channel for the response signal of a system. The principle of an electric material measurement is shown below (Figure 6). A voltage U_0 with a fixed frequency $\nu = \omega/2\pi$ is applied to the sample capacitor.

$$U(t) = U_0 \cos(\omega t) = \mathrm{Re}(U^* \exp(i\omega t)) \tag{21}$$

with $U^* = U_0$

U_0 causes a current I_0 at the same frequency in the sample.

$$I(t) = I_0 \cos(\omega t + \varphi) = \mathrm{Re}(I^* \exp(i\omega t)) \tag{22}$$

In addition, there will generally be a phase shift between current and voltage described by the phase angle φ. The response signal is analyzed by Fourier transform over n periods

$$I^*(\omega) = I' + iI'' = \frac{2}{nT}\int_0^{nT} I(t)\exp(i\omega t)dt \tag{23}$$

$$I_0 = \sqrt{I'^2 + I''^2} \tag{24}$$

$$\tan(\varphi) = \frac{I''}{I'} \tag{25}$$

For a sample with linear electromagnetic response, the measured impedance of the sample capacitor

$$Z^*(\omega) = Z' + iZ'' = \frac{U_0}{I^*(\omega)} \tag{26}$$

is connected with the dielectric function of the sample material by

$$\varepsilon^*(\omega) = \varepsilon' - i\varepsilon'' = \frac{-i}{\omega Z^*(\omega)}\frac{1}{C_0} \tag{27}$$

where C_0 is the capacity of the empty sample capacitor.

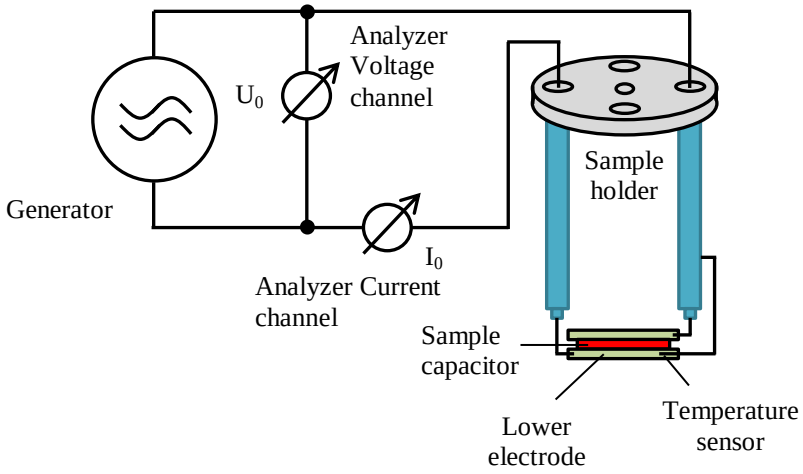

Figure 6. Block diagram showing the principle of a dielectric or impedance measurement.

The Alpha analyser display gives information on the actual state of measurement and shows the data of the last measured point. The Alpha analyser is operated by WinDETA software.

Usually a material is mounted between two parallel plate electrodes forming a sample capacitor (Figure 7). In order to adjust the electrode spacing a spacer should be used. The spacer material should have a low and frequency independent dielectric constant and low losses. Convenient spacer material is Teflon (Figure 7). To avoid the presence of conductivity contribution the electrodes were coated with Teflon layer (100 μm width). The sample capacitor should be installed between two electrodes of the Active Sample Cell which then is positioned in the cryostat before measurement.

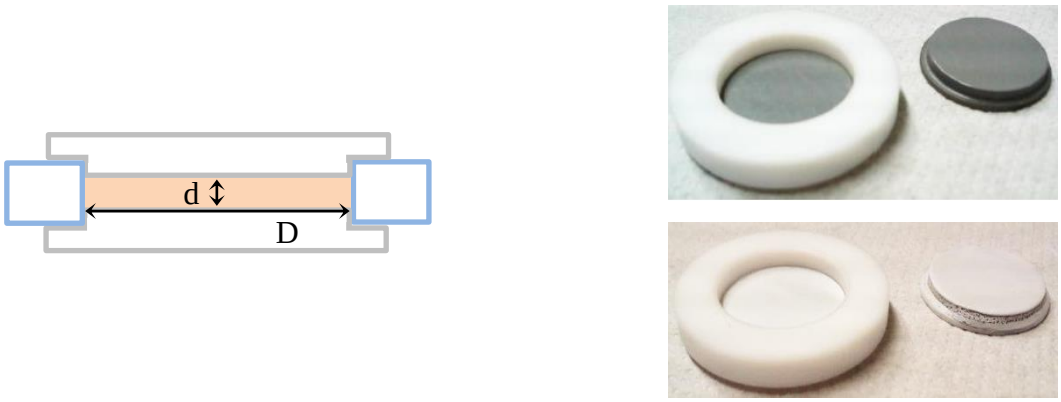

Figure 7. *Left panel*: schematic side view of sample capacitor composed of two electrods (grey), teflon o-ring (blue) and sample material (orange). Horizontal arrow indicates electrode diameter (D) and vertical one - sample thickness (d). *Right panel*: photo of experimental sample capacitor; lower part: sample capacitor electrodes are coated with Teflon layer.

BDS equipped with the Quatro cryogenic system. The sample capacitor can be temperature controlled by this temperature control system between T = −160 ÷ 500°C. With the cryosystem (having a temperature stability of typically ± 0.02 K) it is possible to trace the evolution of the dielectric spectra in steps of one degree or less.

Figure 8. Alpha-A High Resolution Broadband Dielectric Spectrometer (Novocontrol, Germany) that was used to carry out all dielectric measurements.

1.2. Differential Scanning Calorimetry

Calorimetry allows making a thermodynamic analysis of materials for different aims. Some types of thermal analysis measurement typically performed by calorimetry would be as follow: specific heat, glass transition, melting, crystallization. The field of calorimetry has a great variety of calorimetric instruments each of which has its own particular characteristics for special applications.

The object of the Differential Scanning Calorimeter (DSC) experiment is to record the heat flow rates (power) absorbed or released by a sample over a linearly changing temperature range or at a single isothermal temperature. Hence, the characteristic temperatures of a reaction / transition and the precise measurement of heat capacities are obtained in a minimum period of time. DSCs differ in the design and measuring principle, but common to all is a differential method of measurement. In such method the measured quantity is compared with a quantity of the same kind, of known value only slightly different from the value of the measured quantity, and in which the difference between the two values is measured. Therefore the twin-type design and the direct in-difference connection of the two measuring systems are also the common feature of all DSCs.

1.2.1. Theoretical background (Power compensation approach)

For our calorimetric investigations we used one of the basic types of DSCs, the power compensation DSC. It belongs to the class of heat-compensating calorimeters. In the calorimeter the sample and the reference material are placed in independent furnaces. When the temperature rises or falls in the sample material, power (energy) is applied to or removed from the calorimeter to compensate for the sample energy. As a result, the system is maintained at a "thermal null" state at all times. The amount of power required to maintain system equilibrium is directly proportional to the energy changes occurring in the sample.

The temperature difference between the two systems is measured. In a 1^{st} approximation, disturbances from the surroundings have the same effect on both measuring systems and therefore cancel out with respect to the temperature difference. The furnaces are heated separately by applying the same heating power (P_{AV}) via a control circuit (Figure 9) in order to change their mean temperature in accordance with the preset heating rate. So that they comply with the given temperature-time program (T(t) from programmer, Figure 9). When there is ideal thermal symmetry

between the two measuring systems (the temperature of both furnaces is the same, $T_S = T_R$, $\Delta T = 0$), the same heating power is required for sample and reference furnaces (P_{AV}). Any chemical reaction and many physical transitions (exothermic or endothermic process) in a material leads to releasing or consuming of additional heat. This is a case of a thermal asymmetry (temperature difference, $T_S \neq T_R$, $\Delta T \neq 0$) between two measuring systems. The temperature difference ΔT (deviation from the set value) is both the measurement signal and the input signal of a second control circuit. At the second circuit the sample's heating power is regulated (compensated) by means of a proportional controller (($T_S - T_R$) control in Figure 9) so that the electric heat supplied to the sample furnace is decreased or increased ($P \pm \Delta P$) by just the amount as has been generated or consumed during the exothermic or endothermic transition process. The compensating heating power ΔP is proportional to the remaining temperature difference ΔT: $\Delta P = -k_1 \cdot \Delta T$. The factor k_1 is a factory-set fixed quantity of the proportional controller. In the DSC the measurement signal ΔT is always obtained as electric voltage. The measurement signal output by the DSC and accessible to the user is a heat flow rate, Φ_M (in mW). The Φ_M ($_M$: measured) is internally (in the software) assigned to this signal ΔT by factory-installed provisional calibration: $\Phi_M = -k_2 \cdot \Delta T$. The factor k_2 can be changed at the instrument with the aid of a potentiometer or it is adjusted via the software (calibration). The factor k_2 is almost independent of measurement parameters (temperature), and can therefore in principle be determined by one calibration measurement at one temperature only.

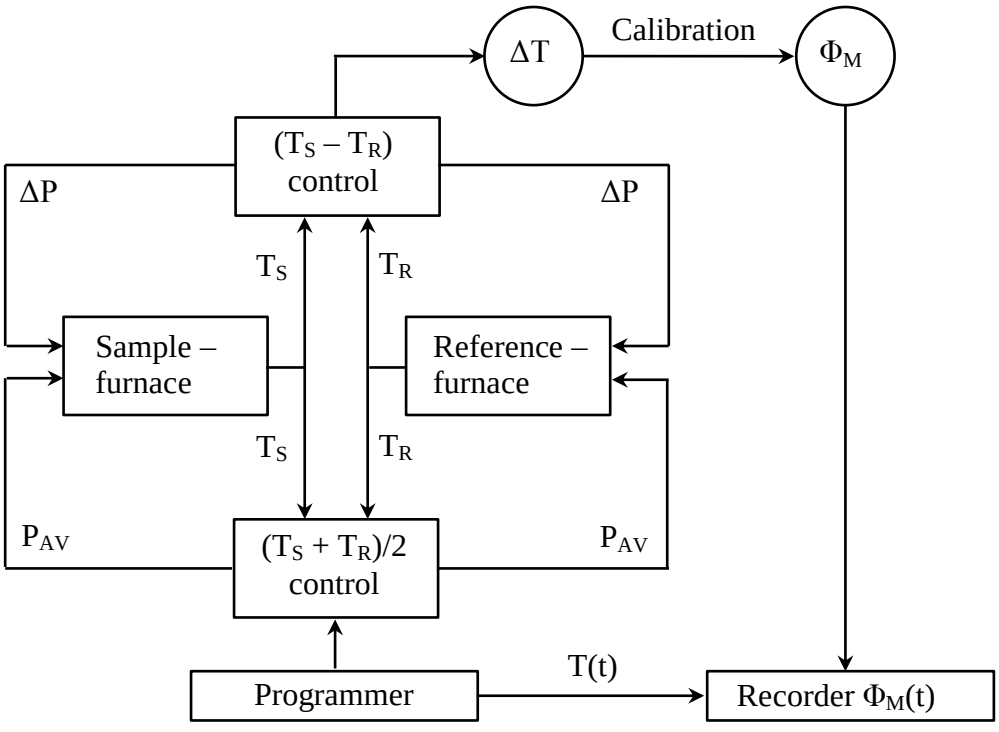

Figure 9. Block diagram showing the function principle of power compensation DSC. T_S is a temperature of sample furnace, T_R is a temperature of reference furnace, $\Delta T = T_S - T_R$, P_{AV} is an average heating power, ΔP is a compensation heating power, Φ_M is a measured heat flow rate [**32**].

The relation between Φ_M and the true heat flow rate exchanged with the sample is $\Phi_{TRUE} = K_\Phi \cdot \Phi_M$, where K_Φ is a proportionality factor which is determined by calibration. The integral of the compensated power over the time is proportional to the heat exchanged by the sample. All these parameters are handled via software, which provides the real heat flow rate at a given temperature as output.

The advantages of the twin principle of DSCs become fully effective only in the case of perfect thermal symmetry of the measuring system. In this case, however, the measured signal is zero. In real measurements there are always asymmetries in the temperature field. Even in the empty state, when there are no sample capsules, the temperatures of the furnaces are not equal so that a residual temperature difference will arise, which may change with temperature during a scan run. As a consequence, the empty DSC produces a measured curve, which is indeed neither zero nor constant with temperature but has an apparatus-dependent curved shape $\Phi_0(T)$. This so-called zeroline, which is mostly measured with empty furnaces in the calorimeter, is a function, which is additive to the measurement signal which stems from the sample processes. In every real case, this function should be subtracted from the measured curve before following analysis. Therefore it will be correct to insert the term $\Phi_M - \Phi_0$ instead of Φ_M. The zeroline shows the thermal behavior of the measuring system itself and the degree and influence of unavoidable asymmetries. The smaller its range of variation with temperature, the better is the instrument. For highly precise measurements, the zeroline must be determined prior to and after every measurement.

1.2.2. DSC data analysis

Normally the heat flow rate versus the sample temperature is plotted, but it is also possible to calculate other quantities from the originally measured values. The DSC curve (the measured curve, Figure 10) offers quick information on the total measuring process.

The baseline (dashed line in Figure 10) is the part of the heat flow rate curve produced of the DSC during steady state conditions (no reactions or transitions in the sample). The baseline is the sum of the zeroline and the heat flow rate caused by the difference of heat capacities on the sample and reference side in scanning mode.

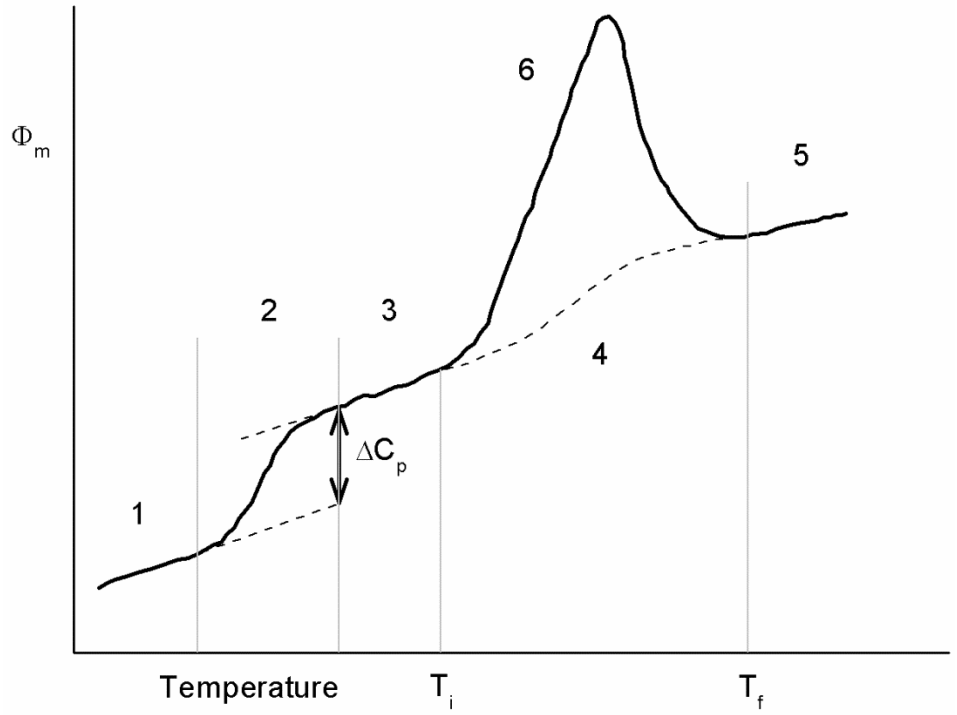

Figure 10. Curve measured by a DSC with step (C_p change) of the baseline (dashed line) and endothermic peak (1st order transition). ΔC_p is a change of sample's heat capacity, T_i and T_f are initial and final peak temperatures. The measured curve has the following parts: initial segment (number 1), step due to ΔC_p (number 2) and the measured curve after step (number 3), number 4 indicates interpolated baseline (between T_i and T_f in the peak region), final segment (number 5) and peak of the measured curve (number 6).

A peak in the measured curve appears when the steady state is disturbed by thermally activated heat production or consumption in the sample (e.g., from transitions or reactions). Peaks in heat flow rate curves, which are assigned to endothermic processes, are normally plotted "upwards" (positive direction), as heat added to a system is defined as positive in thermodynamics by international convention. A peak begins at T_i (first deviation from the baseline), ascends/descends to the peak maximum/minimum, and merges into the baseline again at T_f. Only processes associated with a heat (e.g., melting or crystallization) lead to peaks (except for changes in the heat transfer between the sample and the ΔT-sensor). Other transitions (e.g., glass transition) only lead to changes in the shape of the measured curve, for example step-like changes.

The interpolated baseline is the line which in the range of a peak is constructed in such a way that it connects the measured curve before and behind the peak as if no reaction heat had been exchanged, i.e., as if no heat (peak) had developed.

To get the true sample heat flow rate the zeroline must be subtracted from the measured heat flow rate: $\Phi_S = \Phi_M - \Phi_0$. After that the determination of the baseline is easy (no curvature). The remaining heat flow rate curve will be almost straight and horizontal (outside thermal events). Then

the step-like changes of the heat capacity, weak exothermic events, changes of the heat capacity during transitions (melting, crystallization) are easily detected and specific heat capacity and thermodynamic quantities can easily be calculated.

When a system absorbs heat Q, depending on the transformation it has, its temperature may vary or not. If the system temperature changes from T_i to T_f during the heat transmission, the heat capacity $C(T)$ is defined as $\delta Q/dT$, and its unit is $J \cdot K^{-1}$. Using this definition the specific heat capacity C_p is easily calculated from the measured heat flow rate with the zeroline subtracted:

$$C_p = \frac{C}{m} = \frac{\delta Q_S/_{dt}}{m \,.\, dT/_{dt}} = \frac{\Phi_S}{m \cdot \beta} = \frac{\Phi_M - \Phi_0}{m \cdot \beta} \tag{28}$$

In other words the specific heat capacity is the sample heat flow rate divided by sample mass (m) and heating rate (β). As the latter quantities are given and constant for a DSC run, the C_p curve and the Φ_S curve are identical beside a constant factor. The unit of C_p is $J \cdot K^{-1} \cdot g^{-1}$ and the suffix "p" states for pressure constant quantity.

Qualitative C_p measurements are intended to provide information regarding the glass temperature. The material can be obtained in the glassy state by cooling it at a fixed rate. The glass transition is characterized by an appropriately defined glass transition temperature T_g. Within the transition region many macroscopic properties, which may have great practical importance, change their values (viscosity, dielectric and especially mechanical properties). Each of these could form the basis of an experimental determination of T_g. With DSC the glass transition is detectable by a step change of the heat capacity ΔC_p on heating or cooling. Both the temperature and magnitude of this event are important. Usually the evaluation of the glass transition temperature we do on heating run.

The main parameters used to characterize the glass transition are depicted in Figure 11. For many applications it is important to know the temperature range T_g^i to T_g^f over which the substance vitrifies on cooling, or devitrifies on heating. Unfortunately, the practical determination of these temperatures is problematic, there are large errors in their definition and it is difficult to give clear instructions for their measurement. The situation is improved if clearer, more characteristic temperatures from the transition region are used. These are the extrapolated onset-temperature T_g^e (analogous to the peak onset temperature) and the half-step temperature $T_g^{0.5}$ related to the C_p change (the temperature at which C_p is midway between the extrapolated heat capacity functions

of the glassy and liquid state). The use of the latter is more meaningful as this temperature is better related to the second characteristic quantity of the glass transition, the C_p change.

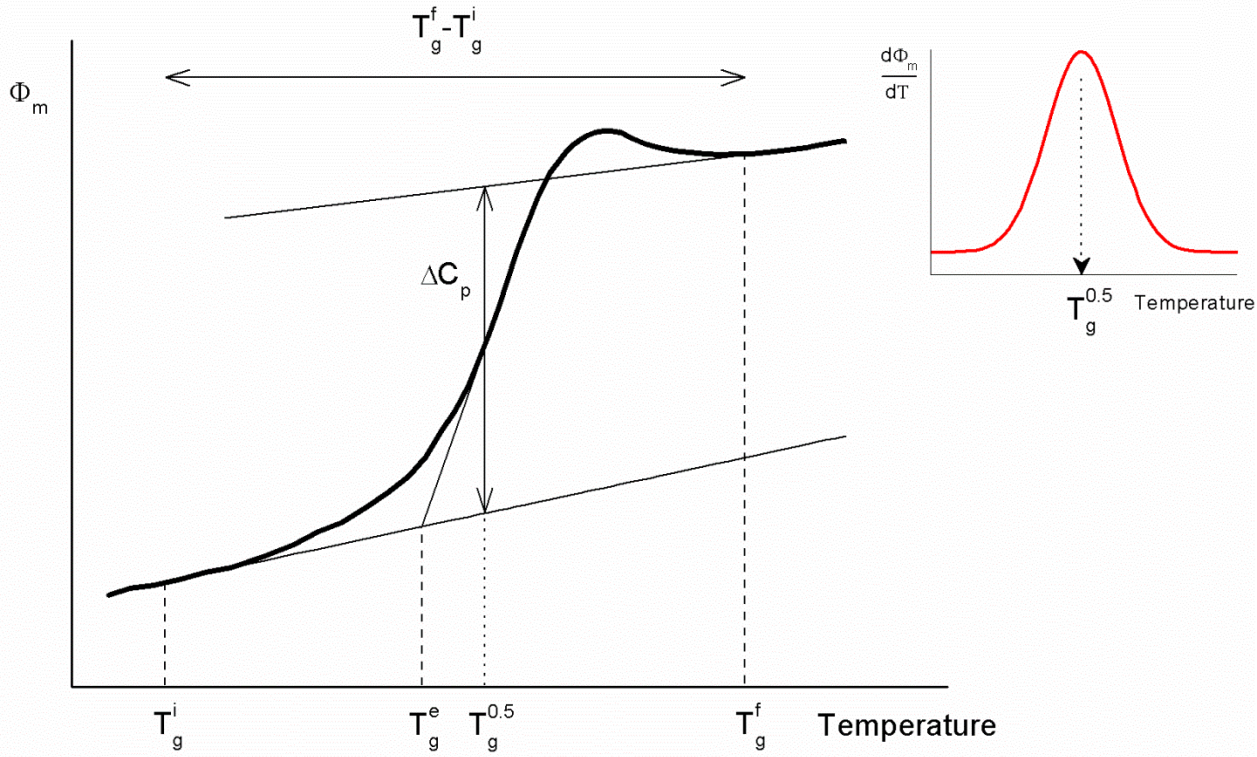

Figure 11. Definition of the most frequently used conventional quantities for characterization of the glass transition. T_g^e is an extrapolated onset temperature, $T_g^{0.5}$ is a half-step temperature, ΔC_p indicates C_p-change at $T_g^{0.5}$, T_g^i and T_g^f are initial and final temperatures and $T_g^f - T_g^i$ is a temperature interval of the glass transition. *Inset*: thermogram derivative curve for precise determination of $T_g^{0.5}$.

T_g^e and $T_g^{0.5}$ can both easily be obtained from routine measurements, this is the reason for the nearly exclusive use of these pragmatically defined glass transition temperatures. A repeatability error of ±1 K is acceptable in practice. The glass transition can be accompanied by "enthalpy relaxation peak". This appears on heating curve as endothermic event at the high temperature end of the glass transition range.

The glassy (or vitreous) solid is, thermodynamically, far from equilibrium. The formation and behavior of a glass are exclusively kinetic events. There are only formal similarities between the C_p-change at an "ideal" glass transition and at a thermodynamically well-defined second order transition. Only the liquid state at the high temperature end of the glass transition is at equilibrium and thermodynamics is valid in this region. The system passes through a sequence of non-equilibrium states during heating or cooling. The typical asymmetric shape of the glass transition curve (an extensive tail on the low temperature side and a fairly abrupt end at high temperatures) is

due to a distribution of the intrinsic variables which vitrify (or devitrify) over a wide range. In contrast to the measurement of equilibrium transitions, it is not possible to get "equilibrium" values of the characteristic quantities T_g and ΔC_p by extrapolation to zero heating or cooling rates: these quantities are determined by the thermal history (scanning rates). If, for instance, the cooling rate is changed by an order of magnitude T_g will change by 3 to 20 K depending on the material in question. T_g depends on the heating rate, by contrast ΔC_p shows much less dependence on thermal history.

1.2.3. Experimental setup

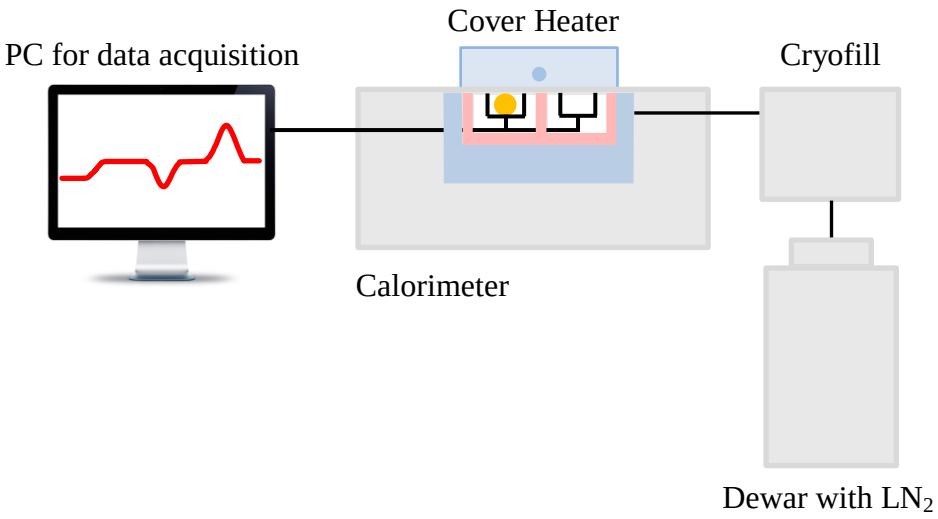

Figure 12. Simplified scheme of the experimental setup for differential scanning calorimetry.

Figure 12 shows the common configuration of the experimental setup with following parts: differential scanning calorimeter, cooling device Cryofill, dewar with liquid nitrogen (LN_2), computer. The common for all DSC software Pyris is used for instrument control and data acquisition.

Perkin-Elmer Company (Massachusetts, USA) offers one of the best calorimeters - the Diamond DSC. Its design with two small furnaces enables the system to achieve the fastest heating and cooling rates (up to 500°C/min), providing better resolution and higher sensitivity, enabling detection of transitions that are missed in conventional DSC systems. The Diamond DSC is designed using the unique power compensation approach.

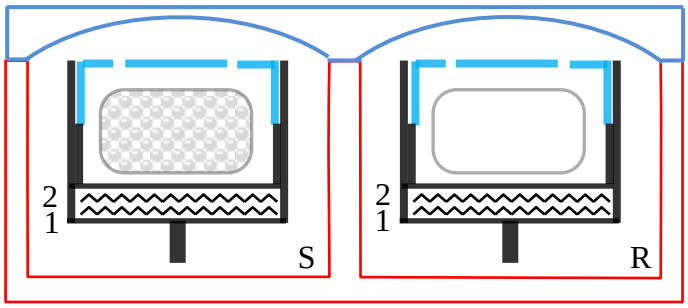

Figure 13. Schematic set-up of the measuring system. S indicates a sample measuring system with microfurnace (black), vented lid (light blue) and capsule (grey); R indicates a reference measuring system (analogous to S). 1 is a heating wire, 2 is a resistance thermometer. Both measuring systems – separated from each other – are positioned in a heat sink (red) at constant temperature and closed by rotating cover (blue). The left capsule contains a sample, the right capsule is empty.

The Diamond DSC sample holder is on the top of the instrument and sits underneath the enclosure of cover heater. There are two low-mass (less than 1 g) platinum-iridium sample microfurnaces (Figure 13) embedded in a large thermostated aluminum heat sink (isoperibol operation). Each of the microfurnaces contains a temperature sensor (platinum resistance thermometer) and a heating resistor (made of platinum wire). The left furnace is used for encapsulated sample; the right furnace is used for reference material. For example, the right furnace is typically an empty sample capsule. Vented platinum lids are used to cover both the sample and the reference microfurnaces.

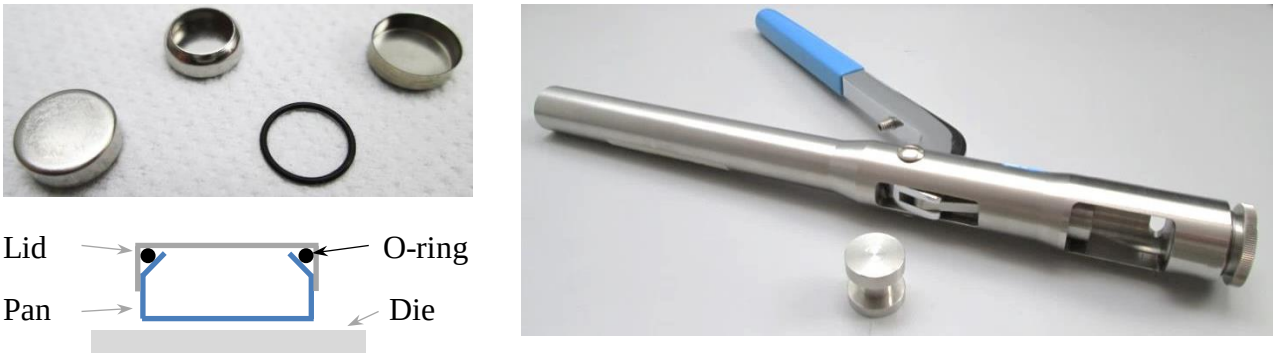

Figure 14. *Left panel*, *upper part* (left to right): 60 µl closed sample capsule consisting of a pan, o-ring, and lid; *lower part*: schematic side view of the capsule. *Right panel*: quick press and spacer die.

The sample capsules of large volume (60 microliters) were used to insert a material for analysis. Large sample capacity yields higher sensitivity. The capsule is made of a stainless steel and contains a pan, lid, and o-ring (Figure 14, left panel). The Viton rubber o-ring allows formation of a seal which suppresses the vaporization of a solvent throughout an experiment. I pursued the idea to maximize the contact surface between capsule and material to reduce the resistance of the material to heat flow though the temperature sensors. The pan and lid are joined by squeezing them between two parallel surfaces. The pressing device must be adjusted to obtain the proper capsule dimention and to assure a good seal. This can be accomplished using the quick press and the spacer die (Figure 14, right panel). The quick press consists of a stainless steel body containing a screw-adjustable bottom die and a lever-arm operated upper die. The positioning of the bottom die to effect a proper capsule seal can be done by preparing a standard spacer using an empty sample capsule.

For a possibility to operate in the very low temperature range, up to −170°C, at the calorimetric instrument an automated cooling system Cryofill is used. This is an intermediate device between dewar and calorimeter; to the latter it is connected by a cryo hose. Prior to performing

subambient measurements the Cryofill pumps LN_2 from dewar to the calorimeter. It should be noted that Diamond DSC provides a wide temperature range from −170°C to 730°C. For the higher temperature measurements it is necessary to change the environment from "Cryofill" to "Water Bath" in the software.

The DSC uses two peripheral gases during operation (Figure 15). The nitrogen gas (pressure 2 bar) is supplied to the Cryofill in order to fill with LN_2 a suitable bath inside of the calorimeter. An electronic system controls the nitrogen level in the thermal bath. The nitrogen gas is used also as shield gas (Block Purge) for the thermostated heat sink, which is immersed in LN_2 bath (by blue in Figure 12). The layer of gas ensures a smooth temperature "blanket" for contact of the system with LN_2. Before the N_2 gas passes through a filter dryer to remove residual moisture, carbon dioxide, and other impurities from it. On the rear corner of the DSC there is a secondary pressure regulator between the filter dryer and the shield gas inlet which controls the amount of gas flow when the cover heater is opened. Thus, the nitrogen gas flow prevents external moisture and particles from entering the sample holder and maintains a constant atmosphere inside. The N_2 gas is inert, inexpensive and readily available.

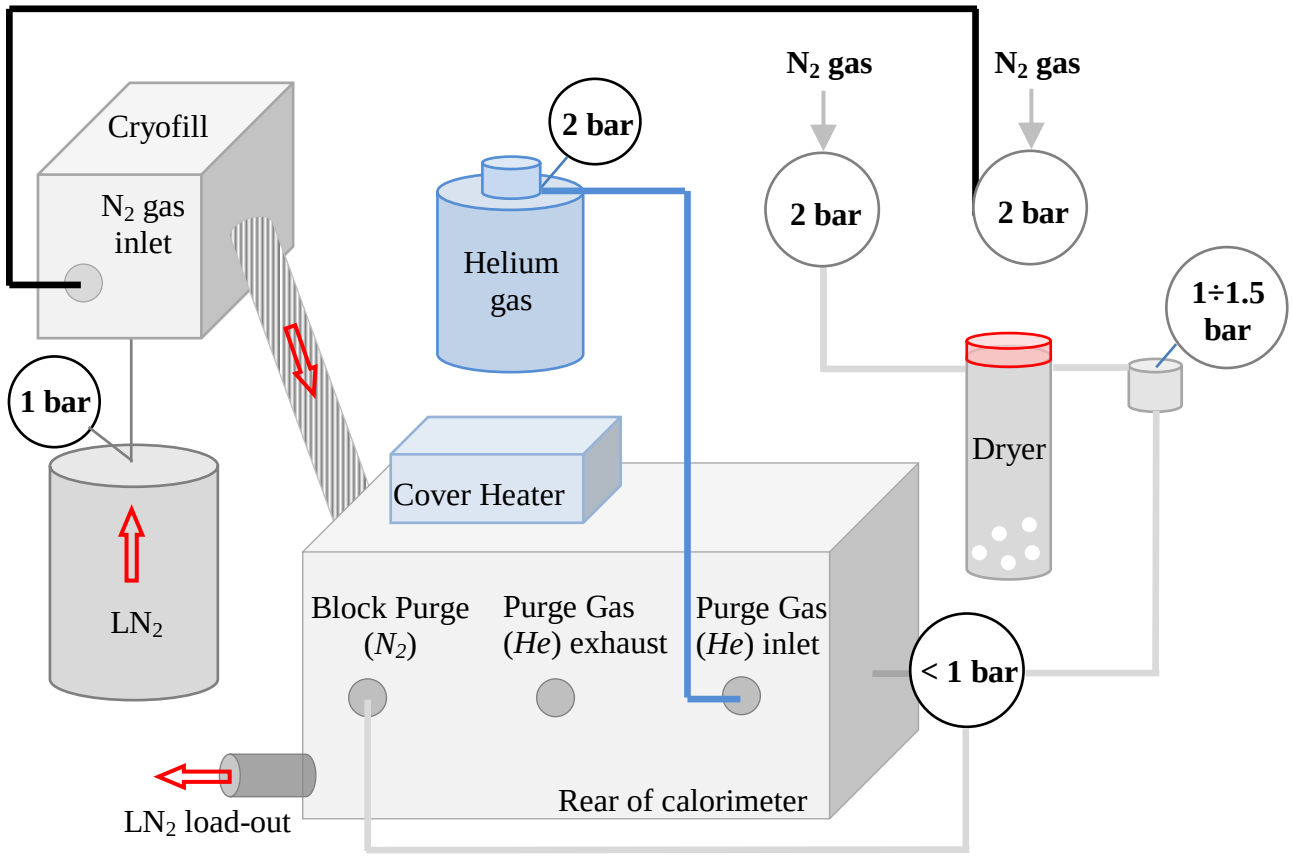

Figure 15. The detailed scheme of gases flow at the DSC.

The second, helium gas is recommended as a purge gas for samples when performing subambient analyses and is supplied to the sample holder. (At subambient runs nitrogen gas will liquefy at temperatures near −196 °C or earlier). Since helium is highly thermally conductive, it helps to cool the sample capsule, so that faster cooling rates may be achieved. However, at high temperature measurements the He gas tends to sweep heat away from the sample reducing sensitivity. This flowing only inside the sample holder gas also helps to remove moisture or oxygen which may accumulate there.

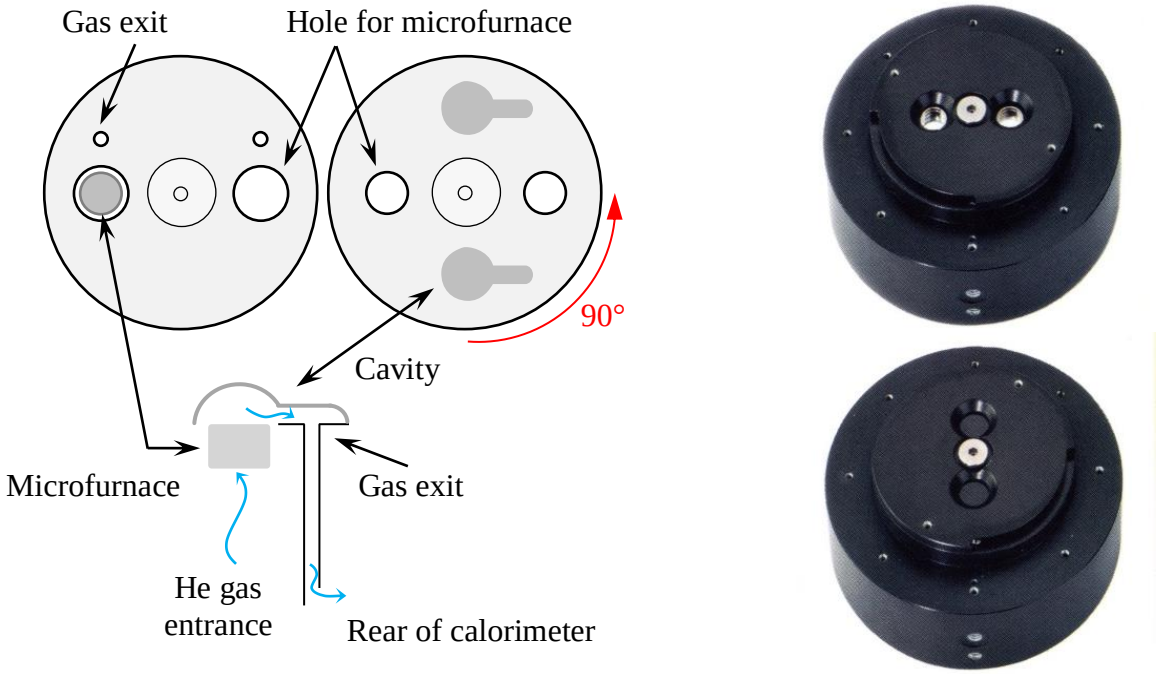

Figure 16. *Left panel*, *upper part*: schematic top view of heat sink (left) and rotating cover (right); *lower part*: side view of closed microfurnace with helium gas flow. *Right panel*: DSC heat sink with rotating cover at opened (upper picture) and closed microfurnaces (lower picture).

The Diamond DSC system includes a unique sample cover design that improves both ease-of-use and performance (Figure 16). An innovative rotating cover effortlessly slides in and out of position. The cover is in a constant contact with the furnace block, reducing equilibrium times and ensuring baseline stability. The top cap of the rotating cover and an outer ring (Danac) around it are heated by pressing “Cover Heater” button on the software control panel that effectively eliminates furnace frosting.

About 15 minutes is needed to fill the calorimeter bath with LN_2. After that in order to have the system in equilibrium it is useful to wait 1 hour before making the instrument calibration and calorimetric measurements.

The calibration procedure of the calorimeter has following steps: baseline adjustment, temperature calibration, heat flow calibration and furnace calibration. The first step is performed manually to level the DSC curve and slope, but it should be done only when a substantial change in the hardware component or system setup has occurred. For the temperature and heat flow calibration a highly pure metal standard as indium with melting temperature 156.6°C and enthalpy of fusion (ΔH) 28.45 J/g is usually used. The last step is a furnace calibration which performed at the empty furnaces overall temperature region.

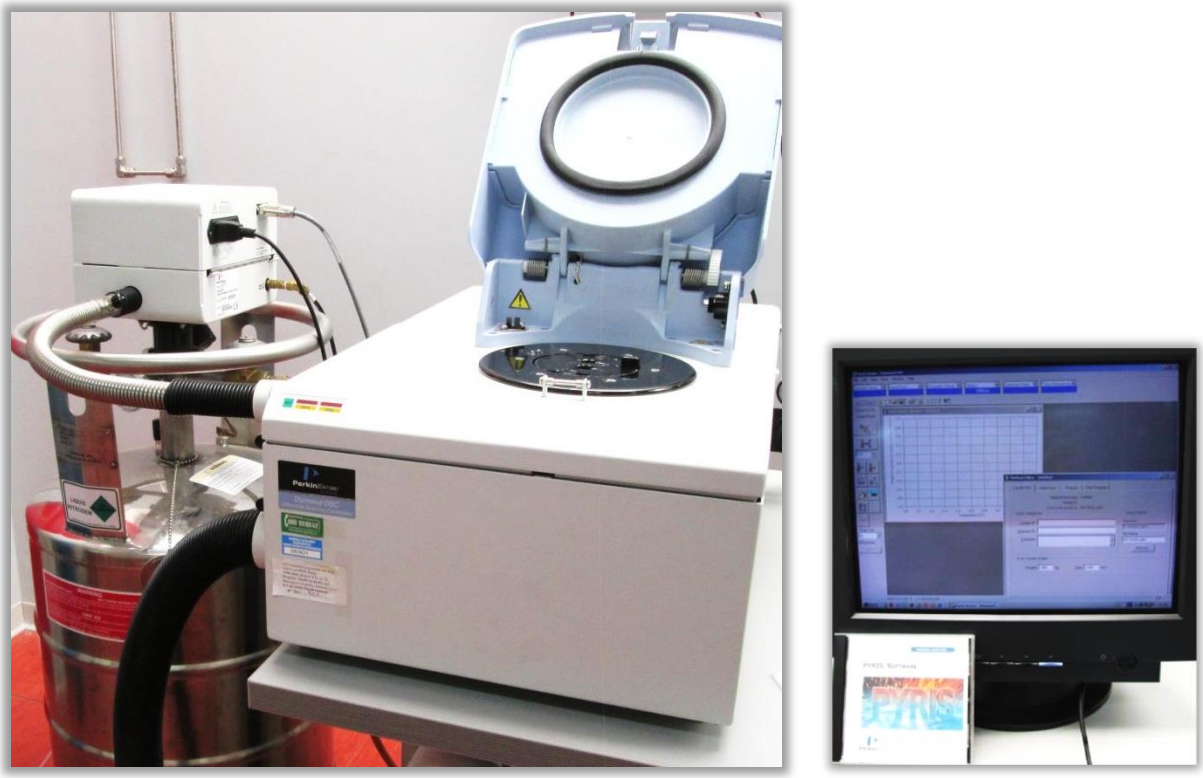

Figure 17. Perkin-Elmer Pyris Diamond DSC that was used to carry out all calorimetric measurements.

1.3. Elastic, Quasi-Elastic and Inelastic Neutron Scattering

Neutron diffraction (elastic scattering) is used for determining material's structure: atomic positions, lattice matrix and symmetry. Inelastic neutron scattering is used for the study of particle's motion (atomic vibrations and other excitations) in space and time. Quasi-elastic neutron scattering is a limiting case of inelastic neutron scattering. This type of scattering assumes a spectrometer with high energy resolution and then it is possible to investigate the processes occurring with a distribution of energies, such as rotations, translations.

1.3.1. Theoretical background

The neutron scattering is a scattering of free neutrons by matter. As an experimental technique this process is used for the investigation many important features of matter - particularly condensed matter.

The nuclear reactor provides an intense flux of neutrons because of a nuclear chain reaction at the heart of the reactor. The interaction of neutron with a heavy isotope, e.g. such as ^{235}U, gives a start of fission chain reaction of isotope's nucleus which releases a large amount of energy and ejects several free neutrons. Inside of the reactor vessel a heavy water (D_2O) at about 35°C is used as coolant and moderator. The result of latter is to produce neutrons with a Maxwellian wavelength distribution, i.e. with $\lambda = 4 \div 1$ Å, and which are called thermal neutrons ($T = 60 \div 1000$ K, $E = 5 \div 100$ meV) [**33**]. To produce high thermal neutron flux the temperature of the moderator is about 300 to 350 K. To produce cold neutrons ($\lambda = 30 \div 3$ Å, $T = 1 \div 120$ K, $E = 0.1 \div 10$ meV) a 25 litre liquid deuterium fridge is used.

By neutrons it is possible to determine the relative positions and motions of atoms in a bulk sample of solid or liquid. The usefulness of thermal neutrons arises from the basic properties of the neutron: mass $m = 1.675 \cdot 10^{-27}$ kg, charge is 0, spin is ½, magnetic dipole moment $\mu_n = -1.913\ \mu_N$ (nuclear magneton). The neutron mass results in the de Broglie wavelength of thermal neutrons ($\lambda = 1.8$ Å at the standard velocity $\upsilon = 2.2$ km·s^{-1}), being of the order of interatomic distances in solids/liquids, thus yielding information on a scattering system structure. Then, uncharged neutron penetrates deeply into a target and comes close to the nuclei (no Coulomb barrier). Hence, neutrons interact with atomic nuclei via nuclear forces which are very short range - few fermis (1 fermi = 10^{-15} meter) and having a magnetic moment the neutrons interact also with the unpaired

electrons in magnetic atoms via a magnetic dipole interaction. The energy of thermal neutrons (E = 25.3 meV at the standard velocity) is of the same order as that of many excitations in condensed matter. So when the neutron is inelastically scattered by the creation or annihilation of an excitation, the change in the energy of the neutron is a large fraction of its initial energy. Measurement of the neutron energies thus provides accurate information on the energies of the excitations, and hence on the interatomic forces.

Consider a beam of thermal neutrons, all with the same energy E, incident on a target-sample (Figure 18, left panel). The sample is a general collection of atoms and it can be called the scattering system. Various types of measurement can be made on the neutrons after they have interacted with the scattering system. The results in each case can be expressed in terms of a quantity known as a cross-section (σ), measured in barns (1 barn = 10^{-28} m^2), that is equivalent to the effective area presented by the nucleus to the passing neutron. The total scattering cross-section is defined by the equation:

$$\sigma_{\text{tot}} = \frac{\text{neutrons scattered per second in all directions}}{\Phi} \tag{29}$$

where Φ is the flux of the incident neutrons, i.e. the number through unit area per second, the area being perpendicular to the direction of the neutron beam. If count all neutrons scattered only into the solid angle dΩ, the cross-section corresponding to these measurements is known as the differential cross-section and is defined by

$$\frac{d\sigma}{d\Omega} = \frac{\text{neutrons scattered per second into } d\Omega}{\Phi d\Omega} \tag{30}$$

If measure the scattered neutrons also as a function of their energy, the partial differential cross-section should be defined by the equation

$$\frac{d^2\sigma}{d\Omega dE} = \frac{\text{neutrons scattered per second into } d\Omega \text{ with energy between } E \div E + dE}{\Phi d\Omega dE} \tag{31}$$

The scattering of neutrons by nuclei is a quantum-mechanical process. Formally, the process has to be described in terms of the wave functions of the neutron and the nucleus. Let's represent neutrons incident on a fixed nucleus by a wave function e^{ikx}, which is a plane wave of unit amplitude

propagating along the x axis; $k = 2\pi/\lambda$ is a neutron wave vector that points along the neutron's trajectory. Because the scattered neutron wave is isotropic, its wave function can be written as $(-b/r)e^{ikr}$ if the scattering nucleus is at the origin of coordinate system. The constant b, referred to as the scattering length of the nucleus, measures the strength of the interaction between the neutron and the scattering nucleus. The minus sign in the wave function means that b is a positive number for a repulsive interaction between neutron and nucleus. Since the nucleus is fixed, the neutron cannot impart kinetic energy, thus, the scattering occurs without any change of the neutron's energy, ΔE = 0, and is said to be elastic. Because the neutron energy is unchanged by a nuclear collision, the magnitude of its velocity and thus of its wave vector is also unchanged. When neutrons are scattered by matter, the process can alter both the momentum and the energy of the neutrons and the matter. The scattering is not necessarily elastic as it is for a single and fixed nucleus because atoms in matter are free to move to some extent. As is usual in a collision, the total momentum and energy are conserved: when a neutron is scattered by matter, the energy lost by the neutron, is gained by the sample. From the neutron momentum, $m\vec{v} = h\vec{k}/2\pi$ (h is Planck's constant), it is easy to see that the amount of momentum given up by the neutron during its collision, the momentum transfer, is $\frac{h}{2\pi}\vec{Q} = \frac{h}{2\pi}(\vec{k}_i - \vec{k}_s)$, where $\vec{k}_i$ is the wave vector of the incident neutrons and $\vec{k}_s$ is that of the scattered neutrons. The quantity $\vec{Q} = \vec{k}_i - \vec{k}_s$ is known as the scattering vector. The angle 2θ is an angle through which a neutron is deflected during the scattering process; generally, it is referred to as the scattering angle. For elastic scattering $\vec{k}_i = \vec{k}_s$, so ΔE = 0 and a trigonometry applied to the scattering triangle shows that $|Q| = 4\pi\,\lambda^{-1}\sin\theta$.

In neutron scattering experiment the intensity of neutrons scattered by matter as a function of the variables Q and E is measured. To relate the intensity of the scattered neutrons to the relative positions and the relative motions of atoms in matter there are scattering effects of two types. The first is coherent scattering in which an incident neutron wave interacts with all the nuclei in a sample in a coordinated fashion; that is, the scattered waves from all the nuclei have definite relative phases and can thus interfere with each other. This type of scattering depends on the relative distances between the constituent atoms and thus gives information about the structure of materials. Elastic coherent scattering gives information about the equilibrium structure, whereas inelastic coherent scattering (with $\Delta E \neq 0$) provides information about the collective motions of the atoms, such as those that produce vibrational waves in a crystalline lattice. In the second type of scattering, incoherent scattering, an incident neutron wave interacts independently with each nucleus in the sample; that is, the scattered waves from different nuclei have random, or indeterminate, relative phases and thus cannot interfere with each other. Rather the intensities from

each nucleus just add up. Incoherent scattering may be due to the interaction of a neutron wave with the same atom but at different positions and different times, thus providing information about atomic diffusion.

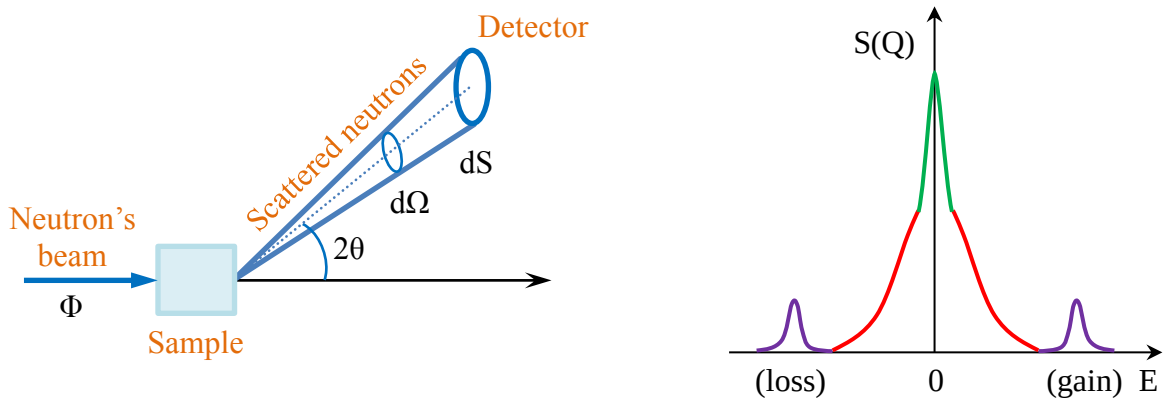

Figure 18. *Left panel*: geometry for scattering experiment; Φ is a flux of incident beam, 2θ is a scattering angle, dΩ is a solid angle and dS is a detector's area. *Right panel*: schematic example of neutron scattering spectrum, where elastic (green), quasi-elastic (red), and inelastic (violet) contributions are depicted.

To be more precise, if the nuclei of the target although being of the same atomic species have different scattering lengths b_j (in general b depends on the relative orientations of neutron and nuclear spins), one can write:

$$b_j = \langle b_j \rangle + \mathrm{d}b_j \tag{32}$$

with $\langle \mathrm{d}b_j \rangle = 0$ and $\langle \mathrm{d}b_j \mathrm{d}b_k \rangle = \delta_{jk} \langle (\mathrm{d}b_j)^2 \rangle$

Then, one can define the coherent and incoherent cross sections as:

$$\sigma_{\mathrm{coh}} = 4\pi \langle b^2 \rangle \tag{33}$$

$$\sigma_{\mathrm{inc}} = 4\pi (\mathrm{d}b)^2 = 4\pi [\langle b^2 \rangle - \langle b \rangle^2] \tag{34}$$

The coherent and incoherent cross sections can be very different and vary from atom to atom. In this thesis we will take advantage of the fact that the incoherent cross section of the hydrogen atom is much larger (~ 80 barns) than the coherent or incoherent cross sections of other atoms in our samples (including the coherent cross section of H atom itself), so that we are essentially observing the incoherent scattering originating from the H atoms in our samples. It can be shown also that

$$I_{\text{inc}} = \left.\frac{d^2\sigma}{d\Omega dE}\right|_{\text{inc}} \propto \int_{-\infty}^{+\infty} \mathrm{d}t\; e^{i\omega t}\langle e^{-iQ[R_k(0)-R_k(t)]}\rangle \tag{35}$$

is the intensity of the incoherent scattering contains information on the self-correlation function of the same particle at different times, i.e. on the atomic diffusion.

1.3.2. Measurement and data analysis

1.3.2.1. Elastic Neutron Scattering

ENS temperature scans were performed at the thermal backscattering spectrometer IN13 (see section 1.3.3.1) with an incident wavelength λ = 2.23 Å and an energy resolution of 8 μeV FWHM.

Mean square displacements (MSDs) of non-exchangeable H atoms of Mb were obtained from neutron scattering function as described in Ref. **34**. Briefly, according to the Gaussian approximation [**35**], the following definition was used:

$$\begin{aligned} I(Q,T,E=0) &= \frac{S(Q,T,E=0)}{S(Q,T=20\text{K},E=0)} = \exp\left[-\frac{\langle u^2\rangle(T)-\langle u^2\rangle(20\text{K})}{6}Q^2\right] \\ &= \exp\left[-\frac{\langle \Delta u^2\rangle(T)}{6}Q^2\right] \end{aligned} \tag{36}$$

where $S(Q,T,E)$ is the dynamic structure factor, i.e., the neutron scattering intensity as a function of momentum transfer (Q), temperature (T), and exchanged energy (E); $\langle u^2\rangle$ is the total mean square displacement of protein hydrogen atoms. Note that from now on the symbol E will denote the exchanged energy that in the previous paragraph was denoted by ΔE. MSD is therefore obtained as:

$$\text{MSD}(T) = -6\cdot\frac{\mathrm{d}\ln I(Q,T,E=0)}{dQ^2} \tag{37}$$

$I(Q,T,E=0)$ is the normalized scattering intensity at the elastic line, defined by the width of resolution function (8 μeV), in the limit of the Gaussian approximation when Q → 0 [**36**].

For ENS experiments with water confined in silica xerogel we used the high hydrostatic pressure equipment developed at the ILL [**37**] for neutron scattering studies of powder and solution samples. The cylindrical cell, built of the high-tensile aluminium alloy (7049-T6), is 4 mm thick and can withstand pressure loads up to 1.5 kbar. To transmit homogeneously the pressure we used Fluorinert™ liquid [**38**] that has a pour point of 178 K and was tested to be completely inert. This avoids using gas for pressure transmission and therefore possible artefacts arising from gas diffusion inside the matrix pores; on the other hand, Fluorinert diffusion was excluded by weighting the sample before and after the measurements. The stick was put inside the closed cycle dry cryostat of the backscattering spectrometer IN13 [**39**] at the ILL and cooled down to 210 or 250 K. When the temperature was reached, the compressor of the cryostat was stopped, as to avoid the cold point and thus freezing of the liquid transmitting the pressure. The temperature was controlled to stay constant along the data collection time. We measured each pressure and temperature point for 5-8 hours, at 210 and 250 K, for pressure values between 20 and 1200 bar in steps of 300 bar.

MSD of confined water were obtained from elastic spectra using equation 37. Limiting the analysis to $Q \leq 1.1$ Å^{-1} allows to neglect contributions arising from rotational motions [**15**] so that, in the diffusion limit, MSD is related to the translational diffusion coefficient D by the Einstein relation:

$$\mathrm{MSD} = 6 \cdot D \cdot \tau_{\mathrm{res}} \tag{38}$$

where $\tau_{\mathrm{res}} = 100$ ps for IN13.

1.3.2.2. Quasi-Elastic Neutron Scattering

The quasi-elastic temperature (190 ÷ 300 K) scans were performed at the cold neutron backscattering spectrometer SPHERES (see section 1.3.3.2) with an incident wavelength λ = 6.27 Å and an energy resolution of ~0.65 μeV FWHM. The setting allows to access the momentum transfer range $0.2 < Q < 1.8$ Å^{-1}.

QENS spectra I(E, Q = 0.6 Å^{-1}) were fitted with the following simplified function:

$$I(E, Q = 0.6\ \text{Å}^{-1}) = [y_0 + B \cdot E] + \left[\frac{A_1}{w_1\sqrt{\frac{\pi}{2}}} \cdot e^{-2\frac{(E-E_0)^2}{w_1^2}}\right] + \left[\frac{2A_2}{\pi} \cdot \frac{w_2}{4(E-E_0)^2 + w_2^2}\right] \tag{39}$$

where A_1 and A_2 are area, $w_1 \cdot \sqrt{ln4}$ and w_2 are FWHM. The first part is a linear function which serves to take account of background, the second part is Gauss function for describing the elastic contribution and the third part is Lorentz function for QENS contribution.

1.3.2.3. Inelastic Neutron Scattering

Measurement

INS experiments were performed at the time-focusing time-of-flight spectrometer IN6 (see section 1.3.3.3) with an incident wavelength $\lambda = 5.1$ Å and an energy resolution of 70 μeV FWHM. The setting allows to access the momentum transfer range $0.3 < Q < 2$ Å^{-1}. The inelastic spectra $S(Q = 1.8$ Å^{-1}, E), where E denotes the exchanged energy, were obtained by binning all the measured spectra in the interval $1.6 < Q < 2.0$ Å^{-1}. In view of the relation between energy and momentum transfer ranges in a time-of-flight spectrometer, the choice of this Q region allows to explore the largest energy range accessible. Given the large incoherent cross section of hydrogen, the (coherent + incoherent) contributions from Si and O atoms and the coherent contribution of H atoms were neglected so that the measured inelastic spectra were considered to arise only from the incoherent scattering of hydrogen atoms.

Analysis

From the physical point of view, the measured inelastic spectra were considered to arise, besides the matrix contribution, from the sum of the following contributions:

1. An elastic contribution arising from nuclei that are at rest in the time window of the experiment and given by a Dirac delta function convoluted with the experimental resolution; in view of the energy resolution used in our experiment (~70 μeV FWHM) the elastic contribution is essentially zero for $E > 0.1$ meV.

2. A quasi-elastic contribution arising from diffusive-like translational and rotational motions occurring in the picoseconds-to-nanosecond time scale. In our approach the analysis of this contribution remains heuristic and is performed with two Lorentzian functions. Note that, at temperatures below 180 K, the quasi-elastic contribution is almost absent and that, above 180 K, its amplitude and width increase monotonically with temperature (see Figure 38, right panel).

3. An inelastic contribution arising from low frequency collective vibrations (the so-called Boson peak (BP); for a discussion on the physical origin of the BP in supercooled water and in deeply cooled confined water see, e.g., Refs. **40** and **41** and references therein). As already proposed in the literature [**42**], we account for this contribution with an asymmetric lognormal term.

The function used to analyze the experimental spectra has the following form:

$$S_{\text{exp}}\left(E, Q = 1.8\ \text{Å}^{-1}\right) = M(E) + \frac{1}{\pi}\cdot\frac{A_1\gamma_1}{E^2+\gamma_1^2} + \frac{1}{\pi}\cdot\frac{A_2\gamma_2}{E^2+\gamma_2^2} + \frac{A_3}{\sqrt{2\pi}\sigma_{BP}E}\cdot\exp\left[\frac{-(E_{BP}-\ln E)^2}{2\sigma_{BP}^2}\right] \quad (40)$$

where M(E) accounts for the matrix contribution, as described above. Note that the term M(E) contains no adjustable parameters since its amplitude depends on the sample hydration level but not on temperature. A_1, γ_2, A_2, and γ_2 are the amplitudes and halfwidths, respectively, of the two Lorentzian terms L_1 and L_2 used to describe the quasi-elastic contribution; σ_{BP} and E_{BP} are the width and position, respectively, of the asymmetric lognormal term that describes the BP shape. The fitting is performed in the energy range 0.1 < E < 15 meV, where the tail of the elastic peak (resolution function) can be neglected. The Debye-Waller factor arising from harmonic vibrations is included implicitly in the amplitudes of the various terms in Eq. (40); it will be considered explicitly only in the derivation of the density of states (see below). The inelastic spectra were analyzed with a FORTRAN 95 code based on the Minuit minimization routine released by the CERN computing group (*lcgapp.cern.ch/project/cls/workpackages/mathlibs/minuit/index.html*).

From the lognormal term we obtain the vibrational density of states (VDOS), g(E), according to

$$g(E) \sim \frac{E\cdot\frac{A_3}{\sqrt{2\pi}\sigma_{\text{BP}}E}\cdot\exp\left[\frac{-(E_{\text{BP}}-\ln E)^2}{2\sigma_{\text{BP}}^2}\right]}{n(E,T)\cdot DW(T)} \quad (41)$$

$$n(E,T) = \frac{1}{\exp\left(\frac{E}{k_{\text{B}}T}\right)-1} \quad (42)$$

where $n(E,T)$ and $DW(T)$ are the Bose occupation factor and the Debye-Waller factor, respectively. $DW(T) = \exp(\langle u^2\rangle\cdot Q^2)$ is calculated, following a well-established approach, from the $\langle u^2\rangle$ mean square displacements obtained with elastic scans performed "ad hoc" in the 5 ÷ 100 K temperature range (data not shown), where the system is harmonic and $\langle u^2\rangle$ is linear with

temperature, and assuming the same linear dependence at higher temperatures. As usual, the VDOS is divided by E^2 to enhance the excess contribution over the Debye level (reduced vibrational density of states, R-VDOS). The intensity, position, and variance of $g(E)/E^2$ are then calculated according to

$$M_0 = \int \frac{g(E)}{E^2}\, dE \tag{43}$$

$$M_1 = \frac{\int E \cdot \frac{g(E)}{E^2}\, dE}{M_0} \tag{44}$$

$$M_2 = \frac{\int E^2 \cdot \frac{g(E)}{E^2}\, dE}{M_0} - M_1^2 \tag{45}$$

1.3.3. Experimental setup

Identical aluminum sample's containers of rectangular shape with surface area 4 × 3 cm^2 and sample thickness 0.5 mm have been used for the whole set of neutron scattering experiments except for one where the dependence on pressure was investigated (Figure 19).

Figure 19. 600 µl opened sample cell for neutron scattering experiment consisting of a pan with indium fiber along its perimeter and lid with screws.

1.3.3.1. IN13

The elastic neutron scattering temperature scans were performed at the thermal backscattering spectrometer IN13 (Institut Laue-Langevin, Grenoble, France). Because of its high energy resolution (8 µeV) and high momentum transfer ($Q < 4.9$ $Å^{-1}$) the backscattering spectrometer IN13 is particularly useful for the microscopic study of single particle motions (jump reorientation, rotational and translational diffusion, tunnelling) observed by incoherent neutron scattering.

The monochromator and analyser $CaF_2(422)$ crystals are oriented in near backscattering geometry thereby achieving an energy resolution of a few µeV (Figure 20). The energy of the incident neutrons (E_i) is scanned by variation of the temperature of the monochromator (T) at a fixed Bragg-angle (Figure 20, inset). In an optional mode the 10 mm thick monochromator crystals are kept at a fixed temperature gradient and energy variation is performed by scanning the monochromator Bragg-angle. This achieves an increased flux at the sample position and slightly increases the energy resolution width.

A vertically curved Graphite deflector focusses the beam onto the sample. The scattered neutrons are energy analysed by a set of seven spherically curved composite crystal analysers, each covering a large solid angle of 0.18 sr. An additional three circular analysers centred around the transmitted beam cover the small-angle region.

The neutron time-of-flight is used to suppress (i) the background of neutrons scattered directly from the sample into the detectors and (ii) second order contamination.

The neutrons are counted with a cylindrical multidetector consisting of 35 ^{3}He detector tubes, arranged in staggered circular rows. The small Q range from 0.2 to 0.8 Å^{-1} is covered by a ^{3}He Position Sensitive Detector (PSD) arranged to see the circular analysers in exact backscattering.

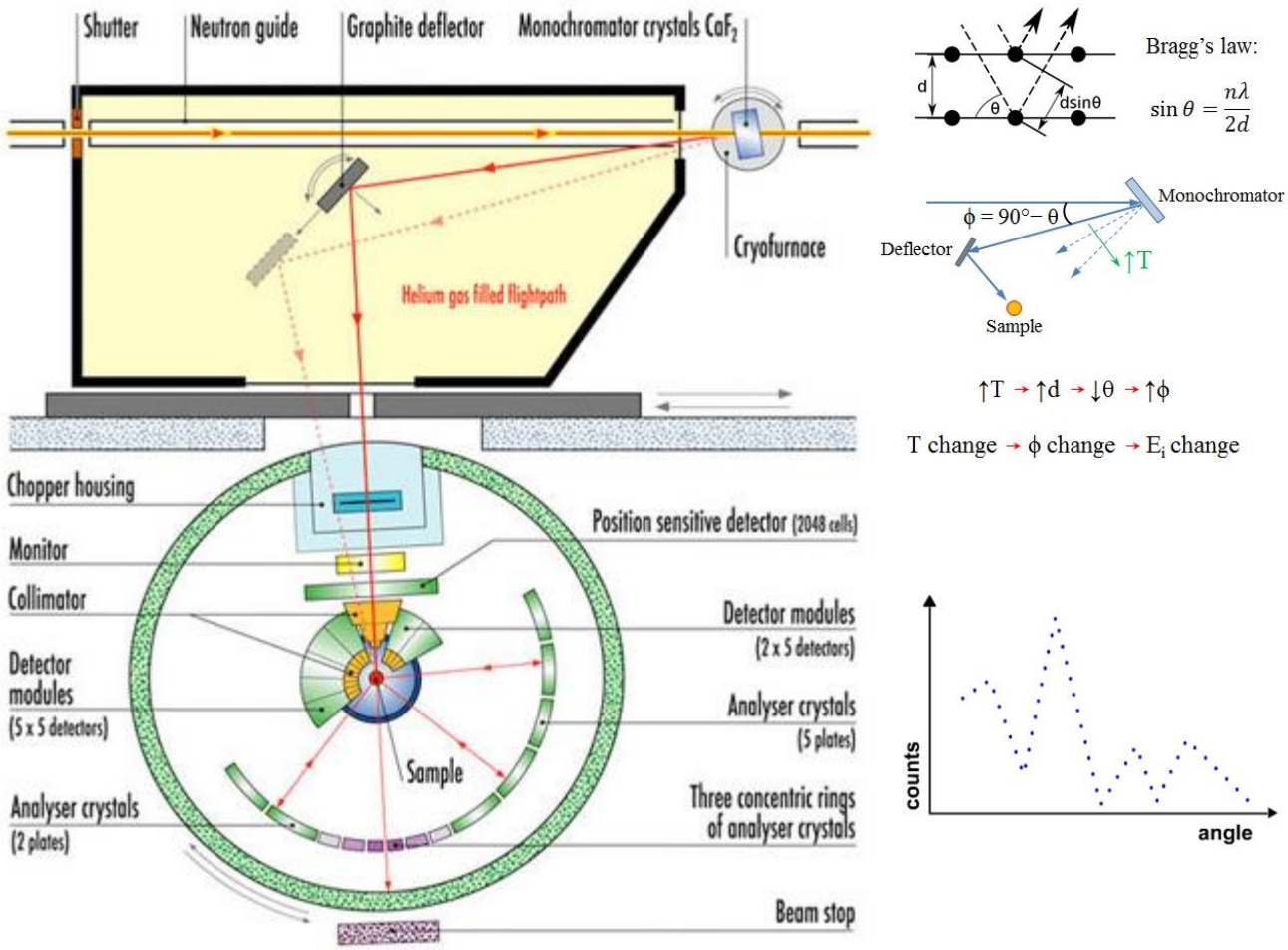

Figure 20. Layout of the thermal neutron backscattering spectrometer IN13. *Inset*: Temperature gradient monochromator (upper panel); simple schematic plot illustrating the experimental raw data (lower panel).

The incoming polychromatic neutron beam (wavelength λ = 2.23 Å) is backscattered on the monochromator (Bragg reflection on a crystal lattice) with a high monochromaticity (energy resolution 10 μeV). The beam is reflected so as to hit the sample. The scattered neutrons are analysed by a Bragg reflection on the analysers. A chopper creates "bursts" of neutrons, so as only those neutrons that have travelled from the sample to the analysers and back to the detectors are counted. The energy transfer between the neutron hitting the sample and the neutrons scattered by

the sample is monitored by varying the monochromator temperature (with reference to the analysers temperature which remains almost constant). Elastic scattering ($\Delta E = 0$) or inelastic scattering (ΔE up to ~200 μeV) is analysed as a function of the scattering angle (Figure 20, inset). This gives access to the dynamical characteristics of the scattering sample, and mostly to the hydrogen atoms it contains.

1.3.3.2. SPHERES

The quasi-elastic neutron scattering measurements were carried out on the high-flux (intensity at the end of neutron guide $8 \cdot 10^9$ n/s and at the sample $7 \cdot 10^5$ n/s) neutron backscattering spectrometer, located at the 20MW German neutron source FRM II (Forschungs (research) Reaktor München) in Garching. The beamline instrument is named SPHERES which is backronym for SPectrometer for High Energy RESolution.

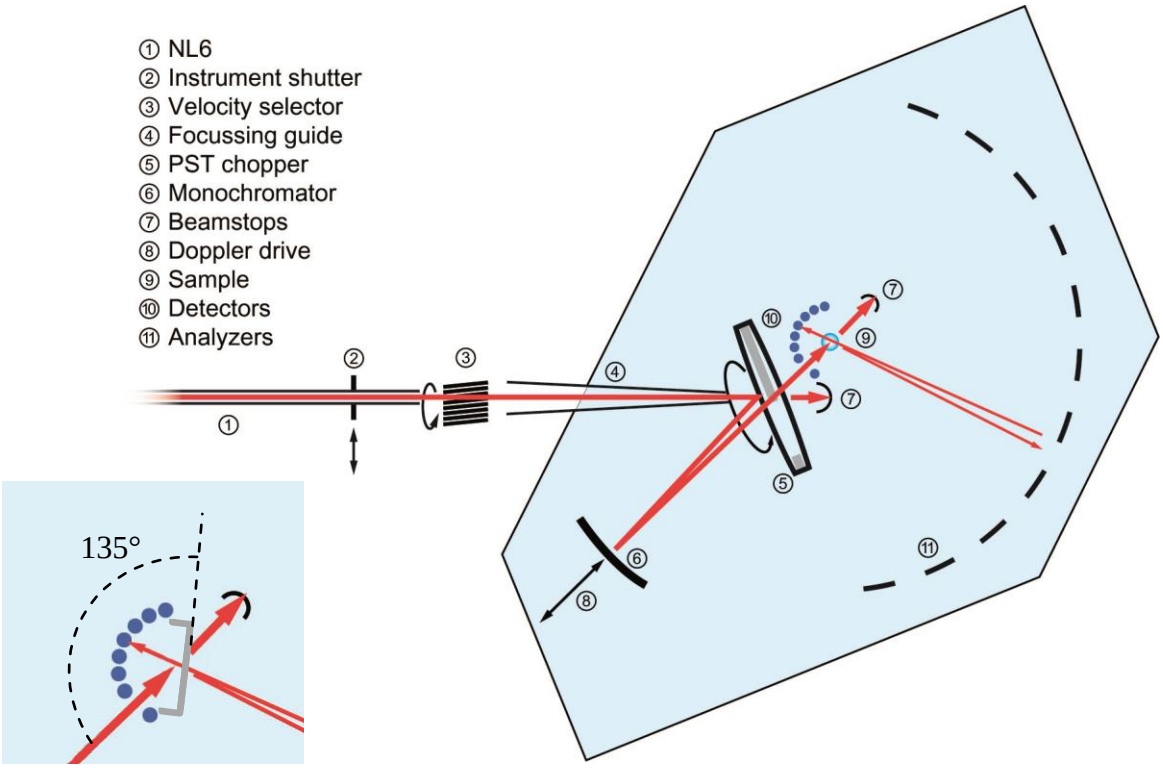

Figure 21. Layout of the backscattering neutron spectrometer SPHERES. *Inset*: zoom in of sample cell (grey) position.

The instrument layout is depicted in Figure 21. SPHERES receives neutrons from the cold source. The velocity selector reduces the incoming neutron spectrum to final neutron wavelength $\lambda_f = 6.27 \pm 0.34$ Å [**43**]. It is followed by a convergent neutron guide that reduces the beam section

by a factor of 11.5 to 25 × 25 mm^2. In a backscattering spectrometer, strong energy filtering of incident and scattered neutrons is achieved by Bragg reflection from perfect monochromator and analyzer crystals (silicon (111)) under angles close to 180°. This peculiar geometry entails the need for a primary beam deflector and a duty-cycle chopper. The phase-space transform (PST) chopper is the key component of a third-generation backscattering spectrometer because combines these two functionalities. Half of its circumference bears deflector crystals (pyrolitic graphite) that redirect incoming neutrons towards the monochromator. The angle between incoming and deflected beam is about 42°. The other half circumference is open. When the chopper is open, neutrons coming out of the neutron guide are transmitted towards a beam stop that is integrated in the chopper housing, and neutrons coming back from the monochromator are transmitted towards the sample.

The resonance-free monochromator Doppler drive is used at the spectrometer configuration to change the energy transfer. Driven by a linear motor, the monochromator shell performs a sinusoidal motion. The maximum frequency is about 10 Hz, resulting in maximum velocity amplitude of 4.7 m/s. In the rest frame of the monochromator, backscattering neutrons have the final velocity v_f = 630.9 m/s with the final neutron energy E_f = 2.08 meV. In the laboratory frame, they have the energy

$$E_i(v) = \frac{m_n}{2}(v_f + v)^2 \tag{46}$$

where v is the monochromator velocity. After monochromator the neutrons are transmitted to the sample, where they are scattered in 4π, but 20% of it is covered with analyzers. The analyzers select scattered neutrons with the energy $E_f = E_i(0)$, which are returned to the sample and then reach the detectors. During the neutron "trip" sample - analyzer - sample the detectors see N pulses of directly scattered neutrons, interlaced with N−1 pulses of energy-analyzed neutrons. In consequence, the sample energy gain in the scattering process is

$$\hbar\omega = E_i - E_f = (2\frac{v}{v_f} + \frac{v^2}{v_f^2})E_f \tag{47}$$

The quadratic term causes a small asymmetry in the dynamic range. With the monochromator's maximum velocity of 4.7 m/s, accessible energy transfers $\hbar\omega$ extend from −30.9 to 31.2 μeV [**43**].

Indirect geometry gives highest resolution with good intensity but limited energy transfer range. The backscattered energy resolution of SPHERES, which is in first approximation a Gaussian with a full width at half maximum of $\Delta E = 0.62 \div 0.65$ μeV. Hence, $\Delta E/E_f \sim 3 \cdot 10^{-4}$ and the resolution time $\tau_{res} \sim h/\Delta E$ is about 6.5 ns.

The detector bank of SPHERES in able to detect scattered neutrons in scattering angle (Θ) range from 9° to 135°.

The sample cell fastens to the standard sample stick and is placed in a cryostat, a closed cycle refrigerator system with cold head and compressor, under 135° to the incoming beam (Figure 21, inset). In the low-temperature range from 4 K to 320 K, the sample is cooled via exchange gas.

The raw data are histograms containing neutron counts per energy channel and per detector. These raw spectra are only a few correction steps away from the physical scattering law $S(Q, E)$.

1.3.3.3. IN6

The inelastic neutron scattering measurements have been performed on a cold neutron time-focussing time-of-flight spectrometer, located at the 58MW French neutron source ILL (Institut Laue-Langevin) in Grenoble. The beamline instrument is named IN6, where letter code IN means Inelastic Neutron scattering.

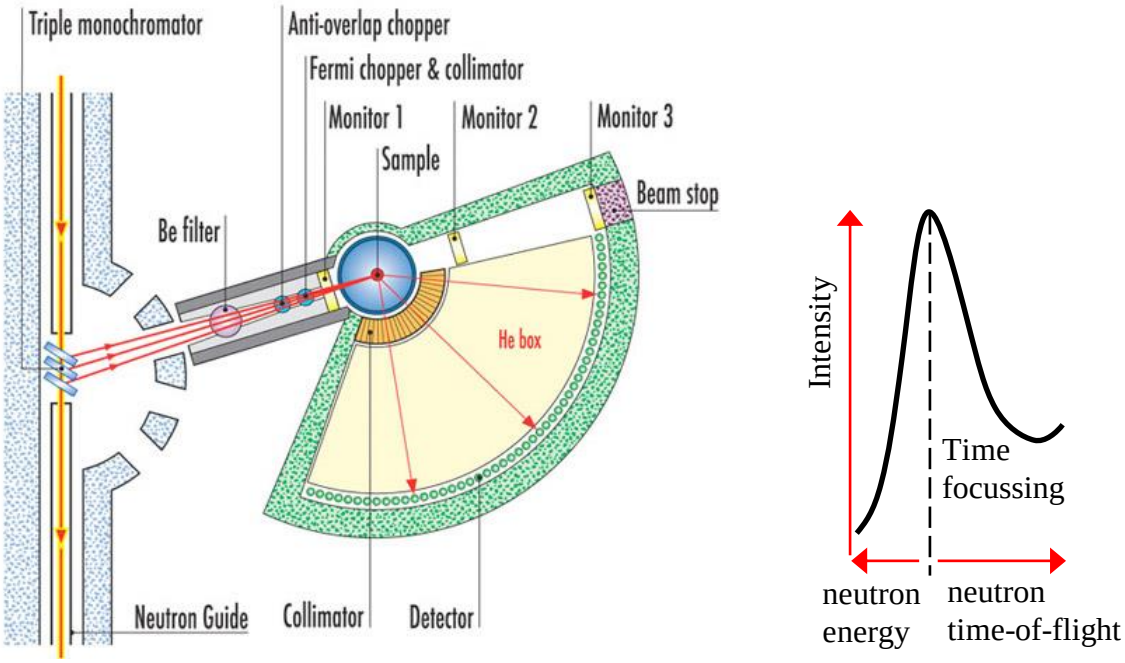

Figure 22. Layout of the time-of-flight spectrometer IN6. *Inset*: simple schematic plot illustrating the work principle.

The instrument layout is depicted in Figure 22. An intense beam is extracted from the cold neutron guide by a vertically focussing monochromator array. It consists of three composite

pyrolytic graphite monochromators and focusses the beam at the sample position. The second order reflection from the graphite monochromator is removed by a beryllium-filter cooled at liquid nitrogen temperature.

To achieve the time-focussing condition, the beam is pulsed by a Fermi chopper. It has a small slot length to ensure a good transmission. To prevent frame-overlap when the chopper is rotating faster than 7500 rpm, a suppressor chopper is placed before the Fermi chopper and rotates in phase with the latter at a lower speed.

The sample stick with attached sample cell is placed in a cryostat. A helium filled box between the sample and the detectors minimises the background. The sample box is equipped with an oscillating collimator which prevents parasitic reflections (from the cryostat walls for example) reaching the detectors. The detector bank is entirely covered with detector boxes, thus avoiding the inconvenience of moving the counters.

The basic of the so called time-focussing technique is following. Three intense neutron beams of $\lambda_i = 5.1$ Å are extracted from a neutron guide by an assembly of three monochromators and are focused horizontally onto the sample. Each monochromator delivers a beam of distinct energy ($E_1 \neq E_2 \neq E_3$) and, thus, of distinct velocity ($\upsilon_1 \neq \upsilon_2 \neq \upsilon_3$) due to different Bragg-scattering conditions. The neutron beams are pulsed by a Fermi chopper which allows the slowest neutrons to pass through first and the fastest neutrons to pass through last. As a consequence, pulses of fast neutrons catch up with pulses of slower neutrons after the chopper. The chopper speed can be adjusted in such a way that all three pulses of different energy arrive at the same time ($t_1 = t_2 = t_3 = t$) in the detectors. Its merit is the increase of intensity by a factor of three ($I \rightarrow 3I$) which corresponds to the number of monochromators.

The interaction of neutrons with a sample changes potentially the velocity of the neutrons. Therefore, if neutrons are scattered by a sample, the time-focussing condition cannot be accomplished in general. Only neutrons of distinct final energies, for example neutrons which are elastically scattered ($\Delta E = 0$) and do not change their velocity ($\Delta\upsilon = 0$), still meet the conditions of time-focussing determined by the corresponding chopper speed. The energy which is exchanged ($\Delta E \neq 0$ or inelastic scattering) between the neutron and the sample can be calculated from the difference in arrival time (Δt) with respect to elastically scattered neutrons at the detector position ($\uparrow t \rightarrow \downarrow\upsilon \rightarrow \downarrow E$). This is the principle of time-of-flight spectroscopy (Figure 22, inset).

The elastic energy resolution (ΔE) of IN6 at incident wavelength of 5.1 Å is 70 μeV and thus, the time resolution $\tau_{res} \sim h/\Delta E$ is about 60 ps. The maximum energy gain of neutrons at the spectrometer can be 200 meV, from that the maximum $\Delta E/E$ is $3.5 \cdot 10^{-4}$.

The detector bank of IN6 in able to detect directly scattered neutrons in the scattering angle (Θ) range from 10° to 115°.

Chapter 2

Investigated systems

2.1. Myoglobin: description and sample preparation

Myoglobin is a reversible oxygen-binding protein found in the muscle tissue of vertebrates in general and in almost all mammals. High concentrations of myoglobin in muscle cells allow organisms to hold their breath for a longer period of time. Diving mammals (whales, seals) have muscles with particularly high abundance of this protein.

It is convenient to use a simple structure protein for protein dynamics investigation. For this reason such paradigm for protein study as myoglobin is used.

Myoglobin was the first protein to have its three-dimensional tertiary structure revealed by X-ray crystallography. This achievement was reported in 1958 by J. Kendrew and associates [**44**]. For this discovery, J. Kendrew shared the 1962 Nobel Prize in chemistry with M. Perutz [**45**].

The globular proteins (spherical shape and water-soluble) have the globin family, which is characterized by the presence of globin fold consisting of eight alpha helices connected by loops. The myoglobin consists of a globin fold with a heme which is buried inside it (Figure 23). The heme is a non-protein chemical compound (cofactor) that is required for the protein's biological activity. Thus, the protein is an enzyme and cofactor can be considered as a "helper molecule" that assists in biochemical transformation. The heme structure is a porphyrin ring with an iron (Fe^{2+}, ferrous) at its center. The porphyrin without a metal-ion in its cavity is a free base, which is a heterocyclic organic ring made up of four modified pyrrolic subunits joined together by methine bridges (=CH–). By the way, the name "porphyrin" comes from the Greek word porphyros, meaning purple. That is why myoglobin is of this color (Figure 24, left panel).

Hemoproteins achieve their remarkable functional diversity by modifying the environment of the heme macrocycle within the protein matrix. The heme group interactions are responsible for the characteristic function of myoglobin, since an isolated heme group does not exhibit the phenomenon of reversible oxygenation. At the myoglobin's heme a proximal histidine group (His-94) is attached directly to iron, and a distal histidine group (His-65) hovers near the opposite face [**46**]. The distal imidazole is not bonded to the iron but is available to interact with the substrate O_2. The binding of O_2 causes substantial structural change at the Fe center, which shrinks in radius and moves into the center of N_4 pocket.

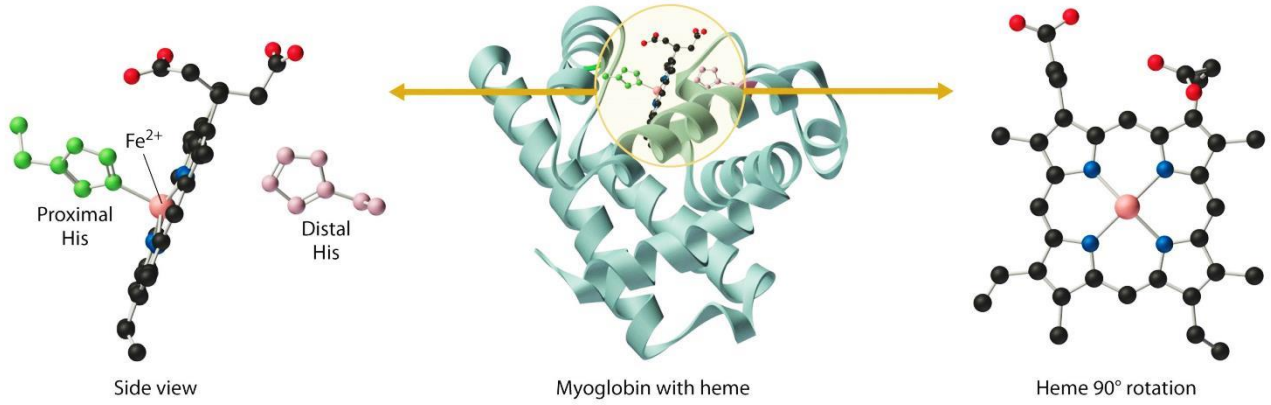

Figure 23. *Middle*: schematic picture of myoglobin and the active site – heme (*right, left*). An iron (Fe^{2+}) in the middle of heme is depicted in pink in complex with four interior nitrogen atoms represented in blue [**47**].

The myoglobin consists of a single polypeptide chain of about 153 amino acid residues, associated with a single heme group. The myoglobin is a protein of low molecular weight; so Mr of myoglobin in equine heart is 16.890 daltons [**48**].

The whole myoglobin structure is folded in a complex and unsymmetrical manner to form a flattened, roughly triangular prism with dimensions about 45 × 35 × 25 Å [**49**]. The whole structure is extremely compact; there is no water inside the molecule, with the probable exception of a very small number (less than 5) of single water molecules presumably trapped at the time the molecule was folded up; there are no channels through it, and the volume of internal empty space is small. The heme group is disposed almost normally to the surface of the molecule, one of its edges (that containing the polar propionic acid groups) being at the surface and the rest buried deeply within.

The side chains almost all those containing polar groups are on the surface. Thus with very few exceptions all the lysine, arginine, glutamic, aspartic, histidine, serine, threonine, tyrosine, and tryptophan residues have their polar groups on the outside (the rare exceptions appear to have some special function within the molecule, e.g. the heme-linked histidine). The interior of the molecule, on the other hand, is almost entirely made up of non-polar residues, generally close-packed and in Van del Waals' contact with their neighbours.

For maintaining the integrity of the whole protein structure the most important contribution comes from the Van der Waals forces between non-polar residues which make up the bulk of the interior of the molecule. There are a number of charge interactions and hydrogen bonds between neighbouring polar residues on the surface of the molecule, but many, or even most, of these are incidental - a polar group on the surface bonds with a water molecule or ion in the ambient solution,

and only links up with a neighbouring side chain without departing too far from its normal extended configuration.

The myoglobin's structure is highly irregular; the seven "corner" regions between helical segments are all different, so that generalization is impossible; the interactions between side chains are numerous and of many different types, and one cannot easily see which are crucial in determining the structure. The complexity of myoglobin is very great, yet it is probably simpler than most proteins, not only by virtue of its low molecular weight, but also in respect of its high helix content, probably much higher than that of most others.

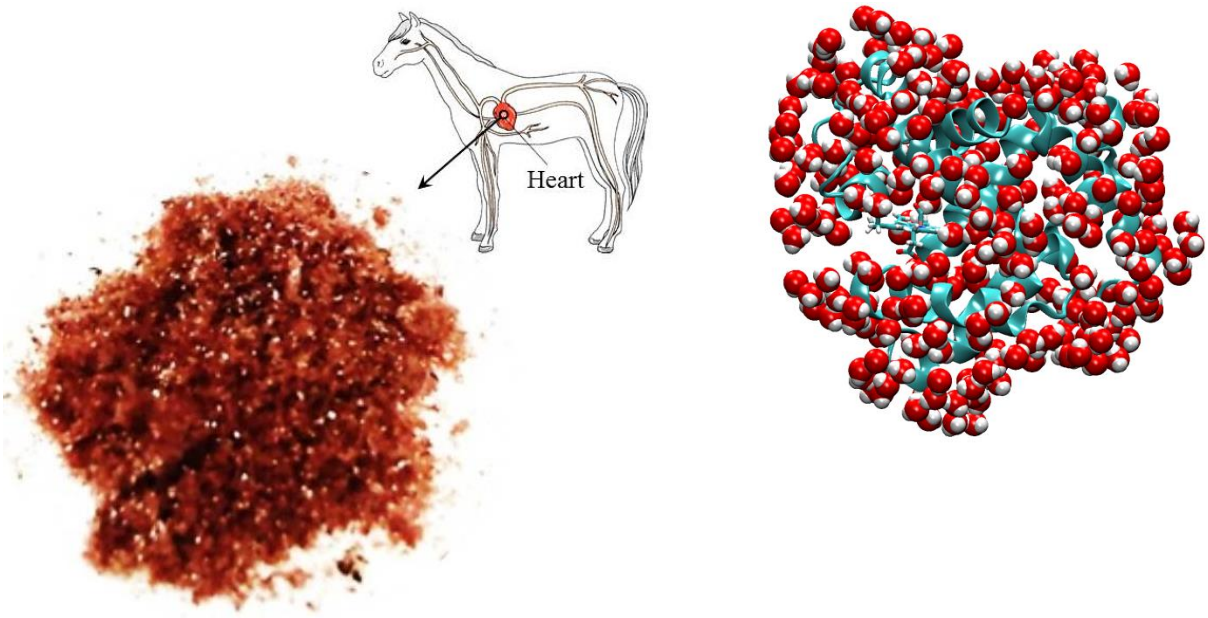

Figure 24. *Left panel*: myoglobin of horse heart. *Right panel*: computer simulation image of myoglobin (cyan) hydrated with D_2O (oxygen by red) at h = 0.3, which corresponds to the 1st hydration shell of the protein surface.

Sample preparation

Lyophilised horse heart myoglobin was purchased from Sigma-Aldrich (St. Louis, MO). Met-Mb hydrated powders for neutron scattering experiments were prepared with the following procedure: a solution of horse Mb in D_2O (concentration 50 mg/ml) was held at room temperature for approximately 24 h, centrifuged for 20 min at 10°C and subsequently re-lyophilised; the resulting powder was held for about 30 h under vacuum at 45°C and considered our dry (h = 0) sample. We are aware of the fact that the above procedure is unable to remove the water tightly bound to charged groups on the protein surface [**50, 51**] and amounting to ~2% w/w. The powder was then held in a controlled N_2/D_2O atmosphere in order to obtain the desired hydration levels (h=gr D_2O/gr protein) that were estimated by measuring the powder mass change.

For calorimetric and dielectric spectroscopy measurements, Hydrogen/Deuterium exchange was achieved by hydration under D_2O atmosphere followed by vacuum drying; this hydration-dehydration procedure was repeated several times (at least 6) so as to guarantee that most of the exchangeable H atoms are replaced by D atoms. This fact was confirmed by NMR experiment. The D-exchanged protein powder was carefully dried under vacuum at room temperature for one day and the obtained powder was considered as our dry (h = 0) sample. Following [**14**], the dry powder was then thoroughly mixed with the desired amounts of D_2O; the mixing procedure was performed by repeatedly adding small amounts of D_2O to the sample until a homogeneous mixture was obtained and the final hydration level h was determined by measuring the mass change of mixture. To further ensure homogeneity, the samples were left to equilibrate for at least 10 days before measurements. Note that this procedure for obtaining hydrated samples is different from that previously used by Schirò et al., 2009 [**52, 53**] for obtaining samples at h = 0.3 and h = 0.5.

2.2. H_2O in silica matrix: description and sample preparation

Other and non-biological system studied in this work, is water embedded in pores of a hydrophilic disordered matrix. This system mimics the protein surface and is a simple and convenient model for the investigation of protein hydration water.

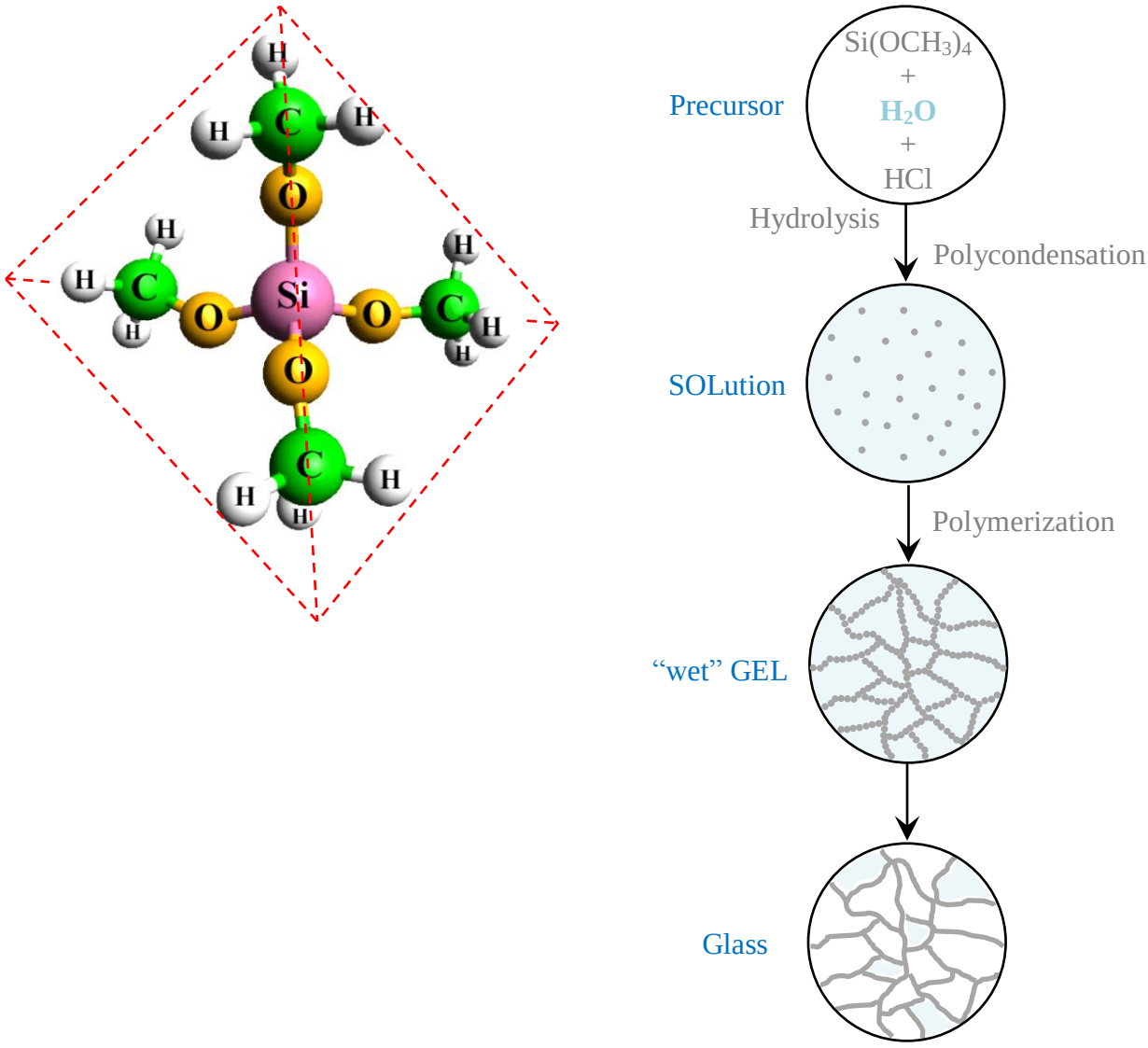

Figure 25. *Left panel*: TMOS molecule in tetrahedron (red dashed line). *Right panel*: summary of the key steps in sol-gel polymerization of TMOS.

A solid silica matrix is obtained with time from a silica gel. The silica gel is obtained by the sol-gel process. The macroscopic process behind this process is a transition from SOL to GEL, i.e. a solution becomes a gel which finally assumes the rigidity of a solid. The microscopic processes such as hydrolysis and polycondensation are the base of sol-gel process. These chemical reactions of metalorganic compounds such as silicon alkoxide compounds occur. A common example for a

silicon alkoxide is the family of tetra alkoxysilanes that have the general form $Si(OR)_4$, where R is an alkyl group and therefore OR is an alkoxy group. A component (precursor) in a starting mixture which was used in the preparation of the silica gel is a monomeric tetramethoxysilane (TMOS) with the formula $Si(OCH_3)_4$ (Figure 25, left panel) and molar mass of 152.2 $g \cdot mol^{-1}$. The four methoxy ($-OCH_3$) groups tetrahedrally bound to silicon (Si, semimetal/semiconductor) are evenly spaced in three dimensions, resulting in a net cancellation of dipole moments. This makes TMOS non-polar and thus immiscible with water. In order to get the two to react HCl was added to the starting mixture.

The first stage of the sol gel process is the hydrolysis reactions (the metal alkoxides interact with water) which facilitate the formation of silanol groups (Si-OH):

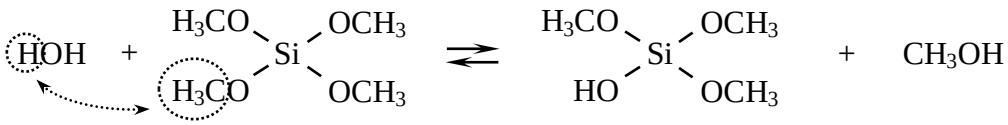

Figure 26. Mechanism for hydrolysis of TMOS.

The hydrolysis can be catalyzed by acidic catalysts in electrophilic mechanism. The reaction rate of the hydrolysis is increased with the strength of the acid, therefore HCl is common catalysts. A complete hydrolysis of $Si(OCH_3)_4$ would give a solution of silanol groups, $Si(OH)_4$, or silicic acid in alcohol, but this does not occur. The second stage of the process consists on polycondensation interactions of the hydrolysis products. The condensation may occur between either two silanols (water condensation) or a silanol and a methoxy group (alcohol condensation) to form a bridging oxygen or a siloxane group (Si-O-Si):

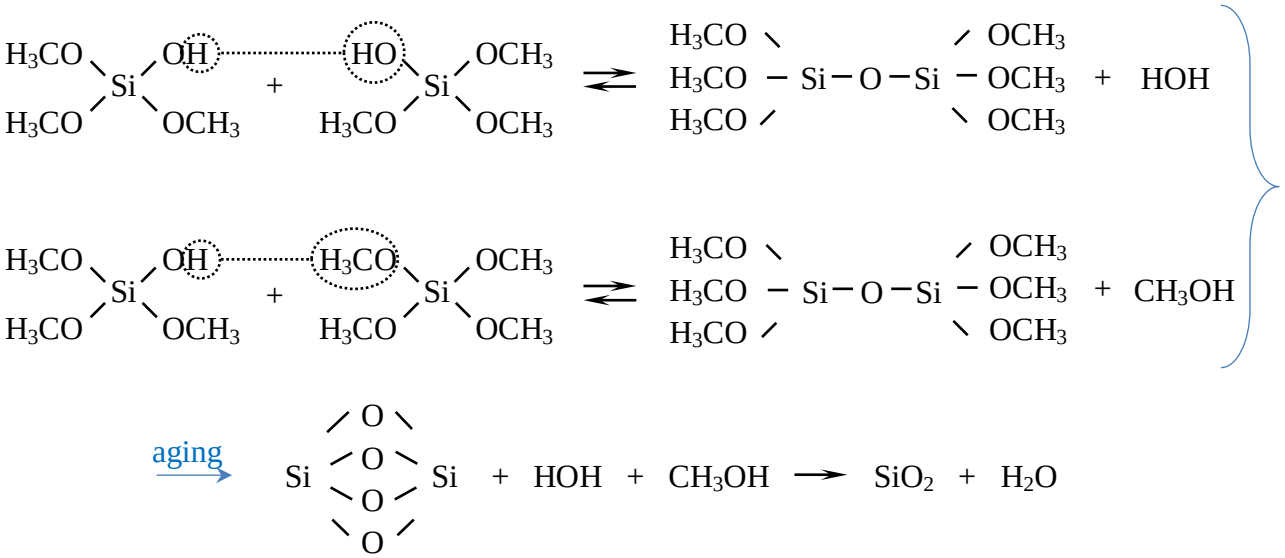

Figure 27. Mechanism for condensation of TMOS.

The result of the polycondensation reactions is the creation of a gel network by cross-linking between silicon and oxygen atoms with the release of water or alcohol (Figure 27).

The whole system does not become a solid in an instant. The sol-gel-solid transition occurs first in small areas where the solid particles are formed in a liquid solution (Figure 25, right panel). Then, slowly these particles meet each other, form a polymer and condense together form the overall silica network ($nSiO_2$) with water contained within its pores ("wet" gel). After the liquid continues to evaporate the gel becomes a solid (but a little amount of liquid remains in its pores). It is a rigid substance can be removed from its original container and stands on its own (Figure 28, left panel). If the liquid part of a hydrogel is removed by evaporation, the empty solid porous matrix remains (xerogel). The shrinkage during drying is often extreme (~90%) for xerogels.

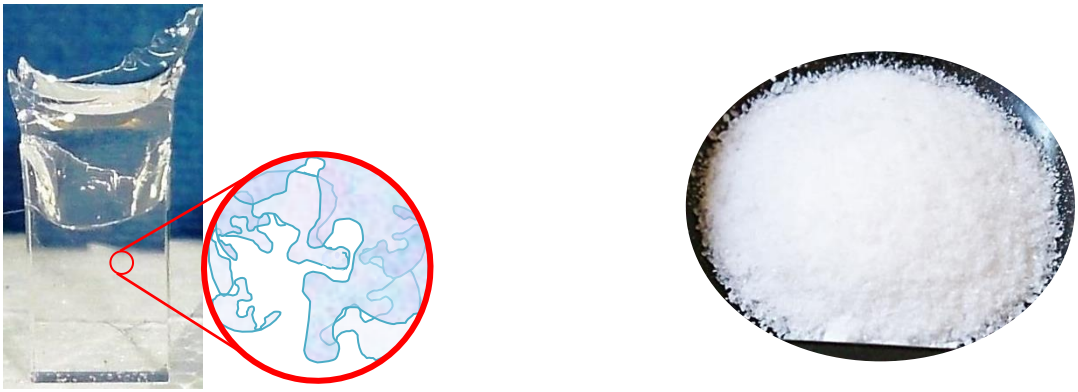

Figure 28. *Left panel*: solid 3D-disordered SiO_2 matrix with water in its pores and schematic representation of microscopic view inside of it (pores with water by blue and empty space by white). *Right panel*: silica powder obtained after crunch of solid matrix from left panel.

Sample preparation

A solution containing 75% (v/v) TMOS (Merck), 20% H_2O (Millipore purified, resistivity of ~18 MΩ cm), and 5% HCl (2×10^{-3} M) is sonicated (for destroying any aggregates) at the frequency of 20 kHz for ~20 min and diluted with an equal quantity of water (final pH 2). After gentle mixing, the resulting sol is poured into semi-micro polystyrene cuvettes (Kartell, 1 cm path length). In these conditions, gelification of the sample occurs in about 1 h at room temperature following two main processes: a hydrolysis and a condensation phase [**54-58**]. After a few days, the "wet" gel sample can be extracted from the cuvette. If the silica hydrogel is left to age at room temperature, it progressively loses weight and reduces its volume until it reaches, after about 15 days, approximately one-seventh of its initial volume. The final dimensions of the slab are about $1.3 \times 0.5 \times 0.24$ cm^3. No further relevant volume contraction is observed upon prolonged aging, although the structure of the matrix and the water content of the hydrogels keep evolving, as shown

by the near-infrared (NIR) absorption spectrum [**27**]. During the aging process the sample hydration h = grams of [H_2O]/grams of [SiO_2] was monitored by weighting; when the desired hydration value was reached the hydrogels were crunched to obtain hydrated powders (Figure 28, right panel); with the used procedure the 3D-disordered, porous, silica matrix has a broad distribution of pore sizes with average dimensions of about 20 Å [**59**]. Three samples have been investigated in this study at hydration levels h = 0.42, 0.19, and 0.05. This last sample was obtained after prolonged vacuum dehydration at 50 °C and was used to obtain the contribution of the "dry" silica matrix (or xerogel). On the other hand, the h = 0.19 sample allows investigating the properties of water mainly interacting with the pore walls, while the h = 0.42 sample gives information also on the internal water.

Chapter 3

Hydration dependence of myoglobin dynamics

3.1. Anharmonic dynamics by neutron scattering

Neutron scattering is a powerful technique to study protein dynamics and energetics. The structure factor S (E = 0, Q, T) of elastic incoherent neutron scattering (EINS) is related to the time-position self-correlation function of protein-solvent nuclei that, in turn, is related to the energy landscape of the system whose different tiers can be explored by the temperature dependence of the EINS signal. In particular, EINS on D_2O-hydrated protein powders, which probes the mean square displacements (MSDs) of protein non-exchangeable H atoms, reveals two deviations from harmonic dynamics, at ~100 ÷ 150 K and at ~220 K [**2, 60**]. Molecular origin, physical nature and biological relevance of these ‘‘transitions’’ are still matter of discussion. The first one is attributed mainly to thermally activated motions of CH_3 methyl groups [**34, 60-63**] (methyl groups activation, MGA). The second one is called “protein dynamical transition” (PDT). Total MSD values of non-exchangeable H atoms of Mb powders differently hydrated as a function of temperature are represented in Figure 29 (left panel, (a)); data relative to the “dry” powder sample are also reported. For dry protein powder no PDT is observed.

I stress that during my thesis work I investigated the temperature dependence of MSD relative to D_2O-hydrated Mb powders at various hydration levels; as already mentioned, my data are shown in the left panel of Figure 29. For the analysis and interpretation of my data I followed the procedure previously developed by Schirò et al. [**8**] and applied to the study of homomeric polypeptides; the main results from Schirò et al. used in the discussion of my data are depicted in the right panel of Figure 29.

To obtain the MSD related to the PDT I adopted the subtraction/normalization procedure developed by Schirò et al., i.e. the MSD measured for the dry sample (h = 0) were subtracted from the MSD measured at a given hydration [**8, 64**]. In this way the contributions related to harmonic motions and to MGA (almost hydration independent [**61**]) are subtracted while contributions related to the PDT are highlighted. ΔMSD values [ΔMSD = MSD(h) − MSD(h = 0)] are represented in the panel (b): a pronounced dependence on hydration is observed, the effect saturating at h > 0.3. To ascertain whether hydration influences the ΔMSD amplitudes or their onset temperature (or both), the ΔMSD were normalized to their high temperature values, i.e. divided by $[MSD(298\ K)_{hydrated} - MSD(298\ K)_{dry}]$; normalized ΔMSD are represented in the (c) panel and one

clearly sees that normalized data superimpose, independent of hydration. This clearly shows that hydration affects the amplitude of anharmonic fluctuations related to the PDT (in agreement with the suggested plasticizing role of hydration water [**65**]), but not the PDT onset temperature that is detected at 220 ± 10 K for all samples (see the blue area in Figure 29, left panel).

The PDT has been first interpreted as a glasslike transition [**2**] directly correlated to the onset of biological activity [**66**], but this view has been later challenged. Several interpretations of the PDT have been proposed: (i) a change in the protein structural flexibility in response to the glass transition of hydration water [**11**]; (ii) a result of the protein structural relaxation reaching the limit of the experimental frequency window [**3-5**]; (iii) the protein response to a fragile-to-strong dynamic crossover in the hydration water at 220 K where water structure makes a low density liquid (LDL) → high density liquid (HDL) transition [**7**]; (iv) a change in the thermodynamic resilience of the water-protein system [**6**]. These models propose physical pictures partially alternative, demonstrating that the question has not been definitively settled yet: (i) and (ii) ascribe the PDT to a temperature dependent relaxation time crossing the instrumental time-scale; (iii) and (iv) interpret the PDT as a change in thermodynamics and structure of the protein-water system. All these hypotheses share the relevant role attributed to the hydration water dynamics: in fact, there is clear experimental evidence that the PDT occurs only in the presence of a sufficient amount of hydration water [**60, 61**]. A key issue is whether and how the onset temperature and amplitude of the detected anharmonic MSDs depend on the time scale probed by neutron spectrometers, i.e., on their energy resolution. Indeed, the answer to this question relies on the nature of the underlying energy surface and, as a consequence, gaining information on the resolution dependence helps in describing the shape of the energy landscape. Moreover, it allows to discriminate among the different hypotheses on the PDT origin listed above: indeed a PDT onset independent of resolution is incompatible with (i) and (ii), while it would support (iii) and (iv).

The experimental evidence on the resolution dependence of anharmonic onsets using homomeric polypeptides was presented by our group [**8**]. The strategy was to use homomeric polypeptides, i.e., chains of one type of amino acid but a number of residues comparable to that of functional proteins, as model systems to catch the molecular details of protein dynamics observed with EINS [**34, 61**]; this overcomes the problem posed by the intrinsic heterogeneity of proteins since it allows to probe the dynamical behavior of each type of residue separately without neglecting the polymeric nature. The hydrated poly-glycine which does not have methyl group and dry poly-alanine having CH_3 group were studied. It was shown that poly-glycine at h = 0.2 undergoes only the PDT while dry poly-alanine shows only the MGA [**34, 61**]. The energy

resolution dependence was investigated by using three different spectrometers (IN16, IN13, and IN6 at the ILL, Grenoble) that allow exploring about two orders of magnitude in energy resolution (FWHM): 0.9 μeV (IN16), 8 μeV (IN13), and 70 μeV (IN6), i.e., the 100 ps ÷ 10 ns time range. The analogous to the previous procedure a subtraction of harmonic from dry poly-alanine and of dry from hydrated poly-glycine contributions and further normalization the obtained ΔMSDs to their room temperature value was performed. For convenience, the figure of that article is demonstrated also in this thesis; see Figure 29 (right panel). The result is that within the resolution range explored, the MGA onset temperature clearly depends on energy resolution while the PDT one does not.

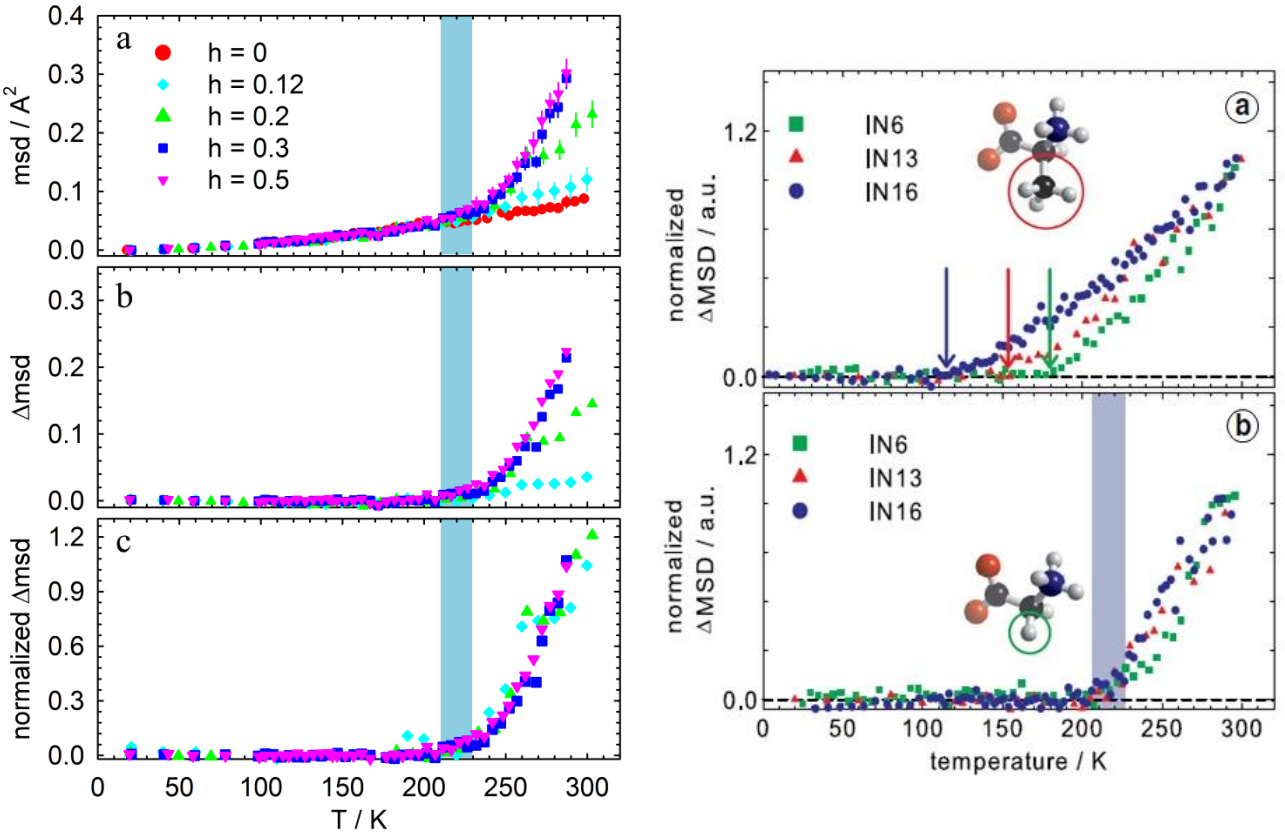

Figure 29. *Left panel*: MSD of non-exchangeable H atoms of Mb hydrated powders as a function of temperature at different hydration levels. Red circles: h = 0; cyan diamonds: h = 0.12; green triangles up: h = 0.2; blue squares: h = 0.3; violet triangles down: h = 0.5. Panels (a), (b), and (c) refer to total MSD, ΔMSD = MSD(h) − MSD(h = 0), and normalized ΔMSD = ΔMSD(T) / ΔMSD(T = 298 K) respectively. The blue zone highlights the temperature intervalwhere the onset of the PDT is observed. *Right panel*: Panel (a): normalized MSD (dry-harmonic) in dry poly-A; the arrows indicate MGA temperatures. Panel (b): normalized MSD (hydrated-dry) in hydrated poly-G; blue area indicates the PDT onset temperature region.

As shown by the blue-shadowed area in the left panel of Figure 29, the onset of the PDT is observed in hydrated Mb powders at the same temperature as in homomeric polypeptides, independent on hydration. Taking together these data with those reported by Schirò et al. 2012 [**8**] on hydrated

powders of Bovine Serum Albumin, one may conclude that the PDT in Mb is a real physical effect and not a mere resolution effect [**3-5, 11**].

3.2. Calorimetric transitions

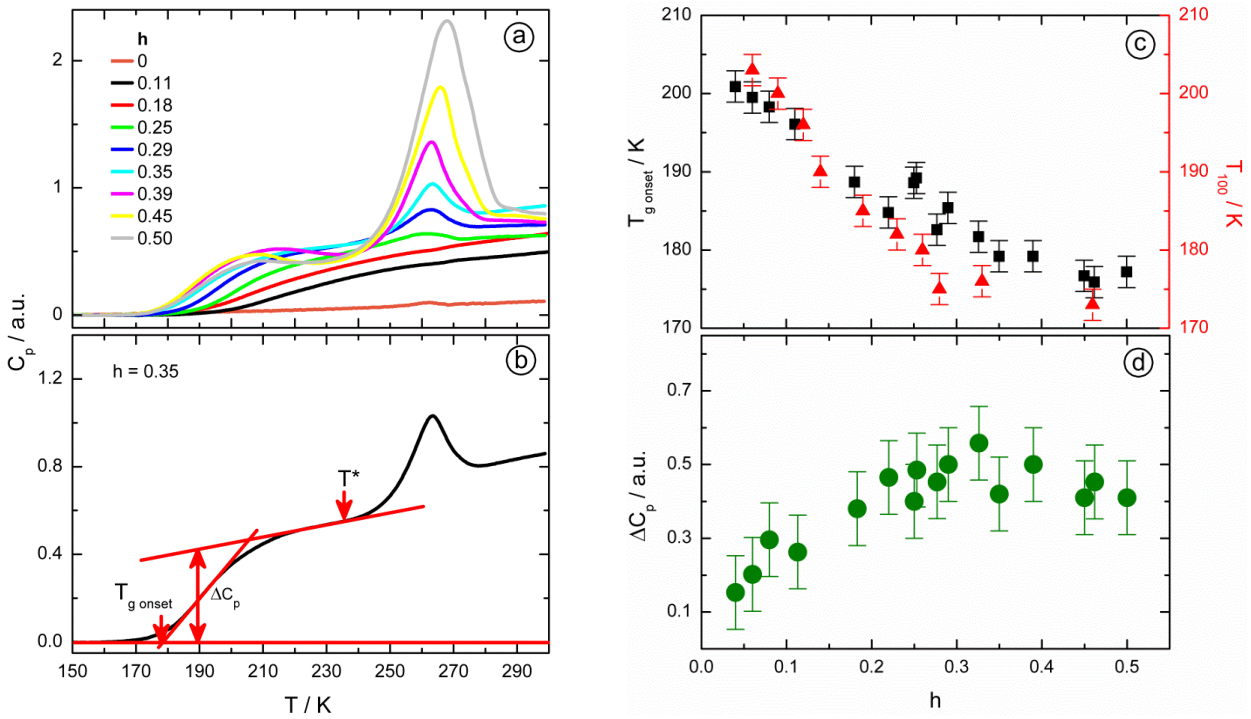

Figure 30. Panel (a): calorimetric upscans (scan rate 20 K/min) of Mb powders at selected representative hydrations; panel (b): pictorial representation of the procedure used to determine T_g onset, T^*, and ΔC_P. Panel (c): T_g onset (black squares, *left scale*) and T_{100} (red triangles, *right scale*) as a function of hydration; panel (d): ΔC_P as a function of hydration.

DSC upscans relative to myoglobin powders at various h values are shown in Figure 30 (panel (a)). Note that a straight line obtained by fitting the data points in the 130 ÷ 170 K temperature interval has been subtracted from the original, baseline subtracted, thermograms in order to highlight the relevant specific heat variations. As can be seen, a glass transition is identified as a specific heat step in the lower temperature region of the thermograms; its onset temperature decreases with increasing hydration while the specific heat leap increases with hydration; both effects tend to reach a plateau at h > 0.30. Panel (b) illustrates the procedure used to determine the glass transition onset temperature ($T_{g\ onset}$) and the specific heat leap (ΔC_P). The absence of any transition in the dry (h = 0) sample (see panel (a)) and the fact that ΔC_P increases almost linearly with hydration in the range 0 < h < 0.3 (see also panel (d)) suggests that the features observed in the hydrated samples refer to hydration water. The hydration dependence of the glass transition related

quantities $T_{g\ onset}$ and ΔC_P is depicted in Figure 30 ((c) and (d)). Interestingly, a broad endothermic peak is observed for samples with h > 0.2. The onset of this peak is independent on hydration and is located at about 230 ÷ 240 K, that is identified as T^*, much lower that the melting temperature of bulk D_2O (~277 K); at the highest hydrations investigated (h > 0.35) the peak broadens significantly towards the high temperatures and likely contains contributions from the melting of heavy water, in agreement with the suggestion that water in excess of the first hydration shell may freeze [**67**].

Data in Figure 30 ((c), (d)) clearly show that the glass transition onset temperature decreases with hydration while the specific heat leap increases; however, both effects tend saturate for hydration levels higher than about 0.3. Considering that, for myoglobin, h = 0.3 corresponds to full coverage of the first hydration shell (Figure 24, right panel) [**68**], this confirms that the glass transition observed with calorimetry has to be related the protein hydration water (although involvement of protein degrees of freedom, as suggested in recent literature [**14, 69**], cannot be excluded).

3.3. Dielectric relaxation times

Dielectric spectra of myoglobin powders at h = 0.30 and at temperatures from 148 K to 233 K (every 5 K) are reported in Figure 31. At low temperatures a single weak and asymmetric relaxation is observed, that is called process "0". This process is very similar to that observed by other groups for lysozyme ("fast" or "main" process [**13, 70**]; process "1" [**71**]); it was not detected

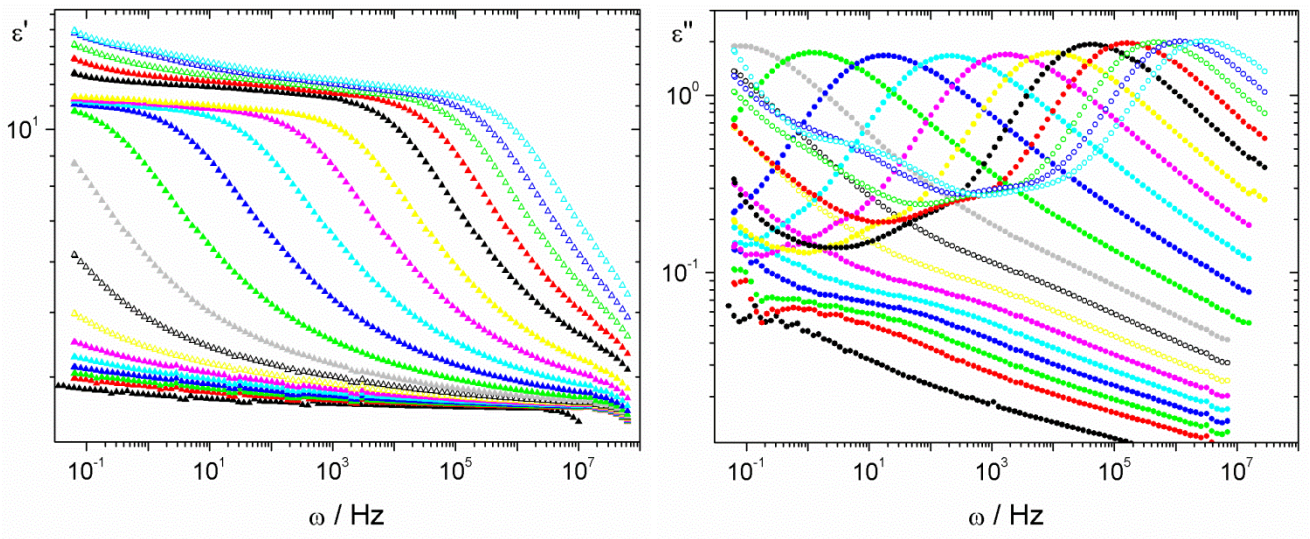

Figure 31. Real (*left panel*) and imaginary (*right panel*) parts of dielectric spectra of myoglobin powder at h = 0.30 and temperature range from 148 K to 233 K (every 5 K).

in a previous study by our group [**52**] due to lower sensitivity. As the temperature is increased a second, main, relaxation that is called process "I" steps in, followed by a third (process "II") relaxation; further lower frequency relaxations (like e.g. process "III") that enter in the frequency window at higher temperatures are neglected, in view of the uncertainties introduced by teflon coating. In Figure 32 a fit to the dielectric spectra (both real and imaginary parts were fitted simultaneously) in terms HN functions, as described in the Chapter 1, is represented.

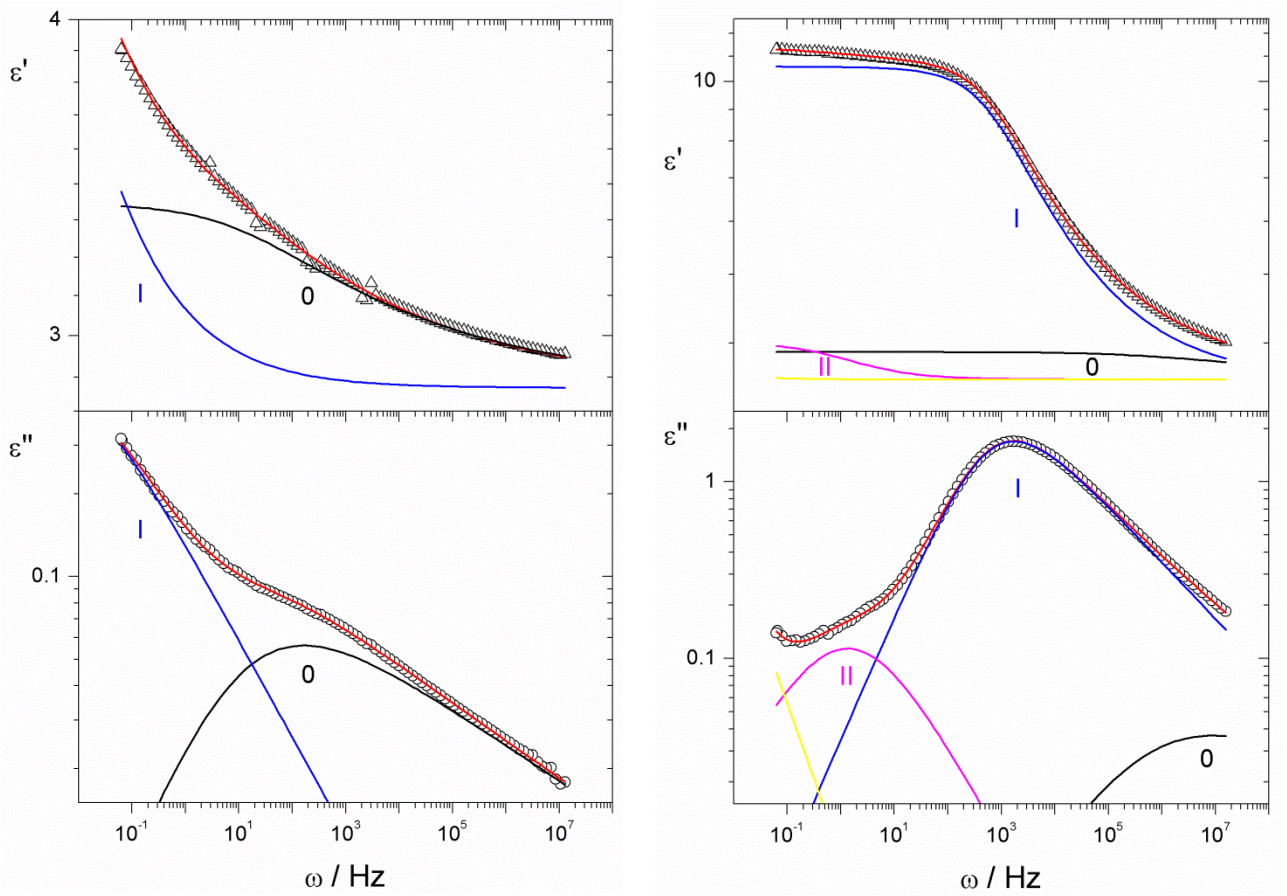

Figure 32. Typical fit to the dielectric spectra of Mb at h = 0.30 in terms of HN functions at T = 168 K (*left panel*) and at T = 203 K (*right panel*). Red lines are overall fittings while black, blue, magenta, and yellow lines represent the individual processes.

The analysis is fully compatible with that represented in ref. **52**. Fittings of comparable quality are obtained at all hydrations and temperatures. As mentioned in the Chapter 1, teflon coated cells were used. The use of teflon coating has been questioned in the literature, as it may introduce spurious peaks, especially at low frequencies and high temperatures [**72, 73**] and references therein. Therefore, to check the reliability of these results, an "ad hoc" experiment was performed whereby the same sample at h = 0.2 was measured in a teflon coated and in a gold coated cell. Results show that while with the teflon coated cell the relaxation peaks are clearly identified, with the gold coated cell they are almost completely obscured by a huge conductivity signal (except process 0 at low

temperatures); however, the fittings indicate that no alterations of peak positions are introduced by teflon coating.

The temperature dependence of relaxation times for processes 0, I, and II is depicted in Figure 33 in the usual log τ vs. 1000/T representation. Note that, when discussing dielectric data, one should keep in mind that all relaxing dipoles in the sample contribute to the observed signal; in the case of protein hydrated powders, both hydration water, polar protein side chains and backbone dipoles may contribute. Moreover, in view of the tight protein–hydration water coupling in used samples, separation of water and protein contributions may be often questionable.

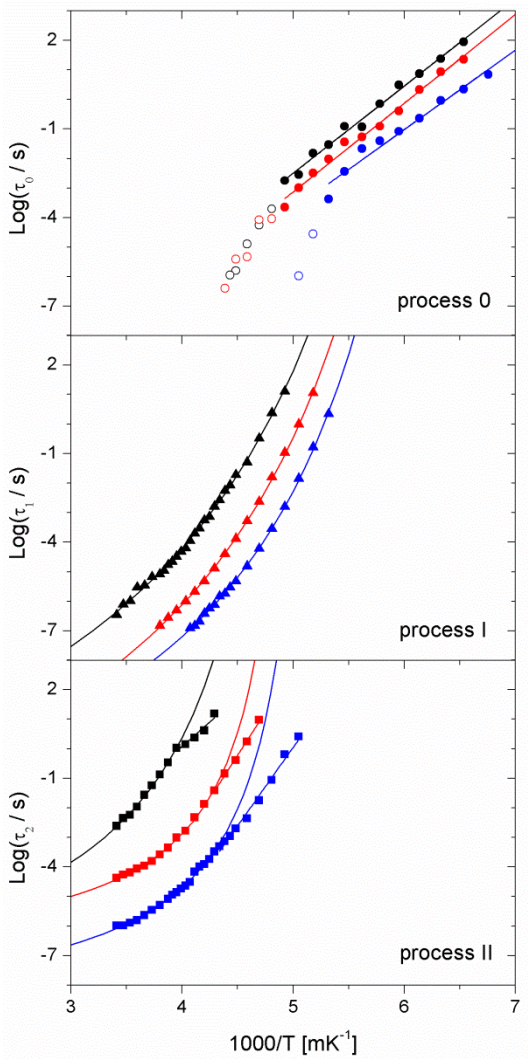

Figure 33. Logarithm of τ_0 (*upper panel*), τ_1 (*middle panel*), and τ_2 (*lower panel*) as a function of the inverse temperature. Black symbols: h = 0.1; red symbols: h = 0.2; blue symbols: h = 0.3. The continuous lines are fittings in terms of the VFT or Arrhenius laws.

Keeping in mind the above warnings, in agreement with previous studies [**13, 71**] process 0 is attributed as mainly arising from the fast rotational relaxation of D_2O molecules in the first

hydration shell; this is confirmed by the fact that its amplitude increases with increasing hydration (data not shown). The temperature dependence of the relaxation time of process 0, for lysozyme, has been analyzed as a simple Arrhenius behavior with activation energy (ΔH) of ~60 kJ/mol [**3, 13**] or as a more complex behavior, exhibiting a Vogel–Fulcher–Tamman (VFT)-Arrhenius crossover at ~180 K [**71**]. The data (upper panel of Figure 33) are compatible with this last behavior; however, process 0 is very weak and at high temperatures (> 200 K) it is partially obscured by the much larger process I: this may cause uncertainties in the exact determination of its temperature dependence at high T. In any case, a clear hydration dependence is observed and the slope of the Arrhenius behavior at low T gives an activation energy value of ~50 kJ/mol. The hydration dependence observed for process 0 is analogous to that observed in ref. [**13**] for the "main" relaxation of hydrated lysozyme powders; in view of the ENS data represented in Figure 29 (left panel), this fact does not support the suggestion in ref. [**3**] that the PDT is related to the characteristic time of this process entering the time window of the neutron spectrometer used.

The temperature dependence of the relaxation time of process I is depicted in Figure 33 (middle panel); at all hydrations it exhibits a VFT behavior, implying that a collective behavior of the protein + hydration water system observes. A collective process exhibiting a similar VFT behavior has also been observed for water confined in a disordered silica matrix [**28**]. For this process a marked hydration effect is observed: the curves shift to lower temperatures (higher $10^3/T$ values) as h increases. From the data, the values of T_{100} (i.e. the temperature values at which the relaxation time of process I reaches the value of 100 s (which is the standard definition of the "dielectric" glass transition) can be obtained; T_{100} values as a function of hydration are reported in Figure 30 (c), in comparison with the calorimetric glass transition onset temperatures. The close similarity between the two sets of data suggests that process I is in fact a collective relaxation of the system, involved in the glass transition. Concerning process II, its hydration dependence is similar to that for the process I; moreover, at all the hydrations investigated, it exhibits a VFT-Arrhenius crossover in the range 220 ÷ 230 K, i.e. in the same temperature region where the onset of the PDT is observed; the crossover temperature shifts to ~250 K for h = 0.1 likely in view of very small water content. Following refs. [**52**] and [**74, 75**] process II is attributed mainly to relaxations of protein side chains strongly coupled to the dynamics of hydration water.

3.4. Conclusions

The dynamics of myoglobin powder at different hydration levels (up to h = 0.5) has been investigated with three different techniques in the temperature range 120 ÷ 300 K. In order to make a conclusion about this study it is useful to correlate all obtained above results, presenting them on one graph (Figure 34). A thermodynamic description of Mb achieved by DSC is in Figure 34 (a); panels (b) and (c) report the relaxation times of myoglobin at two hydrations measured by BDS; the normalized ΔMSDs of non-exchangeable H atoms of hydrated myoglobin obtained by ENS are represented in panel (d).

The arrows in Figure 34 (b) and (c) graphically evidence that the characteristic time of the process I reaches 100 s at a temperature compatible with the glass transition onset temperature detected by DSC; that clearly links the process I to the viscosity-related relaxation of the hydration water. On the other hand, the crossover observed in the temperature dependence of the process II occurs at the same temperature of the LLT onset observed in the calorimetric scans. The normalized ΔMSDs of non-exchangeable H atoms of Mb show the typical kink in the MSD temperature dependence corresponding to the PDT. As evidenced by the pink area in Figure 34, the PDT occurs exactly in the same temperature region of the liquid-liquid thermodynamic/dynamic transition of hydration water.

The combined use of the different experimental techniques furnishes a coherent description of the PDT. Protein hydration water, after exhibiting a glass transition at about 170 K, experiences a first-order liquid-liquid transition at about 230 K, that we can identify with the LDL→HDL crossover observed in supercooled water, in analogy with what observed in other supercooled interfacial water systems [**76**]. This thermodynamic event has a dynamical counterpart in a change of cooperativity of the relevant water relaxation process, as revealed by dielectric measurements. As already shown [**77**], this change is related to a crossover from an almost fully tetrahedrally H-bonded, “strong” LDL to a “fragile” HDL, whose structure and dynamics are similar to that of supercooled bulk water at higher temperature. Water molecules involved in the crossover (i.e., interfacial water molecules) are tightly coupled with protein molecular groups on protein surface via hydrogen bonds and electrostatic interactions [**78**], and induce an increase of protein atomic fluctuations, which is revealed by neutron scattering as the PDT. This interpretation is also compatible with the absence of PDT in dry proteins, as experimentally proven.

The results presented here give further experimental evidence that a fundamental property of hydrated protein molecules is associated to a dynamical crossover in hydration water, which is supposed to be a general phenomenon occurring in supercooled water.

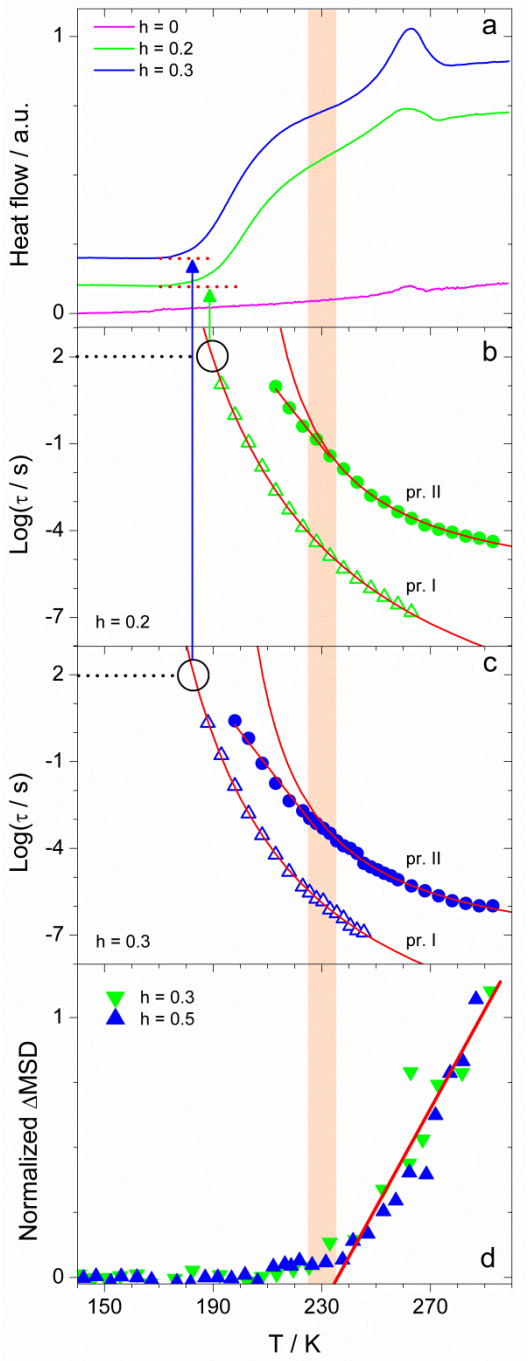

Figure 34. Experimental data obtained on D_2O-hydrated Mb powders. From top to bottom: (a) DSC up-scans; the accuracy of heat flow and temperature estimation is < ±1% and ± 0.1°C, respectively; (b) and (c) relaxation times obtained by BDS; error bars are not shown since they are of the order (or less) of the points dimension; (d) MSDs of non-exchangeable H atoms of Mb obtained by ENS. Pink area indicates the temperature region where hydration water shows a first-order liquid-liquid transition (a) and an Arrhenius-VFT crossover ((b) and (c)), while nonexchangeable H atoms of Mb undergo the PDT (d). The red line in (d) is a guide to the eye.

These results can be summarized as three key findings about the PDT:

- The PDT is not a mere resolution effect but reflects a real physical effect clearly related to the hydration water.
- Physical origin of the PDT: a structural transition in the hydration water.
- Possible connection with the LDL → HDL transition at about 230K.

In order to investigate protein hydration water for the presence of LLT that is expected to occur around 230 K, water was confined in disordered silica matrix. Latter permits to investigate supercooled region in more detailed way. Moreover, matrix's disordered structure is very similar to the protein surface. This study is presented and discussed in the following Chapter.

Chapter 4

Experimental evidence for a liquid-liquid crossover in deeply cooled confined water

In this chapter I will describe the experimental evidences obtained for the existence of a liquid-liquid transition in deeply cooled water confined within the pores of our silica xerogels. In paragraph 4.1 a thermodynamic description of our systems will be given by calorimetry, while in paragraph 4.2 I will focus on the so-called "pressure anomaly" of supercooled water studied with ENS at 210 and 250 K, i.e. below and above the putative LLT, respectively. The temperature dependence of the low frequency collective vibrational dynamics of our confined water will be investigated in paragraph 4.3 with INS, while the temperature dependence of QENS depicted in paragraph 4.4 will give information (although preliminary) essentially on the translational dynamics. Finally, information on the relaxational dynamics (essentially rotational) of electric dipoles in our samples will be obtained with BDS and represented in paragraph 4.5.

4.1. Thermodynamic description by calorimetry

Calorimetric measurements of the system have been obtained with DSC to characterize its thermodynamic state and to evidence the presence of calorimetric phase transitions. Samples were first cooled to 123 K with 5 K/min cooling rate. After equilibration at 123 K, calorimetric upscans from 123 to 303 K were performed with 20K/min heating rate. An empty sealed pan was used as a reference. The baseline was measured at the same scan rate with no pans in the furnace. Three samples at hydration levels 0.05, 0.19, and 0.42, were measured; the thermograms measured at h = 0.05 were used to subtract the matrix contribution.

The temperature dependence of the molar specific heat (C_P) is reported in the inset of Figure 35 (left panel); it compares very favourably with analogous data of Oguni et al., 2011 [**79**] on water conned in MCM-41-S. As clearly shown in the body of Figure 35 (left panel), the confined water exhibits a glass transition (step in C_P; peak in the derivative) at T~170 K, followed by a first order-like transition (maximum in C_P; positive-zero-negative sequence in the derivative) at T~230 K; no signs of crystallization (minimum in C_P; negative-zero-positive sequence in the derivative) are observed in between. These experiments suggest the following picture: at low temperature water confined within the pores of silica matrix is in a glassy state; around 170 K it undergoes

glass→liquid transition followed by a first order-like liquid→liquid transition at ~230 K. An analogous DSC experiment on the sample at h = 0.19 (Figure 35, right panel) evidenced the presence of a barely detectable broad glass transition at lower temperature with respect to h = 0.42 (in agreement with a decrease of glass transition temperature when water strongly interacts with pores walls [**80, 81**]), but no sign of the first order-like transition. DSC results provided the following essential information: 1) at ambient pressure water inside the xerogel is in a deeply cooled liquid state; 2) these temperatures correspond to liquid water below (210 K) and above (250 K) a liquid→liquid transition; 3) what is observed in the sample at h = 0.42 at ~230 K is a transition of the so-called "internal" water, not directly interacting with pore walls [**82**].

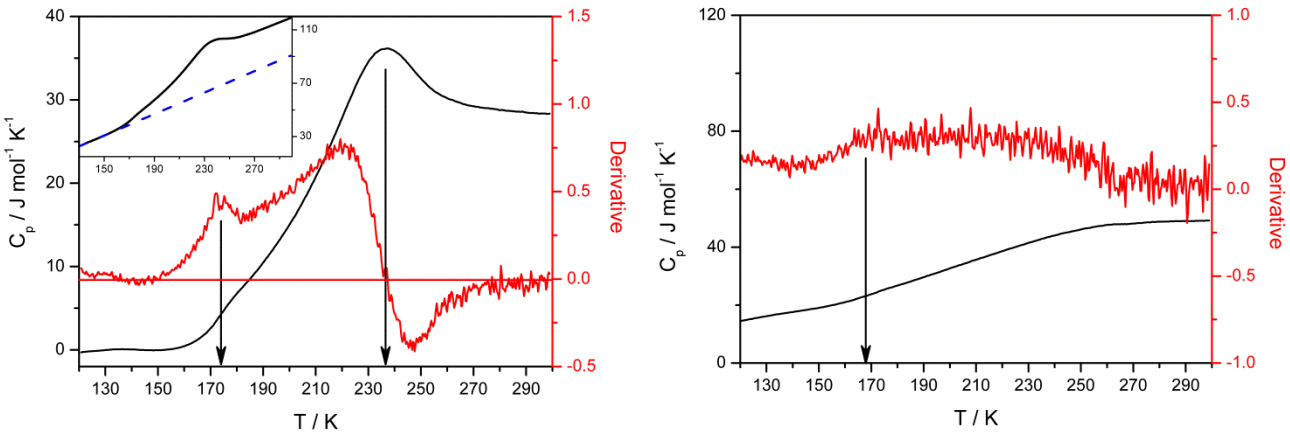

Figure 35. *Left panel*, *inset*: temperature dependence of molar specific heat (C_P) of water confined in a silica hydrogel at h = 0.42; the dashed line is a linear fit to the low temperature behavior. Main body: temperature dependence of C_P (black line) and its derivative (red line) after subtraction of the linear extrapolation. The vertical lines indicate the midpoint temperatures of the glass transition and of the specific heat maximum (Liquid-Liquid Transition). Note the close similarity of the C_P data with the calculations of ref. [**79**]. *Right panel*: temperature dependence of the molar specific heat (C_P) of water confined in a silica hydrogel at h = 0.19 (black line) and its derivative (red line). The vertical line indicates the presence of a broad glass transition. Heat flow error was 0.05 mW.

4.2. Dynamic counterpart by ENS: pressure dependence of MSD

Let's focus on the so-called "pressure anomaly", i.e. on the anomalous increase of the isothermal diffusion coefficients observed for liquid water at low temperatures (below ~300 K) and getting more and more evident in the supercooled region. The commonly accepted, qualitative explanation of the anomalous pressure effect is that pressure disrupts the tetrahedral hydrogen bonds network with a consequent increase of molecular mobility; in contrast, compression of a "normal" liquid leads to a progressive loss of mobility as the molecules are brought closer to each other [**83**]. The pressure dependence of translational and rotational diffusion coefficients of bulk water has been shown in refs. [**83-86**]. Results are expressed as the pressure dependence of the ratio $R(P) = X(P)/X(P_{atm})$, where X stands for the measured transport property.

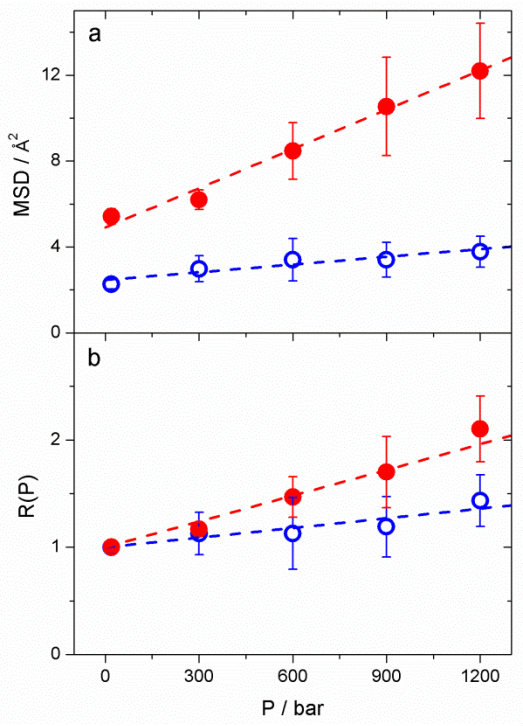

Figure 36. MSD (a) and R(P) = MSD(P) / MSD(P = 20 bar) (b) as a function of pressure. Black open circles: T = 210 K; red circles: T = 250 K. Dashed lines are linear fits.

Water behaves as a normal liquid (i.e. R decreases with pressure) at temperature above the melting point, while the anomalous behavior (i.e. R increases with pressure) is present already at 273 K and gets strongly enhanced when water is supercooled to 243 K where R(P = 1 kbar) is between 1.6 and 2. The pressure effect on translational diffusion is smaller than that on rotational diffusion and exhibits a maximum located at about 1.5-2.0 kbar for translation and about 2.5-3.0 kbar for rotation. Simulation studies on the pressure dependence of the water translational diffusion coefficient using the SPC/E potential have also been performed [**87, 88**] down to 210 K. Simulations qualitatively

reproduce the experimental data; it is very interesting to note that the pressure effect at 210 K is predicted to be much larger than at 240 K.

Here the identical samples to that used for DSC measurements were used. The central result of ENS experiment is represented in Figure 36, where we report the MSD (panel a) and the quantity R(P) = MSD(P) / MSD(P = 20 bar) (panel b) as a function of pressure in the range 20 ÷ 1200 bar at T = 210 and 250 K. More detailed data, i.e. normalized values of ln[I(Q, E = 0)] vs. Q^2 at the two temperatures investigated, are represented in [**80**]. Results in Figure 36 immediately reveal that the water hydrogen's MSD increase with pressure, i.e. the water pressure anomaly is observed in our sample, both at 250 and at 210 K. However, the pressure effect is larger at 250 K than at 210 K. The values of dR(P)/dP obtained from the linear fits represented in Figure 36 are 1.8 and 1.25 $kbar^{-1}$ at 250 and 210 K, respectively. Unfortunately, the pressure range investigated does not allow to put in evidence the possible presence and location of R(P) maxima. We also note that from the MSD measured at 20 bar and, using the Eq. 38, one obtains D (250 K, 20 bar) = $1 \cdot 10^{-6}$ $cm^2 s^{-1}$ and D (210 K, 20 bar) = $0.3 \cdot 10^{-6}$ $cm^2 s^{-1}$. These values compare favorably with D values shown in the literature from quasi-elastic neutron scattering experiments or from simulations [**88-91**]. ENS results in Figure 36 provide the dynamic counterpart of the thermodynamic description obtained by DSC (Figure 35). First, the observation of an "anomalous" pressure effect on the MSD (together with the absence of Bragg diffraction from ice in the structure factor I(Q)) confirms that in our sample water confined within the pores of the silica matrix is a liquid both at 250 and 210 K. Moreover, the behavior at 210 K is surprising: instead of an increased anomalous pressure effect, expected for a liquid approaching a critical divergence and indeed obtained for simulated SPC/E water [**87, 88**], we measure a much lower effect. The glass transition/fragility scenario seems also unable to explain the reported effects. In fact, the "ideal" glass transition temperature (T_0) of water has been shown to increase slightly with pressure, of about 5 K for a pressure increase of 1.5 kbar [**84, 92**]; this, in turn, would cause a (rather small) increase of the quantity T_0/T and therefore a viscosity increase, contrary to what observed. Therefore, our data indicate that, going from 250 K to 210 K, water confined in the silica xerogel undergoes a crossover in which the hydrogen bonds network becomes stronger and less deformable by pressure. This idea is then compatible with the existence of two different phases of water at 250 and 210 K, i.e. with the LLT hypothesis. The pressure dependence of MSD is also compatible with the fragile-to-strong dynamic crossover in the water relaxation times observed by neutron scattering [**15**], nuclear magnetic resonance [**16**] and dielectric spectroscopy [**53**] in the same temperature region of the LLT. Indeed, relaxation times of fragile systems are more affected by pressure than those of strong systems. Supercooled water, in particular, shows a one order of magnitude reduction of translational relaxation times in the fragile

regime when pressure is increased up to 1.4 kbar, while the pressure effect is much weaker in the strong regime [**15, 93**].

4.3. Temperature dependence of Boson peak by INS

One of the characteristic features of supercooled water, analogously to glasses and amorphous materials, is the presence of low-frequency modes revealed by inelastic neutron scattering, x-ray scattering and Raman scattering in the energy range 2-10 meV (the so-called Boson peak), where the vibrational density of states g(E) shows an excess over the $g(E) \sim E^2$ law predicted by the Debye model. Many hypotheses have been proposed to explain the physical mechanisms giving rise to the Boson peak, but a comprehensive understanding has proved elusive. In a recent MD study [**40**], Stanley and collaborators investigated the origin of the Boson peak in TIP4P/2005 water and found that its onset in supercooled bulk water when temperature is lowered below 225 K coincides with the crossover to a predominantly low-density-like liquid. This behavior was found to be in agreement with some older preliminary experimental data on deeply cooled nanoconfined water [**93, 94**] and with more recent data and analysis by the same group [**41**].

Here, we explored the temperature dependence of the boson peak of supercooled water in order to search for a possible experimental evidence of the LLPT hypothesis. We used inelastic neutron scattering to measure the water spectrum in the Boson peak region in the temperature range $100 \div 280$ K.

Typical spectra are depicted in Figure 37. A vibrational excess centered at about 5 meV (BP) is clearly visible in the low temperature spectra where it emerges as a peak over the other contributions; at temperatures higher than about 235 K the quasi elastic contribution grows in amplitude and width and almost smears out the boson peak that, at $T \sim 280$ K, remains only as a barely visible shoulder. At low temperatures the boson peak is more evident in the $h = 0.42$ sample and this fact, together with its absence in the matrix spectra, indicates that it must be attributed to the water confined within the pores of the silica matrix. To obtain quantitative information on the temperature dependence of the BP we analyzed the data in terms of Eq. (40). Typical fits are represented in Figure 38 (left panel); fits of analogous quality are obtained at all the temperatures investigated. As mentioned in Sec. 1.3.2.3, from the lognormal distribution taking into account the inelastic contribution we obtain the VDOS (see Eqs. (41) and (42)); further division by E^2 to enhance the excess contribution over the Debye level yields the R-VDOS that is represented, at

selected temperatures, in Figure 38 (right panel). Some relevant features are already evident from visual inspection. In fact, R-VDOS redshifts and widens by increasing the temperature, the effect being similar for the two hydrations; conversely, the intensities behave in a different way: while for the sample at h = 0.19 they increase monotonically with temperature, for the sample at h = 0.42 an inversion is observed at about 225 K.

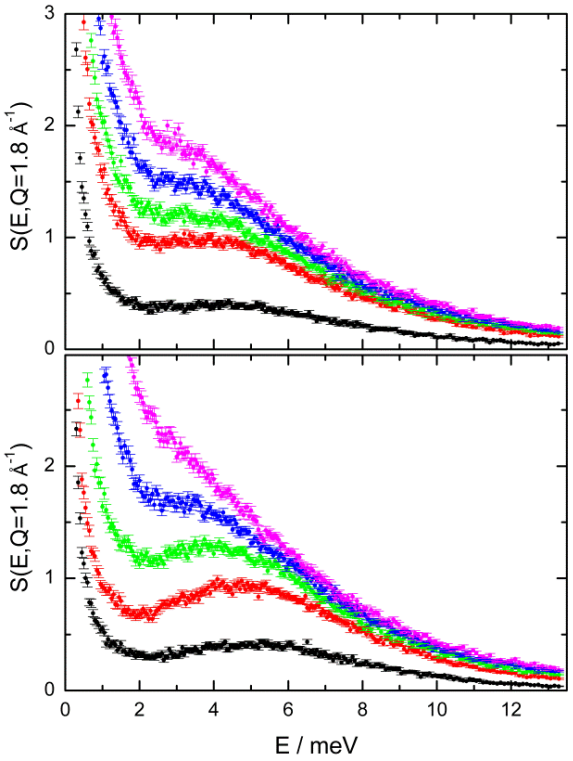

Figure 37. *Upper panel*: Dynamic structure factor of silica xerogel at h = 0.19; from bottom to top: T = 105 K (black), T = 195 K (red), T = 215 K (green), T = 238 K (blue), and T = 255 K (magenta). *Lower panel*: Dynamic structure factor of silica xerogel at h = 0.42; from bottom to top: T = 100 K (black), T = 187 K (red), T = 215 K (green), T = 235 K (blue), and T = 257 K (magenta).

More detailed information is obtained by calculating the R-VDOS zeroth, first, and second moments, following Eqs. (43), (44), and (45); results are shown in Figure 39 (left panel). Concerning the zeroth moment, the different hydration dependent behavior is striking: for the h = 0.42 sample a clear inversion is observed at 225 K so that at higher temperatures the BP area tends to vanish, while for the h = 0.19 sample a monotonous increase is observed. Concerning the position (M_1) and width (M_2) of the boson peak, no hydration effect is observed. Qualitatively, a BP redshift with temperature may be attributed to the effect of anharmonicity, while a BP widening may be attributed to the effect of mode damping. We note that redshift and widening of the R-VDOS with increasing temperature has been observed in the simulations of TIP4P/2005 supercooled water by Kumar et al. [**40**], and that our low temperature M_1 value of ~6 meV

(~50 cm^{-1}) is in very good agreement with their calculated value. We note also that around 225 K we observe a smooth temperature dependence of M_1 and M_2, in agreement with the results of a very recent study on the pressure and temperature dependence of the BP in deeply cooled water confined in MCM-41-S [**41**]. In that study, the authors state that the BP "emerges" if a maximum in the S(E, Q = 1.8 $Å^{-1}$) curve is observed between 2 and 10 meV; otherwise, the BP has "disappeared." With this semi-quantitative definition they obtain, in the temperature-pressure plane, an "emergence line" of the BP that, below 1600 bars, is parallel (although not coincident) with the so-called Widom line, defined as the line in the water phase diagram formed by the points of maxima of thermodynamic response functions; this behavior is taken as further evidence for a liquid-liquid crossover in deeply cooled confined water. It is important to stress that our data on normalized M_0 are in full agreement with this view since they highlight the presence of an inversion point at about 225 K, i.e., the temperature where a fragile-to-strong crossover is observed in the temperature dependence of relaxation times of nano-confined water [**15**] and in the protein hydration water [**7**].

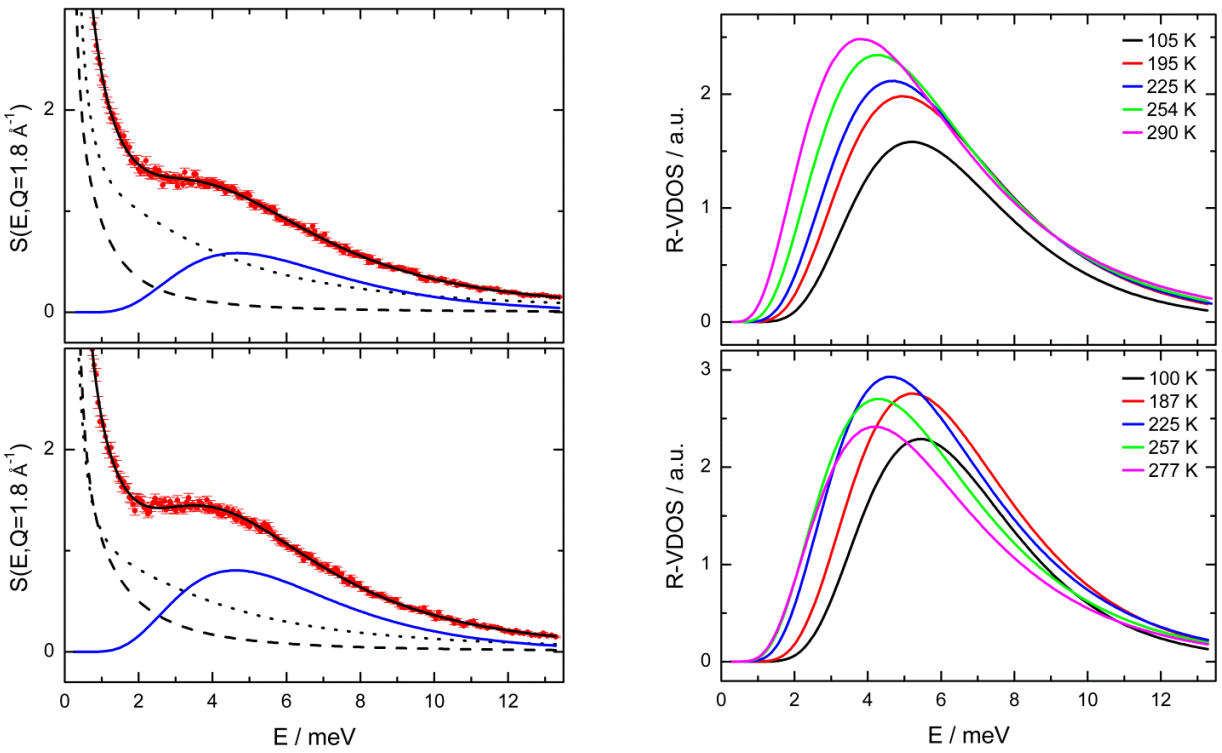

Figure 38. *Left panel*: Fit to the inelastic spectra at T = 225 K for samples at h = 0.19 (*upper*) and h = 0.42 (*lower*). Red circles: experimental data; dotted line: matrix contribution; dashed line: quasi-elastic contribution; and continuous blue line: log-normal distribution representing the boson peak. The total fit is also depicted as a continuous line superimposed to the experimental data. *Right panel*: R-VDOS as a function of energy at selected temperatures; h = 0.19 (*upper*) and h = 0.42 (*lower*).

To check the validity of our BP results, the temperature dependence of the quasi-elastic contribution has to be investigated. Amplitudes and Half Widths at Half Maximum (HWHM) of the

quasi-elastic contribution (sum of the L_1 and L_2 terms in Eq. (40)) are reported in Figure 38 (right panel) as a function of temperature. As expected, an amplitude increase with temperature is observed; however, no hydration dependence is present, indicating that the M_0 inversion observed for the BP at h = 0.42 is not due to an anomalous increase of the quasi-elastic contribution but is a real property of the BP. Concerning the HWHM, we note that it is much smaller for the h = 0.19 sample, in agreement with the fact that water strongly interacting with pore walls moves on a lower time scale than internal water; moreover, its increase with temperature is barely visible in the ordinate scale of Figure 39 (right panel). Concerning the h = 0.42 sample, the larger HWHM has to be attributed to internal water and its marked increase with temperature is expected; considering the rather large error bars, we prefer not to speculate about the possible presence of an inflection at about 225 K.

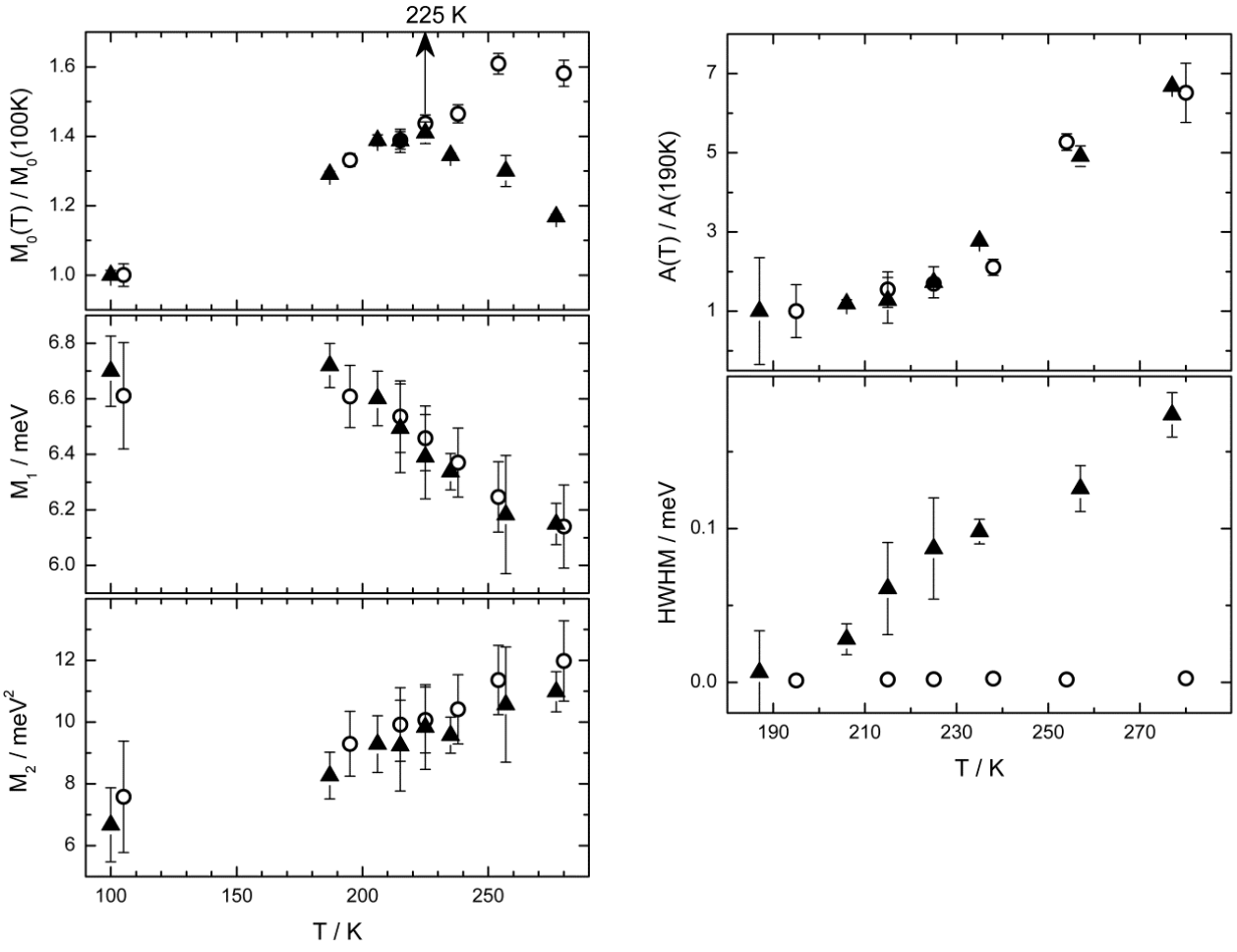

Figure 39. *Left panel*: Moments of the R-VDOS as a function of temperature at h = 0.19 (open circles) and h = 0.42 (full triangles). (*Upper*) Zero moments normalized to their low temperature values in order to take into account different sample composition and weight, (*middle*) first moment, and (*lower*) second moment. *Right panel*: Temperature dependence of the quasi-elastic contribution for h = 0.19 (open circles) and h = 0.42 (full triangles). (*Upper*) Normalized amplitude and (*lower*) half width.

4.4. The fragile-to-strong hypothesis checked by QENS

By using the high energy resolution neutron backscattering spectrometer SPHERES we obtained QENS spectra of water confined in silica matrix for temperature set from 20 to 300 K. The experimental data normalized on T = 20 K for the samples at h = 0.42, 0.19, and 0.05 (matrix contribution) are depicted in Figure 40. Before data analysis it is possible to have some idea about a key obtained result by comparing the experimental spectra of the sample at two hydrations. The broadening of the spectra at the wings due to the quasi-elastic contribution becomes more and more noticeable as temperature increases. But for h = 0.19 this behavior is gradual, while for h = 0.42 there is an evident spectra shape change after reaching T = 230 K. At the same time, the elastic peak intensity decreases with increasing of temperature.

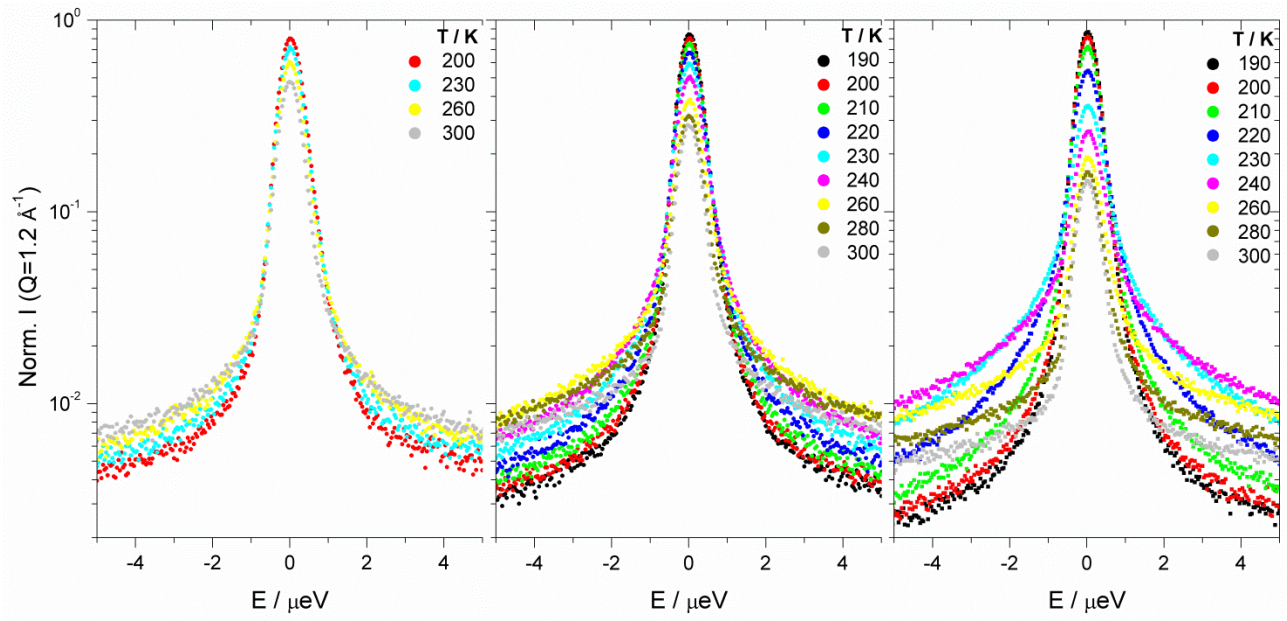

Figure 40. Normalized (on T = 20 K) QENS spectra I(E, Q = 1.2 Å^{-1}) were obtained by binning all the measured spectra in the interval 0.6 < Q < 1.8 Å^{-1} for h = 0.05 (*left panel*), h = 0.19 (*middle panel*), and h = 0.42 (*right panel*).

In Figure 41 we plot the normalized elastic peak intensity as a function of temperature for investigated sample hydrations. It is noticeable that for the higher hydration sample the curve slope is different across the temperature zone of 220 ÷ 240 K. To evidentiate this effect we have calculated the derivatives of the intensity vs. temperature curves (lower panel of Figure 41). The data relative to h = 0.42 exhibit a deep minimum at about 220 K; this minimum is less pronounced and shifted to ~230 K for the sample at h = 0.19, and absent for the dry sample.

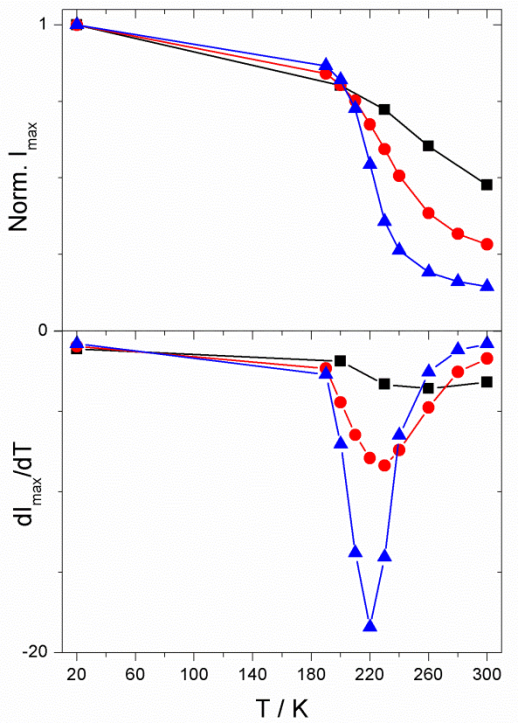

Figure 41. Normalized elastic intensity (*upper panel*) of QENS spectra (data binning in Q from 0.6 to 1.8 $Å^{-1}$) and its derivative (*lower panel*) vs. temperature for different hydration level of silica matrix: h = 0.05 (black squares), h = 0.19 (red circles), and h = 0.42 (blue triangles).

For a more detailed analysis the QENS spectra have been fitted with the simplified Eq. 39. In Figure 42 (left panel) we present a typical fit to the QENS spectrum at h = 0.42 and T = 240 K by this function. We are aware of the fact that this analysis is over-simplified. As a matter of fact, the analysis of QENS spectra of deeply cooled confined water is a highly debated issue and no clear consensus has been reached yet. In particular, a model consisting of an elastic line and a Kohlrausch-Williams-Watts function (KWW, Fourier transform of a stretched exponential) has been used by Chen and coworkers [**7**], but the results have been highly questioned [**26**]. Here, we use the above over-simplified analysis simply to check the consistency of our QENS data with the fragile-to-strong crossover hypothesis. Our group is actually working on the development of a more detailed analysis of QENS spectra that involves a "Q-by-Q" spectral analysis (not simply the analysis of data binned over on extended Q range). The results of this analysis are for beyond the aims of this thesis and will be published elsewhere.

In Figure 42 (right panel) we then present an Arrhenius plot, the temperature dependence of the average translational relaxation time for the hydrogen atom in a water molecule calculated by the following equation:

$$\tau(\mathrm{s}) = \frac{h}{w_2 \cdot 10^{-6}} \tag{48}$$

where $h = 4.14 \cdot 10^{-15}$ (eV·s) is Planck's constant.

It is seen that for higher hydration sample, h = 0.42, in the temperature range 300 ÷ 220 K, log(τ) obeys VFT law, a signature of fragile liquid, but at T = 220 K it suddenly switches to an Arrhenius law, a signature of a strong liquid. Therefore, our QENS data are fully compatible with the Fragile-to-Strong Crossover hypothesis. For the lower hydration, h = 0.19, and also for our almost dry sample, h = 0.05, the temperature dependence of translational relaxation time expectedly shows a simple Arrhenius behavior.

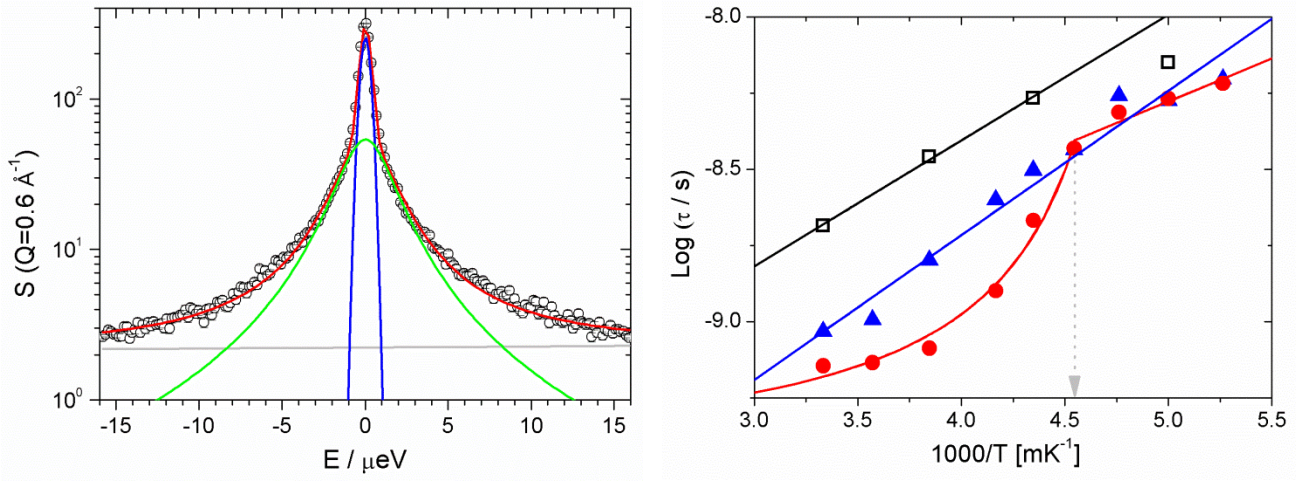

Figure 42. *Left panel*: measured QENS spectrum of silica hydrogel at h = 0.42 and T = 240 K (binning is done for every four data points in E). Fitting curves: total (red), elastic contribution (blue), QENS contribution (green), and background (grey). *Right panel*: logarithm of τ as a function of the inverse temperature for h = 0.05 (black open squares), h = 0.19 (blue triangles), and h = 0.42 (red circles).

4.5. Evidence for fragile-to-strong crossover by dielectric spectroscopy

Dielectric spectra of silica xerogels at different hydration levels, h = 0.42, 0.19, 0.05, and ~0, are obtained over temperature range from 123 to 300 K. All spectra have been fitted by HN-equation; for three hydration level dielectric loss spectrum with fitting curves at one representative temperature is depicted in Figure 43. As it was shown afore, there are four relaxation processes in hydrated myoglobin and these processes appear consecutively in our accessible frequency range due

to temperature increase. Such processes exist also in silica hydrogels. Instead of enough weak protein relaxation process at low temperatures the well-defined process 0 is observed for both hydrated and dry silica powders. In case of Mb, we have attributed this process to a fast rotational relaxation of water molecules in the first hydration shell. Being bounded with the protein surface and dependent on side groups of protein chain, water molecules exhibit a weak relaxation process of not very clear shape. On the contrary, being in the pores of silica matrix the water molecules are relatively free and the lower temperature process 0 is clearly marked, almost symmetric and is not under influence of the following process I. As has been mentioned, in our dry sample, h ~ 0, the process 0 is also observed, that can be explained either due to OH groups, which are present in case of not completely polymerized silica matrix, or some residual water molecules, which are almost impossible to remove completely from the pores of solid matrix.

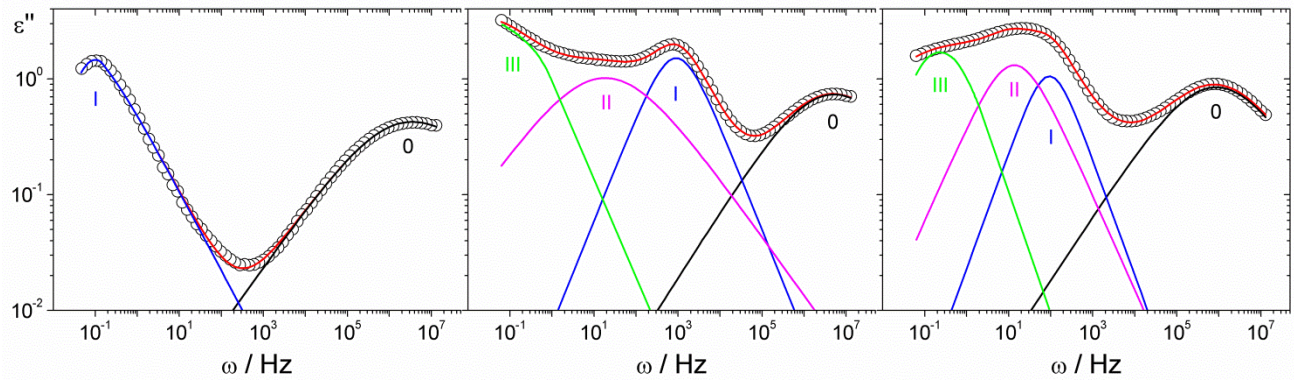

Figure 43. Typical HN fit to the dielectric losses in silica hydrogel at h ~ 0 (*left panel*) and h = 0.19 (*middle panel*) at T = 203 K, and h = 0.42 (*right panel*) at T = 193 K. Red lines are overall fittings while lines of another colors represent the individual processes.

As usual the temperature dependence of relaxation times, log τ vs. 1000/T, of observed relaxation processes is depicted in Figure 44 in series for three hydration levels. The temperature dependence of the relaxation time of process 0 is the same for all samples, i.e. shows independence on water amount (overlapping at superposition), and has a simple Arrhenius behavior with activation energy of ~50 kJ/mol. Our protein data (see upper panel of Figure 33) are well compatible with this behavior; just the relaxation time of process 0 for confined water is faster (~ two orders of magnitude), than that for the protein, that supports the above given explanation of water molecules rotation. Also the process I of dry sample has a linear temperature dependence.

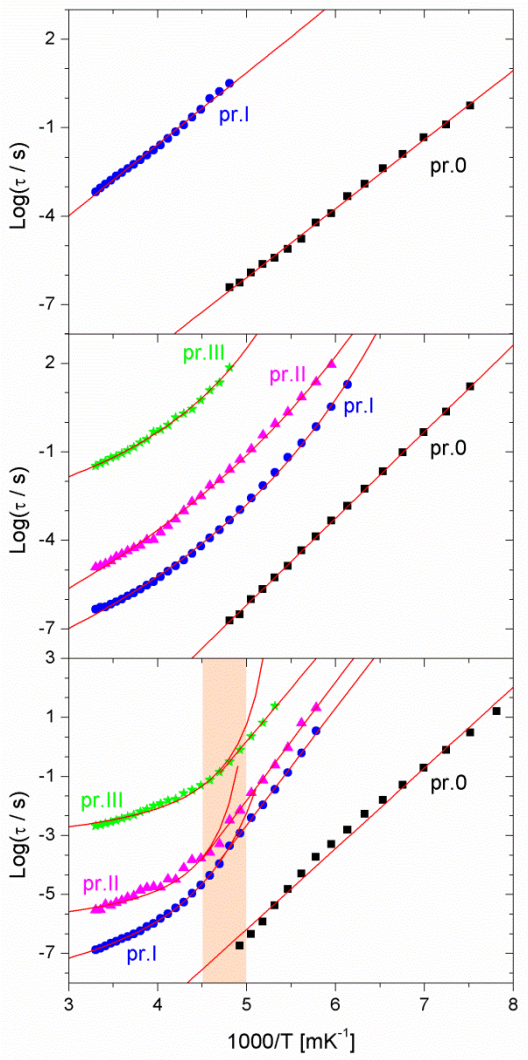

Figure 44. Logarithm of τ as a function of the inverse temperature for h ~ 0 (*upper panel*), h = 0.19 (*middle panel*), and h = 0.42 (*lower panel*). Process 0 (black squares), process I (red circles, process II (blue triangles), and process III (green triangles down). The continuous lines are fittings in terms of the VFT or Arrhenius laws. Pink zone in bottom panel highlights the temperature interval in which, for process I and II, a VFT–Arrhenius crossover is observed.

At the hydration h = 0.19 the temperature dependence of the relaxation times of processes I, II, and III, reported in Figure 44 (middle panel), exhibits a VFT behavior, while at the higher hydration, h = 0.42, all these processes exhibit a VFT-Arrhenius crossover in the range 200 ÷ 220 K (evidenced by the pink zone in Figure 44, lower panel), i.e. in the same temperature region of the LLT. This is a key result obtained by BDS on H_2O embedded in the pores of silica matrix, since it reveals the change in water behavior from “strong” to “fragile” giving experimental support for the liquid-liquid transition. It should be noted that it has been possible to register this crossover only in case of sufficient water amount in the pores of the matrix, so-called "internal" water.

4.6. Conclusions

Our data give a new experimental evidence of the existence of LLT occurring at ~230 K in deeply cooled confined water obtained by DSC, ENS, INS, QENS, and BDS techniques.

1. the pressure-dependent ENS data shows that at 210 K water is in a liquid state, as shown by the fact that it exhibits an anomalous pressure effect (increasing MSD as pressure is increased) and it is also confirmed by the thermodynamic transitions probed by DSC; however, the comparatively small pressure effect indicates the presence of an almost fully developed, locally icelike, hydrogen bond network less deformable by pressure and suggests that water is essentially in the LDL state (Figure 45, left panel). By increasing the temperature, a first-order-like liquid-liquid calorimetric transition is observed at ~230 K so that at 250 K water is essentially in the HDL state in which the local, tetrahedrally coordinated, hydrogen bond network is not fully developed and is therefore more deformable by a pressure increase. Therefore, our data give experimental support to the LLT hypothesis. The results for both studies are presented in a sketch below (Figure 45, right panel).

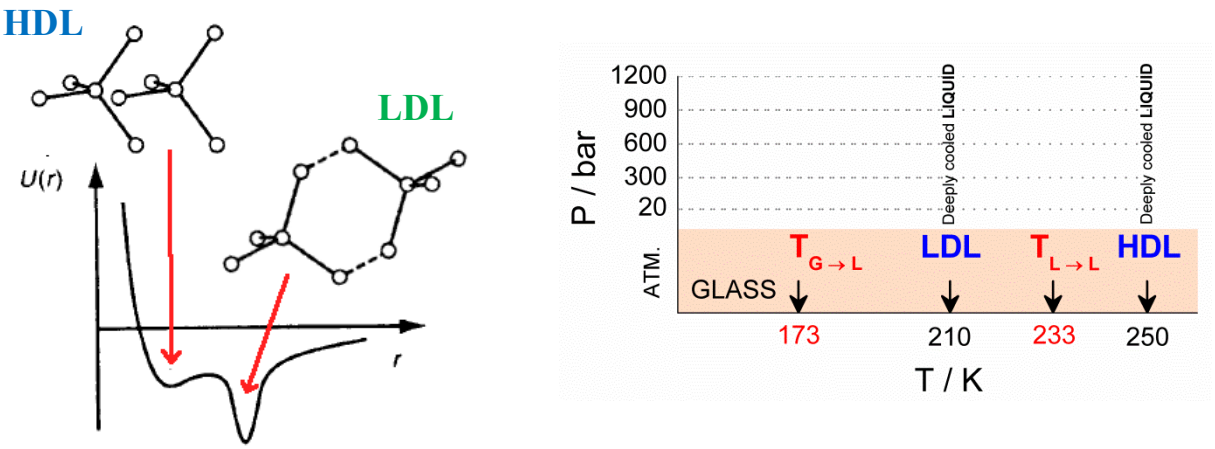

Figure 45. *Left panel*: two-wells water interaction potential with corresponding idealized interaction clusters of water molecules in configurations [**95**]. *Right panel*: a summary of the results on deeply cooled confined water obtained by DSC and ENS techniques.

2. investigation of the behavior of low-frequency modes of water (Boson peak) by using different hydration levels allowed us to exactly identify the contribution of internal water to neutron inelastic spectra and to reveal a clear inflection point in the Boson peak intensity at 225 K, the presence of that point we attribute to the proposed liquid-liquid transition.

3. the temperature dependence of translational (studied by QENS) and rotational (studied by BDS) relaxation times of internal water confined in silica matrix detects the presence of a fragile to strong crossover at T ~ 230 K that also confirms the LLT hypothesis.

Chapter 5

Conclusions and perspectives

In this work we focused on the study of hydrated myoglobin in order to determine the physical nature of the protein dynamical transition which was found by elastic neutron scattering at the temperature ~230 K. Experimental investigations were made by using three powerful methods, such as neutron scattering, differential scanning calorimetry, and broadband dielectric spectroscopy. The main results relative to myoglobin can be summarized as follows:

1. ENS data analysis shows that the PDT depends only on the presence of water on protein surface (no PDT in dry protein); moreover, while the amplitude of anharmonic fluctuations is found to depend on hydration, the onset temperature of the PDT is independent on protein hydration.

2. the study of homomeric polypeptides on neutron spectrometers of different energy resolution proves that the PDT is not a mere resolution effect.

3. calorimetric study of hydrated protein shows that after the glass transition, there is another transition, likely a liquid-liquid transition (LLT) which is associated with the protein hydration water.

4. broadband dielectric study of hydrated protein detects the presence of a fragile to strong crossover in relaxation process which is attributed to the relaxation of protein side chains strongly coupled to the dynamics of hydration water.

Thus, the study of hydrated protein suggests a dependence of PDT on hydration water, which is supposed to undergo a structural transition from LDL to HDL at T ~ 230 K or LLT. Thus, the LLT triggers the PDT, i.e. is its physical origin. With the aim of obtaining further experimental evidence of the existence of a LLT in deeply cooled confined water, a simple experimental model was used, namely silica matrix, in the pores of which water was embedded. Such system allows studying water in a deeply cooled state, excluding its crystallization, and well mimics protein surface due to its disordered structure, while water in its pores is like protein hydration water. We have obtained a thermodynamic description of this system with Differential Scanning Calorimetry and we have investigated the dynamic properties of confined water by exploiting the pressure dependence of Mean Square Displacements and the temperature dependence of the Boson Peak and of the Quasi-Elastic contribution. All the data consistently pointed out the presence of a liquid-liquid crossover

occurring at about 220 ÷ 230 K, i.e. at the same temperature where the onset of the PDT is observed in hydrated protein powders.

On the basis of the reported experimental evidence, I therefore think that the provisional answer to the question mark in the title of the thesis may be:

YES; THE PHYSICAL ORIGIN OF THE PROTEIN DYNAMICAL TRANSITION IS A LIQUID-LIQUID CROSSOVER IN THE STRUCTURAL/DYNAMICAL PROPERTIES OF PROTEIN HYDRATION WATER.

I am aware of the main objection that can be raised against the above conclusion: you did not provide direct evidence of your final statement, since you investigated a plausible model system (water confined in a disordered hydrophilic silica matrix) but not the protein hydration water in a hydrated protein powder.

Studying protein powders hydrated with H_2O and trying to separate hydration water contributions from protein contributions is a tricky procedure (as the dielectric data presented in this thesis clearly show) and may lead to questionable conclusions. As a matter of fact, a direct proof of the above statement would be a neutron scattering study of a H_2O-hydrated perdeuterated protein. Then, since neutron scattering gives information on the hydrogen atoms, the obtained data will pertain only to the hydration shell of the protein, since all (including non-exchangeable) protein hydrogens will be replaced by deuterium. Unfortunately, although the production of perdeuterated proteins is possible at the ILL Deuteration Laboratory, the procedure is long, not always easy and always expensive. However, such an experiment is in our perspective and will be a final step in the investigation of the scientific problem of this thesis.

Bibliography

[1] H. Frauenfelder, F. Parak, R.D. Young, Annu.Rev. Biophys. Biophys. Chem. 17, 451–479 (1988)

[2] W. Doster, S. Cusack, W. Petry, Nature 337, 754–756 (1989)

[3] S. Khodadadi, S. Pawlus, J.H. Roh, V. Garcia Sakai, E. Mamontov, A.P. Sokolov, J. Chem. Phys. 128, 195106 (2008)

[4] G. Chen, P.W. Fenimore, H. Frauenfelder, F. Mezei, J. Swenson, R.D. Young, Philos. Mag. 88, 3877–3883 (2008)

[5] S. Magazù, F.Migliardo, A. Benedetto, J. Phys. Chem. B 115, 7736–7743 (2011)

[6] G. Zaccai, Science 288, 1604–1607 (2000)

[7] S.-H. Chen, L. Liu, E. Fratini, P. Baglioni, A. Faraone, E. Mamontov, Proc. Natl. Acad. Sci. 103, 9012–9016 (2006)

[8] G. Schirò, F. Natali, A. Cupane, Phys. Rev. Lett. 109, 128102–128106 (2012)

[9] G. Schirò, Biophys. Chem. 180–181, 29–36 (2013)

[10] K. L. Ngai, S. Capaccioli, A. Paciaroni, J. Chem. Phys. 138, 235102–235115 (2013)

[11] W. Doster, J. Non-Cryst. Solids 357, 622–628 (2011)

[12] A. M. Klibanov, Nature 409, 241–246 (2001)

[13] S. Khodadadi, S. Pawlus, A.P. Sokolov, J. Phys. Chem. B 112, 14273–14280 (2008)

[14] H. Jansson, R. Bergman, J. Swenson, J. Phys. Chem. B 115, 4099–4109 (2011)

[15] L. Liu, S.-H. Chen, A. Faraone, C.-W. Yen, C.-Y. Mou, Phys. Rev. Lett. 95, 117802 (2005)

[16] S.-H. Chen, F. Mallamace, C. Y. Mou, M. Broccio, C. Corsaro, A. Faraone, L. Liu, Proc. Natl. Acad. Sci. U.S.A. 103, 12974 (2006)

[17] F. Mallamace, M. Broccio, C. Corsaro, A. Faraone, U.Wanderlingh, L. Liu, C. Y. Mou, S.-H. Chen, J. Chem. Phys. 124, 161102 (2006)

[18] Y. Liu, A. Z. Panagiotopoulos, P. G. Debenedetti, J. Chem. Phys. 131, 104508 (2009)

[19] P. Gallo, M. Rovere, S.-H. Chen, J. Phys. Chem. Lett. 1, 729 (2010)

[20] N. Giovambattista, T. Loerting, B. R. Lukanov, F. W. Starr, Sci. Rep. 2, 390 (2012)

[21] D. T. Limmer, D. Chandler, J. Chem. Phys. 135, 134503 (2011)

[22] D. T. Limmer, D. Chandler, J. Chem. Phys. 138, 214504 (2013)

[23] M. G. Mazza, K. Stokely, S. E. Pagnotta, F. Bruni, H. E. Stanley, G. Franzese, Proc. Natl. Acad. Sci. U.S.A. 108, 19873 (2011)

[24] S. Pawlus, S. Khodadadi, A. P. Sokolov, Phys. Rev. Lett. 100, 108103 (2008)

[25] M. Vogel, Phys. Rev. Lett. 101, 225701 (2008)

[26] W. Doster, S. Busch, A. M. Gaspar, M.-S. Appavou, J. Wuttke, H. Scheer, Phys. Rev. Lett. 104, 098101 (2010)

[27] A. Cupane, M. Levantino, M. G. Santangelo, J. Phys. Chem. B 106, 11323 (2002)

[28] M. Cammarata, M. Levantino, A. Cupane, A. Longo, A. Martorana, and F. Bruni, Eur. Phys. J. E 12, S63 (2003)

[29] M. G. Santangelo, M. Levantino, A. Cupane, G. Jeschke, J. Phys. Chem. B 112, 15546 (2008)

[30] Y. Zhang, A. Faraone, W. A. Kamitakahara, K.-H. Liu, C.-Y. Mou, J. B. Leão, S. Chang, S.-H. Chen, Proc. Natl. Acad. Sci. U.S.A. 108, 12206–12211 (2011)

[31] F. Kremer, A. Schonhals, *Broadband dielectric spectroscopy*, Springer (2003)

[32] G. Hohne, W. Hemminger, H. Flammersheim, *Differential scanning calorimetry*, Springer 2nd edition (2003)

[33] G. L. Squires, *Introduction to the theory of thermal neutron scattering*, Dover Publications, New York (1996)

[34] G. Schirò, C. Caronna, F. Natali, A. Cupane, J. Am. Chem. Soc. 132, 1371 (2010)

[35] F. Gabel, D. Bicout, U. Lehnert, M. Tehei, M. Weik, G. Zaccai, Q. Rev. Biophys. 35, 327 (2002)

[36] M. Tehei, D. Madern, C. Pfister, G. Zaccai, Proc. Natl. Acad. Sci. U.S.A. 98, 14356 (2001)

[37] J. Peters, M. Trapp, D. Hughes et al., High Press. Res. 32, 97 (2012)

[38] V. A. Sidorov, R. A. Sadykov, J. Phys. Condens. Matter 17, S3005 (2005)

[39] F. Natali, J. Peters, D. Russo et al., Neutron News 19, 14 (2008)

[40] P. Kumar, K. T. Wikfeldt, D. Schlesinger, L. G. M. Pettersson, H. E. Stanley, Sci. Rep. 3, 1980 (2013)

[41] Z. Wang, K.-H. Liu, P. Le, M. Li, W.-S. Chiang, J. B. Leão, J. R. D. Copley, M. Tyagi, A. Podlesnyak, A. I. Kolesnikov, C.-Y. Mou, S.-H. Chen, Phys. Rev. Lett. 112, 237802 (2014)

[42] V. K. Malinowsky, V. N. Novikov, A. P. Sokolov, Phys. Lett. A 153, 63 (1991)

[43] J. Wuttke and others, Rev. Sci. Instrum. 83, 075109 (2012)

[44] J. Kendrew, G. Bodo, H. Dintzis, R. Parrish, H. Wyckoff, D. Phillips, Nature 181, 662-666 (1958)

[45] The Nobel Prize in Chemistry 1962 www.nobelprize.org/nobel_prizes/chemistry/laureates/1962/index.html

[46] www.uniprot.org/uniprot/P02144

[47] www.chemwiki.ucdavis.edu/Inorganic_Chemistry/Descriptive_Chemistry/d-Block_Elements/23.6_Transition_Metals_in_Biology

[48] D. L. Nelson, M. M. Cox, *Lehninger Principles of Biochemistry*, 4th edition (2005)

[49] J. Kendrew, Myoglobin and the structure of proteins, Nobel lecture, December 11 (1962)

[50] J. Rupley, E. Gratton, G. Careri, Trends Biochem. Sci. 8, 18 (1983)

[51] J. Rupley, G. Careri, Adv. Protein Chem. 41, 37 (1991)

[52] G. Schirò, A. Cupane, E. Vitrano, F. Bruni, J. Phys. Chem. B 113, 9606-9613 (2009)

[53] G. Schiro, M. Fomina, A. Cupane, J. Chem. Phys. 139, 121102 (2013)

[54] R. Reisfeld, J. Fluoresc. 12, 317−325 (2002)

[55] B. Dunn, J. Zink, I. Acc. Chem. Res. 40, 747−755 (2007)

[56] C. J. Brinker, G. W. Scherer, Academic Press: Waltham, MA (1990)

[57] M. D. Curran, A. J. Stiegman, Non-Cryst. Solids 249, 62−68 (1999)

[58] R. Gupta, N. Chaudhury, Biosens. Bioelectron. 22, 2387−2399 (2007)

[59] A. I. Sulatskaya, A. A. Maskevich, I. M. Kuznetsova, V. N. Uversky, K. K. Turoverov, PLoS One 5, No. e15385 (2010)

[60] J. H. Roh, V. N. Novikov, R. B. Gregory, J. E. Curtis, Z. Chowdhuri, A. P. Sokolov, Phys. Rev. Lett. 95, 038101 (2005)

[61] G. Schiro, C. Caronna, F. Natali, A. Cupane, Phys. Chem. Chem. Phys. 12, 10215 (2010)

[62] K. Wood, D. J. Tobias, B. Kessler, F. Gabel, D. Oesterhelt, F. A. A. Mulder, G. Zaccai, M. Weik, J. Am. Chem. Soc. 132, 4990 (2010)

[63] M. Krishnan, V. Kurkal-Siebert, J. C. Smith, J. Phys. Chem. B 112, 5522 (2008)

[64] G. Schirò, M. Sclafani, F. Natali, A. Cupane, Eur. Biophys. J. 37, 543–549 (2008)

[65] A. Paciaroni, S. Cinelli, E. Cornicchi, A. De Francesco, G. Onori, Chem. Phys. Lett. 410, 400–403 (2005)

[66] A. F. Rasmussen, A. M. Stock, D. Ringe, G. A. Petsko, Nature (London) 357, 423 (1992)

[67] G. Sartor, A. Hallbrucker, E. Mayer, Biophys. J. 69, 2679–2694 (1995)

[68] V. Lounnas, B. M. Pettitt, Proteins 18, 133–147 (1994)

[69] H. Jansson, J. Swenson, Biochim. Biophys. Acta 1804, 20–26 (2010)

[70] S. Khodadadi, J. E. Curtis, A. P. Sokolov, J. Phys. Chem. B 115, 6222–6226 (2011)

[71] F. Bruni, R. Mancinelli, M. A. Ricci, Phys. Chem. Chem. Phys. 13, 19773–19779 (2011)

[72] R. Richert, Eur. Phys. J. B 68, 197–200 (2009)

[73] P. B. Ishai, M. S. Talary, A. Caduff, E. Levy, Y. Feldman, Meas. Sci. Technol. 24, 102001–102021 (2013)

[74] H. Jansson, R. Bergman, J. Swenson, J. Phys. Chem. B 109, 24134–24141 (2005)

[75] J. Swenson, H. Jansson, R. Bergman, Phys. Rev. Lett. 96, 247802–247805 (2006)

[76] J.-M. Zanotti, M.-C. Belissent-Funel, S.-H. Chen, Europhys. Lett. 71, 91 (2005)

[77] P. H. Poole, F. Sciortino, U. Essmann, H. E. Stanley, Nature (London) 360, 324 (1992)

[78] K. Wood, A. Frölich, A. Paciaroni, M. Moulin, M. Härtlein, G. Zaccai, D. J. Tobias, M. Weik, J. Am. Chem. Soc. 130, 4586 (2008)

[79] M. Oguni, Y. Kanke, A. Nagoe, S. Namba, J. Phys. Chem. B 115, 14023 (2011)

[80] Supplemental Material at http://link.aps.org/supplemental/10.1103/PhysRevLett.113.215701

[81] A. Nagoe, Y. Kanke, M. Oguni, S. Namba, J. Phys. Chem. B 114, 13940 (2010)

[82] D. M. Murphy, T. Koop, Q. J. R. Meteorol. Soc. 131, 1539 (2005)

[83] M. R. Arnold, H. D. Lüdemann, Phys. Chem. Chem. Phys. 4, 1581 (2002)

[84] E.W. Lang, H. D. Lüdemann, Ber. Bunsen-Ges. Phys. Chem. 85, 603 (1981)

[85] F. X. Prielmeier, E.W. Lang, R. J. Speedy, H. D. Lüdemann, Phys. Rev. Lett. 59, 1128 (1987)

[86] F. X. Prielmeier, E. W. Lang, R. J. Speedy, H. D. Lüdemann, Ber. Bunsen-Ges. Phys. Chem. 92, 1111 (1988)

[87] F. W. Starr, S. Harrington, F. Sciortino, H. E. Stanley, Phys. Rev. Lett. 82, 3629 (1999)

[88] F. W. Starr, F. Sciortino, and H. E. Stanley, Phys. Rev. E 60, 6757 (1999)

[89] D. Paschek, A. Geiger, J. Phys. Chem. B 103, 4139 (1999)

[90] J. Qvist, H. Schober, B. Halle, J. Chem. Phys. 134, 144508 (2011)

[91] J. Qvist, C. Mattea, E. P. Sunde, B. Halle, J. Chem. Phys. 136, 204505 (2012)

[92] H. D. Lüdemann, E. W. Lang, J. Phys. (Paris), Colloq. 45, C7-41 (1984)

[93] S.-H. Chen, F. Mallamace, L. Liu et al., AIP Conf. Proc. 982, 39 (2008)

[94] S.-H. Chen, Y. Zhang, M. Lagi, S. H. Chong, P. Baglioni, F. Mallamace, J. Phys.: Condens. Matter 21, 504102 (2009)

[95] H. E. Stanley, P. Kumar, S. Han, M. G. Mazza, K. Stokely, S. V. Buldyrev, G. Franzese, F. Mallamace, L. Xu, J. Phys.: Condens. Matter 21, 504105 (2009)

UNIVERSITÀ DEGLI STUDI DI MESSINA

Dipartimento di Fisica e Scienze della Terra.

Prof. Francesco Mallamace, Contr. Papardo salita Sperone n.31, 98166 S. AGATA (Messina, Italy) –
Tel: +39-090-6765016 – Fax: +39-090395004 – e-mail: francesco.mallamace@unime.it

Messina 13-1-2015

Doctoral thesis of Margarita Fomina Dottorato di Ricerca in Fisica Università degli Studi di Palermo.

THE PHYSICAL ORIGIN OF PROTEIN DYNAMICAL TRANSITION: A LIQUID-LIQUID TRANSITION IN HYDRATION WATER?

This thesis deals with a proper experimental study on the protein dynamical transition made by using dielectric spectroscopy, calorimetry and neutron scattering on hydrated proteins. The studies were made at different concentrations and in a large temperature interval including the deep supercooled regime. The main results was also supported by the same studies on water confined in SiO_2 xerogel. The thesis experiments are very interesting with new important results on strongly debated research topics.
The focal point is the confirmation of the existence of a Liquid-Liquid Transition at about 230 K, from a local water structure with an higher density (HDL) characterizing the high temperature regime to a local water structure with a lower density (LDL) characterizing the low temperature regime.

In addition, the obtained results strongly support the idea that the LLT in protein hydration shell is the physical origin of the biologically relevant protein dynamical transition.

The thesis is of high quality, very well written and the reported findings are of deep interest for the people working in different areas of science and technology thus, I am glad to highlight the considerable quality of the work made.

In my opinion the thesis is original and scientifically sound, hence of an overall excellent level.

Francesco Mallamace